Effects of Sn on Microstructure and Dynamic Grain Growth in a Binary Mg-Ca Alloy

by

Monira Binte Mesbah

Student ID: 1017112008

MASTER OF SCIENCE IN MATERIALS AND METALLURGICAL ENGINEERING

Department of Materials and Metallurgical Engineering

BANGLADESH UNIVERSITY OF ENGINEERING AND TECHNOLOGY (BUET)

March, 2020

The thesis titled **"Effects of Sn on Microstructure and Dynamic Grain Growth in a Binary Mg-Ca Alloy"** Submitted by Monira Binte Mesbah, Roll No. 1017112008 and Session: October 2017 has been accepted as satisfactory as a partial fulfilment of the requirement for the degree of M.Sc. Engg. in Materials and Metallurgical Engineering on March 14, 2020.

BOARD OF EXAMINERS

1. HRashed 14.03.2020 — **Chairman** (Supervisor)
   Dr. H. M. Mamun Al Rashed
   Associate Professor
   Department of Materials and Metallurgical Engineering, BUET

2. Fahmida 14.03.2020 — **Member** (Ex-officio)
   Dr. Fahmida Gulshan
   Professor and Head
   Department of Materials and Metallurgical Engineering, BUET

3. 14/03/2020 — **Member**
   Dr. Md. Moniruzzaman
   Professor
   Department of Materials and Metallurgical Engineering, BUET

4. 14/03/2020 — **Member**
   Dr. Kazi Md. Shorowordi
   Professor
   Department of Materials and Metallurgical Engineering, BUET

5. Md. Mohar Ali 14.03.2020 — **Member** (External)
   Dr. Md. Mohar Ali
   Professor (retired)
   Department of Materials and Metallurgical Engineering, BUET

CANDIDATE'S DECLEARATION

It is hereby declared that the experimental studies embodied in thesis are the result of investigation carried out by the author, except where specified by reference to other works. No portion of work referred to in this thesis has been submitted in support of an application for another degree or qualification of this or any other university or other institute of learning.

_____

Monira Binte Mesbah

Student Number: 1017112008

Department of Materials and Metallurgical Engineering, BUET

Dhaka-1000

ACKNOWLEDGEMENT

The author is deeply thankful to her supervisor Dr. Hossain Mohammad Mamun Al Rashed, Associate Professor, Department of Materials and Metallurgical Engineering (MME), Bangladesh University of Engineering and Technology (BUET) for his continuous guidance, suggestions and encouragements throughout the progress of the research work. His assistance and co-cooperativeness has greatly helped towards the completion of this thesis.

The author is greatly thankful to Department of Materials and Metallurgy Engineering, BUET and Department of Glass and Ceramics Engineering, BUET for giving the opportunity and facilities in different labs in due time.

The author is also thankful to all the lab assistants.

Finally, the author is deeply indebted to the authorities of Bangladesh University of Engineering and Technology for providing the facilities and financial support to carry out the research work.

ABSTRACT

The evolution of microstructure and dynamic grain growth of a binary Mg-1Ca alloy with different tin addition (1, 2 and 4 wt.%) was investigated under various conditions of temperatures and strain rates.

Mg-1Ca, Mg-1Ca-1Sn, Mg-1Ca-2Sn and Mg-1Ca-4Sn samples were cast and homogenized. The homogenized samples were rolled at 400^0C. Optical microstructures of both cast and rolled samples were taken for microstructural analysis. Scanning electron microscopy of four rolled samples was carried out for identifying phases present. Tensile test of rolled alloys was carried out at temperatures 300, 350, 400 and 450°C, and at two different strain rates $5x10^{-4}$ s^{-1} and $1x10^{-4}$ s^{-1}. Optical microstructures of tensile tested samples were acquired for observing dynamic grain growth. Samples were taken from six different location of failed (tensile loaded) samples. For understanding deformation mechanisms during grain growth and total deformation, activation energy, strain hardening exponent and strain rate sensitivity index were calculated.

It was found that tin addition increased dendrite formation in as-cast alloys and continuously reduced grain sizes of rolled alloys. Addition of small amount of Sn increased both strength and elongation to failure values. However, higher amount of Sn addition lowered the properties to some extent due to formation of excessive primary intermetallic particles. At lower temperatures, work hardening rate is higher leading to higher strength and lower elongation to failure values. Conversely, at elevated temperatures, strength values were reduced due to inevitable softening and greater grain growth was observed as well. At slower strain rate ($1x10^{-4}$ s^{-1}), higher dynamic grain growth was observed than higher strain rate ($5x10^{-4}$ s^{-1}). At slower strain rate, value of strain rate sensitivities became higher ($m>0.33$), which indicated superplastic behavior, in addition, deformation mechanisms of grain boundary sliding and diffusional creep.

TABLE OF CONTENTS

LIST OF FIGURES

LIST OF TABLES

LIST OF ABBREVIATIONS

CRSS	Critical Resolved Shear Stress
DGG	Dynamic Grain Growth
DRX	Dynamic Recrystallization
DRV	Dynamic Recovery
EDS	Energy Dispersive Spectroscopy
SGG	Static Grain Growth
SRX	Static Recrystallization
SRV	Static Recovery
SEM	Scanning Electron Microscopy
UTS	Ultimate Tensile Stress
XRF	X-Ray Fluorescence

Chapter 1
Introduction

In recent years, there has been an increasing demand for energy conservation and environmental protection [1]. Rising concern has been given to wrought magnesium (Mg) alloys for its high specific strength, desirable recyclability and great potential for enhancing fuel efficient vehicles and green environment [2]. Alongside the many benefits, there are difficulties with using magnesium as an industrial material due to its low formability at room temperature. This arises from the limited number of slip systems available in HCP magnesium alloys at room temperature. The limitation of having few slip systems is further complicated by magnesium's tendency to develop and retain a strong texture during deformation. Due to its low formability, alloying elements are added to increase its strength, formability and weld-ability. These alloying elements in proper portion also results in corrosion and wear resistance that leads it to a good candidate for automotive industry.

In general, grain refining and precipitation strengthening are considered as two effective strategies to improve strength of Mg alloys [3].However, in the case of rare earth (RE)-free Mg alloys (such as Mg-Al-, Mg-Sn- and Mg-Ca-based), their age-hardening responses are usually not yet significant due to difficulty in achieving nano-dispersions, such as, nano precipitates and grains. Fortunately, it is known that the grain refinement in Mg alloys contributes to the strengthening more significantly than the other alloy systems (such as Al alloys), attributed to their higher k values in Hall-Petch relationship [4]. Calcium (Ca) was found to distinctly refine grains and enhance mechanical properties profoundly in Mg alloys [5, 6]. In addition to grain refining, precipitation strengthening by RE elements has gained attraction over the last two decades due to their wide-ranging capabilities of precipitate-forming. Nevertheless, due to scarcity of RE elements and their price, very recently tin (Sn) has become a promising alternative [7, 8]. Therefore, grain refining by addition of Ca and promoting precipitation hardening by Sn addition are expected to very effective strengthening of Mg alloys.

In this work, the microstructure and dynamic grain growth (DGG) of Mg-1Ca-xSn alloy

have been investigated with variation of Sn content. From this work, effects of Sn on microstructure of cast, rolled and tensile tested alloys can be evaluated. In addition, effects of Sn on tensile property and dynamic grain growth can be understood. Moreover, effects of temperature and strain rate on Mg-1Ca alloy with and without Sn, can be observed.

Microstructural study of Mg-Ca alloy system [9] with addition of Sn [10, 11] is a new opportunity for hardening in Mg alloys. During thermo-mechanical treatment of this alloy system, the mechanism for deformation is yet to establish. One window for such observation would be study of dynamic grain growth [12]. Such understanding will establish thermo-mechanical treatment schedules for promising Sn containing Mg alloys.

This thesis contains several chapters. In chapter two, the review of previous works related to this thesis work is discussed. It contains about magnesium, effects of alloying elements, classifications and applications of Mg alloys, deformation of Mg single crystal and polycrystal, high temperature behavior of different Mg alloys and effects of Sn on deformation and microstructure. In chapter three, experimental procedure of this thesis work is discussed. This chapter contains details of raw materials, casting method, different experiments, such as, XRF, homogenization, hot rolling, microscopic observations, SEM analysis, tensile test and dynamic grain growth analysis. In chapter four, results of these experiments are discussed, and from these results, deformation mechanisms during grain growth are identified. Finally, in Chapter five, results of present thesis work are summarized.

Chapter 2
Literature Review

2.1 Magnesium

Magnesium belongs to alkaline earth metals, which occupy the second main group of the periodic table of elements. It was discovered in the eighteenth century and named after the ancient Greek district of Magnesia in Eastern Thessaly. This silvery-white metal is the eighth most abundant element, comprising 2.7% of earth's crust. Due to its high reactivity, magnesium is not found in elemental form in nature, but only in chemical complexes. It is widely distributed in rock structures, seawater and lake brines [13]. The most common compounds are magnesite ($MgCO_3$), dolomite ($MgCO_3 . CaCO_3$), carnallite ($KCl . MgCl_2 . 6H_2O$) [14]. Magnesium is the lightest of all structural metals. It has a density of 1.74 g/cm^3, which is approximately one-fourth the density of steel and two-thirds that of aluminum. Due to its light weight, strength and resistance to corrosion, it is primarily used as structural alloy [15].

2.1.1 Mechanical Properties

Tensile strength of pure magnesium rolled sheet is in the range of 149 MPa to 153 MPa. Elongation to failure is in the range of 2.9 % to 3.1%. 2% proof strength is in the range of 83 MPa to 86 MPa, and 2% compressive strength is in the range of 69 MPa to 83 MPa. Young's modulus, shear modulus and bulk modulus of this sheet are 44.7 GPa, 17.3 GPa and 44.7 GPa, respectively. Moreover, at 400°C, vapour pressure is 6.53 x 10^{-9} Pa [17].

2.2 Effects of Alloying Elements in Magnesium

The addition of alloying elements in pure magnesium helps to alter its properties. Magnesium is chemically active and can react with other metallic alloying elements to form intermetallic compounds. In most magnesium alloys, the presence of intermetallic phases can be observed. These phases aid to influence the microstructure, and hence, affect the mechanical properties

of the magnesium alloys. Solid solution hardening and/or precipitation hardening are the key mechanisms to enhance the mechanical performance the magnesium-based materials.

The effects of addition of major metallic elements on magnesium are discussed below.

Aluminum. Aluminum rapidly diffuses through magnesium matrix and acts as a passivating element. It improves corrosion resistance and die casting ability. Moreover, it increases hardness and strength [18, 38].

Calcium. The addition of calcium improves thermal and mechanical properties as well as assists in grain refinement and creep resistance. Further, it reduces surface tension [18].

Zinc. Magnesium alloys containing zinc have an elastic modulus similar to bone. The presence of Zn can reduce hydrogen gas evaluation during bio-corrosion. Also, it increases alloy fluidity in casting [18, 40-42].

Tin. The addition of tin improves ductility. In addition it reduces the tendency to cracking during processing [18].

Copper. Copper increases both room and high temperature strengths of magnesium alloy. However, it also accelerates corrosion rates when exposed to NaCl medium [18].

Manganese. The addition of manganese reduces harmful effects of impurities and improves corrosion resistance [18].

Lithium. The addition of lithium improves corrosion resistance [18].

Nickel. Nickel increases both yield strength and ultimate tensile strength at room temperature. It negatively impacts on ductility and corrosion resistance [18].

Strontium. Strontium is used in conjunction with other elements to enhance creep performances [18].

Yttrium. The addition of yttrium improves high temperature properties and corrosion resistance [18].

Rare earth elements. The addition of rare earth element improves corrosion resistance and mechanical properties [18].

2.3 Classification of Magnesium Alloys

The American Society for Testing and Materials (ASTM) has developed a coding system that is widely used for classification of magnesium alloy. The system is a 'letter-letter-number-number' code. The letters indicate the two principal alloy elements listed in order of decreasing content. When the two alloying elements are present in an equal amount, then they are listed alphabetically. The code letters used to identify the alloying elements are given in Table 2.1. The two numbers specify the weight percent of the two principal alloying elements, rounded off to the nearest whole number and listed in the order of the two elements [19]. For example, the alloy AZ91 signifies that aluminum (A) and zinc (Z) are the two main alloy elements, and their weight percentages are about 9 and 1 wt%, respectively.
The major groups of magnesium alloys are based on the following compositions:

- magnesium–aluminum–manganese (Mg–Al–Mn)
- magnesium–aluminum–zinc (Mg–Al–Zn)
- magnesium–zinc–zirconium (Mg–Zn–Zr)
- magnesium–rare earth metal–zirconium (Mg–RE–Zr)
- magnesium–rare earth metal–silver–zinc (with or without thorium) (Mg–RE–Ag–Zn)
- magnesium–thorium–zirconium (with or without zinc) (Mg–Th–Zr)

Table 2. 1: ASTM lettering system for magnesium alloys

A: Aluminum	H: Thorium	N: Nickel
B: Bismuth	K: Zirconium	P: Lead
C: Copper	L: Lithium	Q: Silver
D: Cadmium	M: Manganese	T: Tin
E: Rare earths	R: Chromium	W: Yttrium
F: Iron	S: Silicon	Z: Zinc

2.4 Applications of Mg Alloy

Mg alloy is used in a wide range of applications. Some applications of magnesium alloy are shown in Figure 2.1.

Automotive Applications

In the 1920s, magnesium parts made their way into racing cars. However, it was not until the 1930s that magnesium was used in commercial vehicles such as the Volkswagen (VW) Beetle. The VW Beetle, back then, contained more than 20 kg of magnesium alloy in the transmission housing and the crankcase.

Over the past decade, the increasing environmental and legislative pressures on the automotive industry to produce lighter, higher fuel efficiency, and higher performance vehicles have resulted in the surge in the use of magnesium. Widely used conventional steel parts are being replaced by new advanced materials such as magnesium, aluminum, and metal matrix composites. Leading automobile makers such as Audi, Volkswagen, Daimler Chrysler (Mercedes-Benz), Toyota, Ford, BMW, Jaguar, Fiat, Hyundai, and KIA Motors Corporation have used magnesium-based materials in their automotive parts [19].

Aerospace Applications

In the aerospace industry, weight reduction is the major objectives. The reduction in overall weight of the aircraft will result in fuel savings, which saves cost. Several weight reduction alternatives such as low-density structural plastics, aluminum and fiber metal laminates have been founded over the years. Nevertheless, low-density structural plastics have low impact and damage tolerance properties. In addition, the limited progress in the development of aluminum alloys has made weight reduction a challenge. Moreover, fiber metal laminates are also high-cost materials. They also reveal inferior properties when subjected to temperature. All these limitations have made magnesium an attractive alternative. There is widespread use of magnesium in spacecraft and missiles due to the requirement for lightweight materials to reduce the lift-off weight. This is coupled with its high specific mechanical properties, ease of fabrication and its capability to withstand elevated temperatures, exposure to ozone and bombardment of high-energy particles and small meteorites. A large amount of magnesium sheets was used in the Titan and Atlas intercontinental ballistic missiles [19].

Figure 2.1: Some applications of Magnesium alloy [19-23]

Medical Applications

Magnesium alloys were first introduced as orthopedic biomaterials in the first half of the last century [20]. However, because of its low corrosion resistance, a large amount of hydrogen accumulates around the implant during the *in vivo* corrosion process, confining the widespread use of magnesium-based materials as biomaterials. Despite this, magnesium still possesses many attractive characteristics that make magnesium- based materials potential candidates to serve as implants for load-bearing applications in the medical industry.

Magnesium is also present as a natural ion in the human body, whereby approximately 1 mole of magnesium is stored in a 70 kg adult human body and an estimated amount of half of the total physical magnesium is present in the bone tissue [21]. It also assists in many human metabolic reactions and is nontoxic to the human body. Magnesium has good biocompatibility and it is biodegradable in human body fluid by corrosion, thus eliminating the need for another operation to remove the implant. All these desirable features make magnesium-based material a promising implant material [20–22].

In order to overcome the corrosion issues that limit the use of magnesium-based materials in orthopedics application, much research efforts in recent years are focused to explore the use

of different alloying elements in magnesium and surface treatments such as protective coatings on magnesium-based materials [20].

Sports Applications

Magnesium is used in sports equipment due to its light weight and impact resistance. In addition, magnesium has the ability to be formed into intricate shapes which is ideal for use in golf clubs, tennis rackets and the handles of archery bows. Moreover, the damping effects of the alloys make it a good candidate for bicycle frames and the chassis of in-line skates since the magnesium can absorb shock and vibration. This absorption allows cyclist to exert less energy and enjoy a smoother, more comfortable ride. Magnesium vaulting poles have also come into production as they have minimal twisting due to their high torsional strain resistance [19].

Electronic Applications

The trend in the electronic equipment industry is to make products more personal and portable. Hence, it is important that the components that make up the equipment are lightweight and also durable. Magnesium-based materials meet the necessary requirements as they are as light as plastic, but exhibit great improvement in strength, heat transfer, and the ability to shield electromagnetic interference and radio frequency interference, as compared with their plastic counterparts [23].

The ability to form magnesium alloys into complex shapes and the good heat dissipation and heat transfer characteristics of magnesium alloys also result in the use of magnesium alloys in heat sinks and the arms of the hard-drive reader [23].

2.5 Deformation of Mg Single Crystal

The crystal structure of Mg is hexagonal close-packed (HCP). The primitive hexagonal unit cell has three axes (a_1=a_2≠c) with corresponding angles (α=β=90°, γ=120°). In one primitive hexagonal unit cell, two atoms are placed forming a double lattice structure. Thus, the stacking sequence of HCP structure along c direction is ABABAB in the ideal case (atom layers of cyan and black in Figure 2.2) [24].

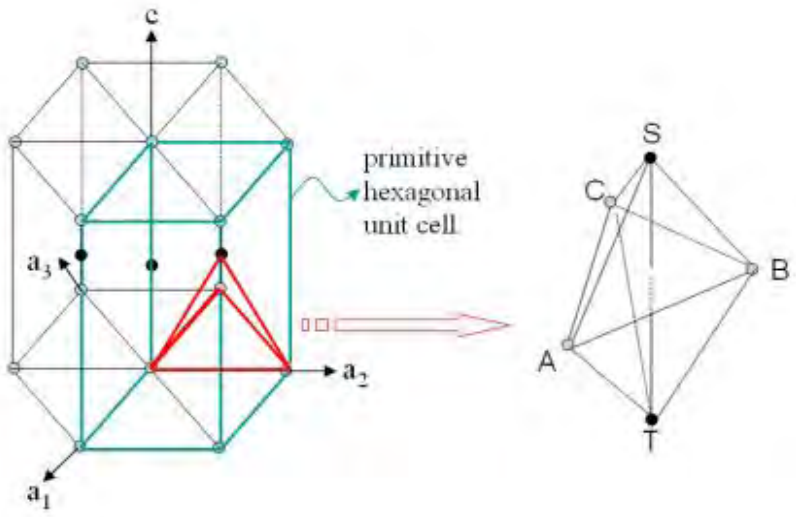

Figure 2.2: Hexagonal close-packed structure. The hexagonal primitive unit cell contains 2 atoms and Thomson-tetrahedron which is used in FCC can be applied to explain the slip system [24]

In terms of crystallography, the basic difference between HCP and face center cubic (FCC) is the asymmetry of the array of atom. The unit cell is defined by cubic in case of FCC whereas cubic system is not proper to apply to HCP. In order to define the indices of directions and planes in HCP structure, usually Millier-Bravais notation with four axes has been used. The 4- axis system is based on the vectors a_1, a_2, a_3 and c as shown in Figure 2.2, where a_3 is redundant since $a_3 = -(a_1+a_2)$.

Two important material parameters determine the deformation behavior [24]. One of the parameters is c/a ratio. The shortest distance from the atom center to a and c axis is usually presented as a and c, respectively. The ideal axial ratio c/a equals $\sqrt{8/3}=1.633$. However, no pure metal has this ideal c/a ratio. Depending on the c/a ratio, some metals such as Zr, Cd show the twinning dominant deformation when compressive load is applied along c axis, while tensile load is needed for twinning in Mg and Be. Another parameter is the elastic modulus [24].

2.5.1 Slip

The plastic deformation of metals usually occurs by slip, which essentially involves the sliding of blocks of the crystal along definite crystallographic planes (slip planes) via the motion of dislocations through the crystal lattice [24]. It commonly operates along close

packed planes and in close packed directions, and only occurs once the applied shear stress has exceeded a critical value (critical resolved shear stress, or CRSS). Although HCP metals can have many slip systems and twinning systems, Mg is known to be deformed mainly by four slip systems and one twinning system [24]. Figure 2.3 shows the five deformation modes in Mg. Figure 2.3 (a), (b), (c) and (d) are basal, prismatic, pyramidal ‹a› and pyramidal ‹c+a› slip systems, whereas (e) is tensile twin system.

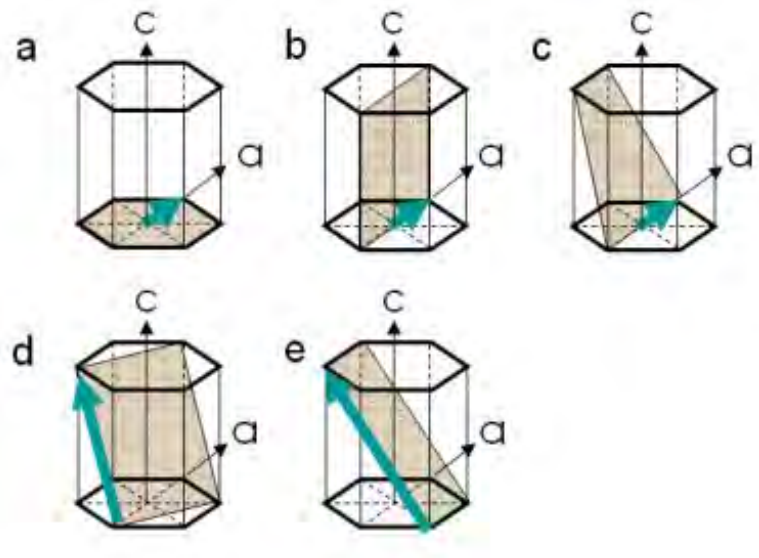

Figure 2.3: Deformation system of magnesium. (a), (b), (c) and (d) are basal, prismatic, pyramidal ‹a› and pyramidal ‹c+a› slip systems, respectively, whereas (e) is tensile twin system [24]

Table 2.2: Some important information of four slip systems and twinning system [24]

Type	Slip/Twin plane	Slip/Twin direction
Basal slip	(0001)	$[11\bar{2}0]$
Prismatic slip	$(10\bar{1}0)$	$[11\bar{2}0]$
Pyramidal slip ‹a›	$(10\bar{1}1)$	$[11\bar{2}0]$
Pyramidal slip ‹c+a›	$(11\bar{2}2)$	$[\bar{1}\bar{1}23]$
Twinning	$(10\bar{1}2)$	$[10\bar{1}1]$

Burger vectors for the structure may also be explained in a similar manner of the Thompson tetrahedron for face-centered-cubic metals as shown in Figure 2.2. Some important information of four slip systems is listed in Table 2.2. The basal, prismatic, pyramidal ‹a› slip systems have ‹a› Burger vector, whereas the pyramidal ‹c+a› slip system has ‹c+a› Burger vector, therefore, the energy of the Burger vector of pyramidal ‹c+a› slip system is greater than that of other slip systems, therefore energetically less stable. At least five independent slip systems are required to achieve homogeneous, generalized ductility. Basal slip system and prismatic slip system has two independent slip modes, respectively. The strain accommodation due to the twin might give another deformation mode [24].

At ambient temperatures, crystallographic slip in magnesium alloys occurs most readily on the (000l) basal plane (the close packed plane) in the $[11\bar{2}0]$ direction. At elevated temperatures, prismatic and pyramidal slip systems are enabled, as there is a reduction in their critical resolved shear stresses [Figure 2.4].

Prismatic slip occurs on the $(10\bar{1}0)$ vertical face planes in the $[11\bar{2}0]$ direction, and pyramidal slip ‹a› occurs on the $(10\bar{1}1)$ planes in the $[11\bar{2}0]$ direction. Pyramidal slip ‹c+a› occurs on the $(11\bar{2}2)$ planes in the $[\bar{1}\bar{1}23]$ direction. These extra slip systems enhance the ductility of magnesium. Consequently, primary fabrication methods are generally carried out at elevated temperatures.

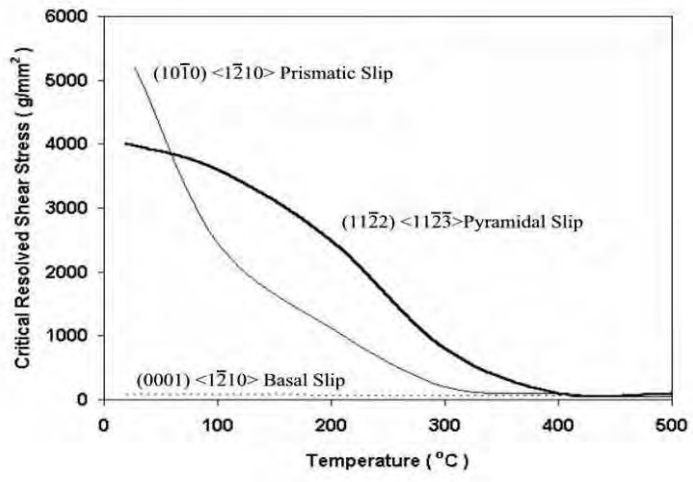

Figure 2.4: The critical resolved shear stress (CRSS) for basal slip [25], prismatic slip [26] and pyramidal slip [27] in pure magnesium.

$(11\bar{2}2)$ $[\bar{1}\bar{1}23]$ pyramidal slip, which operates out of the basal plane, has been observed in magnesium [25]. Although the system was found to be operative from room temperature

to 500°C, the CRSS for this system was found to be higher than the other slip systems operative above room temperature and so it is only observable in single crystals deformed under the constrained orientation of c-axis compression. It should be noted, however, that recent studies that modeled the deformation of AZ3l at room temperature [26] and elevated temperatures have indicated that $(11\bar{2}2)$ $[\bar{1}\bar{1}23]$ pyramidal slip is likely to contribute to the deformation of magnesium poly crystals when compressed along the c-axis.

Of the above slip systems, $(11\bar{2}2)$ $[\bar{1}\bar{1}23]$ pyramidal slip is the only one that can accommodate deformation along the c-axis. However, as evident in Figure 2.3, it has a high CRSS, particularly at low temperatures. In cases where tension is applied along the c-axis, $(10\bar{1}2)$ $[10\bar{1}1]$ twinning is often activated. The CRSS for this system is around 2-4 times that for basal slip. However, other twin systems have been observed [26, 27].

2.2.2 Twinning

Twinning proceeds by the atoms translation for the accommodation of deformation, thus, it is a polar mechanism which cannot be reversible, while slip is reversible process. Nevertheless, the understanding of twin is of importance because twinning is a major deformation mode with basal slip at room temperature. The twin nucleation stress is much higher than the twin propagation stress. Therefore, twin can easily occurs at the stress concentrated zone such as grain boundary. Twin leads to the reorientation of the crystal. In case of tensile twin of Mg, the misorientation is about 87.3 degrees. However, that does not mean that there was huge translation in atom array. Only a small atomic translation can change the crystallographic orientation. Actually, although the contribution of twin itself to plastic strain is not so tremendous in case of polycrystalline, twin can play an important role because the twin modifies the crystallographic orientation of the crystal to the dislocation-slip-favored-orientation. In case of mono-crystalline magnesium, due to the absence of grain boundary, almost all volume is twinned, once twin occurred. Therefore, the influence of twin is much larger in single crystal. The incidence of twinning is affected by the purity of the metal. The twinning behavior can be changed depending on the sample size. At the bulk scale, twins can occur at several points and they meet each other after their propagation. This lead to the heterogeneous stress field in the sample and as a result, secondary twin can be generated. In contrast, at the small scale, once the twinning happens, twin propagates and almost all region of the sample is twinned [33]. Therefore, there is no chance for twins to interact each other.

Several twin modes have been studied in HCP metals. Although $(10\bar{1}1)$ $[10\bar{1}2]$ twin, so-called compression twin, can be occurred at high strain rate, $(10\bar{1}2)$ $[10\bar{1}1]$ twin, so-called tensile twin, is observed widely. Tensile twin is named because $(10\bar{1}2)$ $[10\bar{1}1]$ twin occurs when tensile stress is applied along c-axis. The deformation mechanism due to twinning can be explained employing Figure 2.5. As shown in Figure 2.5, once twin occurs on twin habit plane K_1, atoms translate along η_1 direction with the rotation axis of R [24].

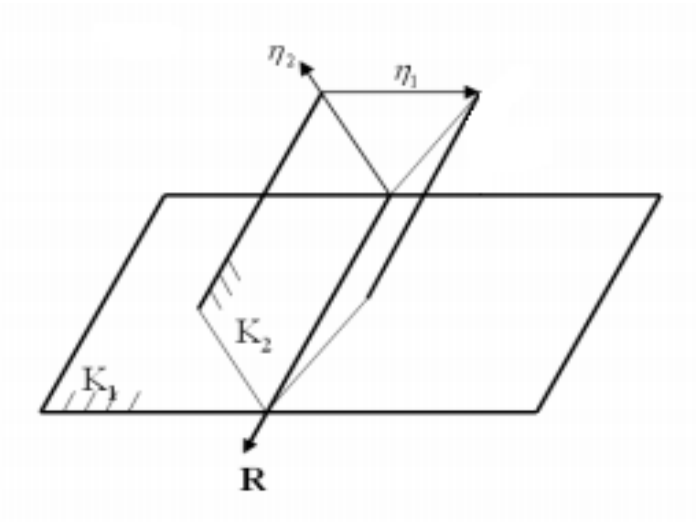

Figure 2.5: Schematic image of twin mechanism [24]

In case of Mg, lattice system of HCP structure is double. Thus, the translation of four atomic layers is needed to complete the tensile twinning process. The atoms in second or third layers can only have the small amount of translation, so-called shuffling [24].

Activation of a twin depends on the direction of the applied stress and also depends on the extension or contraction of c-axis of a crystal. Twinning provides an extra independent mode of deformation in magnesium, but provides only limited strain.

2.6 Deformation of Mg Polycrystal

Cold rolling is a common metal forming process that results in pronounced texture evolution. Plastic deformation during cold rolling primarily leads to the alignment of basal planes with the rolling direction (RD) with increasing deformation [29, 33]. This deformation during the rolling process is characterized by superimposed shear and compressive strains [30, 33]. The complexity of the lattice structure of Mg is oftentimes described by only a reduced set of slip

and twin systems, whose choice may lead to different material behavior. Here, three cases are considered for demonstrating texture evolution in polycrystalline Mg.

Case i. Basal, prismatic, and pyramidal ‹a› slip systems and (10$\bar{1}$2) [10$\bar{1}$1] tensile twin systems.

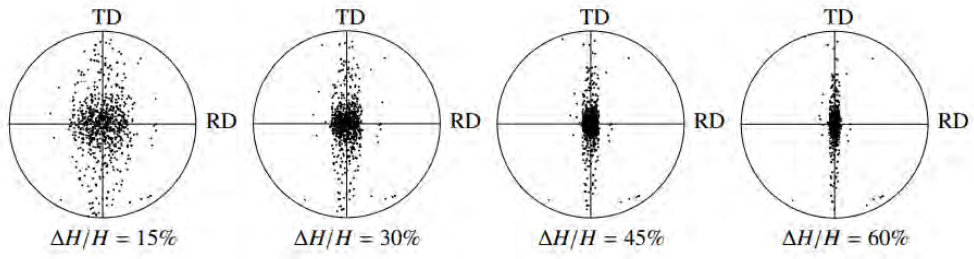

Figure 2.6: Texture evolution during the cold rolling process, showing (0001)-poles moving towards the normal direction (ND) [33]

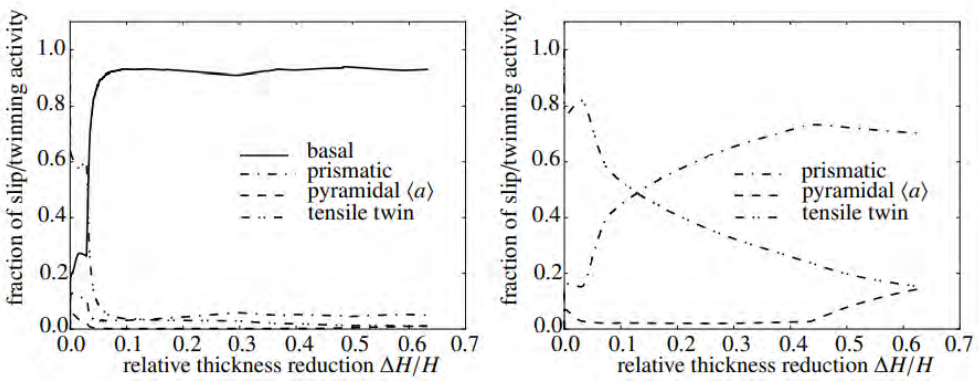

Figure 2.7: Relative contributions of slip and twin systems. The left figure shows all slip/twin system contributions; the right figure shows the contributions without the dominant basal slip [33]

In case i, pyramidal ‹a› slip systems are included while pyramidal ‹c+a› slip systems are not included. Pyramidal ‹c+a› slip has been rarely observed during cold rolling, which is why pyramidal ‹a› slip systems are considered rather than pyramidal ‹c+a› slip systems. Figure 2.6 illustrates the resulting grain distributions with increasing levels of thickness reduction. Figure 2.7 shows the relative activities of each slip/twin system. Obviously, the (0001)-poles gradually move towards the rolling normal direction (ND). This is mainly due to activity of the basal slip systems (more than 90% of the total slip is basal). The alignment of the grain

orientations in the rolling direction is considerably faster than in the transverse direction. This can be explained by the direction of the applied simple shear. In technological applications, typical cold rolling procedures often involve several passes of a single workpiece through the rolling device, and each pass can be performed with a different rolling direction, which ultimately leads to a faster directional alignment. Although, the overall plastic deformation of the polycrystal is mainly the result of basal slip activity, a significant number of grains undergoing tensile twinning at low deformation levels can be observed. At small thickness reductions of ΔH/H <7%, more than 60% of the total plastic deformation comes from twinning (Figure 2.7). However, as those grains approach the twinned states, basal slip activity in the twinned grains catches up and dominates the ensuing deformation [33].

Case ii. Basal, prismatic, and pyramidal ‹c+a› slip systems and (10$\bar{1}$2) [10$\bar{1}$1] tensile twin systems.

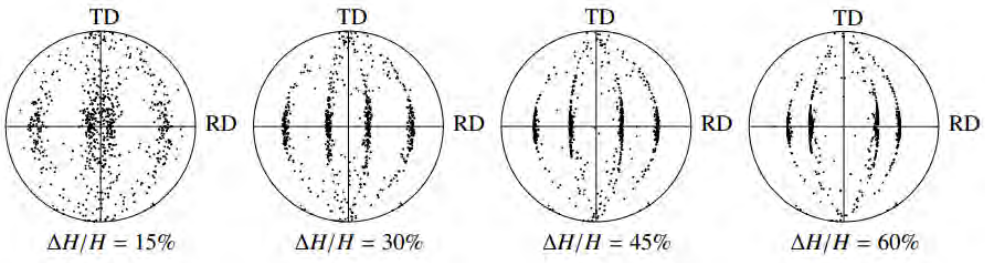

Figure 2.8: Texture evolution during the cold rolling process shown by (0001)-pole figures [33]

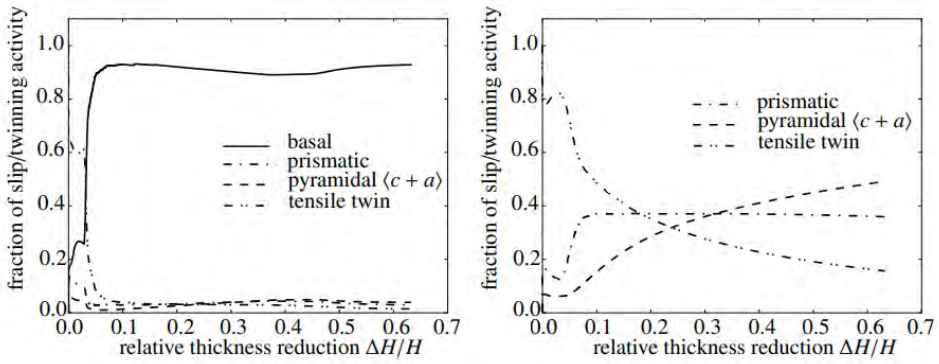

Figure 2.9: Relative contributions of slip and twin systems. The left figure shows all slip/twin system contributions; the right figure shows the contributions without the dominant basal slip [33]

Most models in the literature have included pyramidal ‹c+a› systems to accommodate non-basal slip. For this case, the grain distribution and the relative activity of each slip/twin system for the same cold rolling scenario are summarized in Figures 2.8 and 2.9, respectively. Here, a quite different texture evolution compared to the previous case can be observed. Indeed, the final grain distribution resembles that of plane-strain compression of FCC metals. The activation of the pyramidal ‹c+a› systems tends to reorient the basal slip systems. Although the overall deformation is dominated by basal activity, the contributions of the pyramidal slip systems (the dashed line in Figure 2.9) are significantly higher than in the previous case [46].

Case iii. Basal, prismatic, and pyramidal ‹a› slip systems and $(10\bar{1}1)$ $[10\bar{1}2]$ compression twin systems.

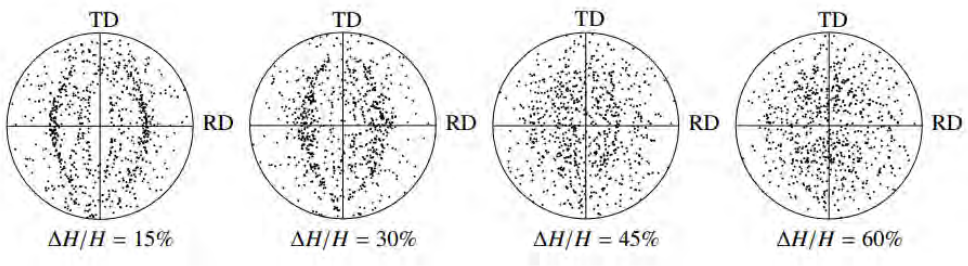

Figure 2.10: Texture evolution during the cold rolling process shown by (0001)-pole figures [33]

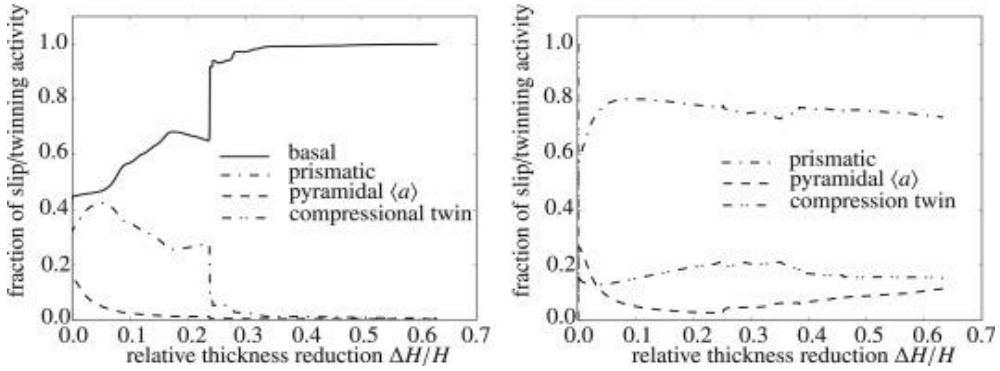

Figure 2.11: Relative contributions of slip and twin systems. The left figure shows all slip/twin system contributions; the right figure shows the contributions without the dominant basal slip [33]

Because of the high critical resolved shear stress and large critical shear strain, compression twins are rarely observed and often omitted in simulated texture predictions [31-33]. For

illustrative purposes, only compression twinning is included (tensile twinning is suppressed) to demonstrate its effect on the texture evolution. Grain distribution and relative slip/twin activities for this case are shown in Figures 2.10 and 2.11, respectively. The polycrystal does not develop any preferably-oriented texture in this case because of the high barrier to activate compression twins [33].

2.7 High Temperature Behavior of Mg Alloys

2.7.1 The Basics of Hot Working Stresses and Microstructures

The flow stress (σ_f) during deformation is of great significance for hot working as it gives an indication of the load required for the process. During hot deformation there are several, often competing, deformation mechanisms which affect the flow stress. A generalized stress-strain curve during hot deformation is represented in Figure 2.12.

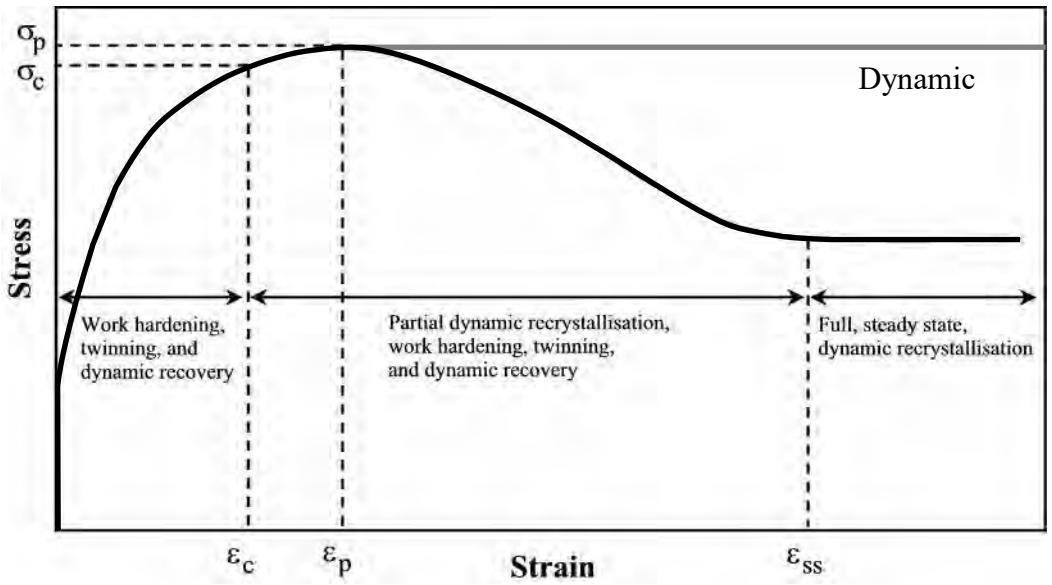

Figure 2.12: A schematic representation of the stress-strain behaviour during hot deformation [36]

During the initial stages of deformation, work hardening, dynamic recovery and possibly twinning are operative but when the critical strain, or stress, is reached (ε_c or σ_c), dynamic recrystallisation initiates. This softening mechanism also aids in reducing the rate of work hardening but with further straining, the degree of flow softening outweighs that of work hardening and the flow stress begins to drop. The operation of dynamic recrystallization

creates a peak in the stress-strain behavior (σ_p and ε_p). Upon further straining, a flattening of the stress-strain curve is generally observed which signifies full steady-state dynamic recrystallization [36].

The flow stress during hot deformation is sensitive to temperature and strain rate. An increase in temperature yields a greater contribution to flow softening from mechanisms such as dynamic recovery and dynamic recrystallization, and the peak flow stress is shifted to lower stresses and lower strains. This is due to the fact that softening mechanisms are thermally activated. A similar trend is observed with a reduction in strain rate. A reduction in strain-rate allows more time for the operative mechanism to counteract the increase in flow stress from work hardening [36].

The basic operation of work hardening, dynamic recovery, dynamic recrystallization, dynamic grain growth, static recovery, static recrystallization and static grain growth are examined below. Twinning has been considered when the crystallographic deformation of magnesium is discussed.

Work Hardening

The mechanism by which a material gets harder as it is plastically deformed is known as work hardening. Since plastic flow occurs by a dislocation mechanism the fact that work hardening occurs means that it becomes difficult for dislocations to move as the strain increases [34]. During the initial stages of deformation, dislocation sources are activated and mobile dislocations move along slip planes within the crystal lattice. As strain is increased, dislocations multiply and interact, resulting in an increase in the stress required to move the dislocations through the crystal lattice. Obstacles such as grain boundaries and particles also impede dislocation motion.

Dynamic Recovery

Dynamic recovery (DRV) involves the thermally activated annihilation and rearrangement of dislocations during deformation. DRV is an important mechanism in metals of high stacking-fault energy such as aluminum, most bcc metals, and magnesium. During DRV, dislocations arrange themselves into cell walls, forming small angle or subgrain boundaries, in order to reduce the lattice strain energy [35].

Dynamic Recrystallization

When recovery processes are slow, or recrystallization processes are fast, dynamic recrystallization (DRX) may occur. DRX is more pronounced in metals with a low to medium stacking-fault energy, such as copper and nickel. DRX processes are dependent on temperature, strain, strain rate, composition, texture and initial grain size. DRX is an important mechanism during deformation as it not only reduces the flow stress but also controls the final microstructure, and hence the final properties of the material.

Conventional, or discontinuous, DRX involves the replacement of the deformed lattice by a new unstrained lattice through a process of nucleation and growth of new grains. Once nucleated, the strain free grains grow, driven by the density and distribution of dislocations. The dislocation density of the new DRX grains increases as deformation continues. This reduces the driving force for further growth and results in a constant average grain size for a given strain rate and temperature [36].

Dynamic Grain Growth

After recrystallization is complete, the strain free grains will continue to grow at elevated temperature. This phenomenon is called grain growth. It depends on temperature, solutes and particles, specimen size, texture and time. Grain growth occurs by the migration of grain boundaries. As grains increase in size, the total boundary area decreases, yielding an attendant reduction in the total energy; this is the driving force for grain growth [39]. In all polycrystalline materials, grain growth can take place. Grain growth that occurs during superplastic deformation is called dynamic grain growth (DGG) [59].

Static Recovery

Static recovery (SRV) is a similar process to that of dynamic recovery in that it involves dislocation annihilation, dislocation rearrangement and sub-grain growth. It is driven by the lattice strain energy and so depends on the number of dislocations and other defects remaining in the material after deformation. In hot working, the microstructural changes due to static recovery are generally very small because dynamic recovery has already preceded it. After the deformation of austenite, however, approximately 25% of the softening is generally attributed to SRV, with the rest attributed to SRX [37].

Static Recrystallization

Static recrystallization (SRX) can occur after deformation so long as there is sufficient stored energy and thermal activation. Stored energy is affected by the amount of deformation, the temperature, the strain rate and the amount of recovery. The growth rate depends on factors such as temperature, composition, stored energy and texture. SRX occurs very rapidly at high temperatures but as the temperature is reduced, the recrystallization time increases exponentially. Rapid cooling immediately after deformation can suppress SRX and in these cases the deformed structure will be retained [37].

Static Grain Growth

Grain growth that occurs during annealing is called static grain growth (SGG) [59]. Stress or load is not applied during static grain growth, only temperature is the main factor while during dynamic grain growth both temperature and stress/load are applied. For this reason, amount of dynamic grain growth is always higher than static grain growth.

2.7.1.1 Deformation Mechanisms of Grain Growth

Deformation mechanism can be obtained by two methods. First is accomplished by activation energy calculation. Second method involves calculation of strain hardening exponent or strain rate sensitivity index.

Activation Energy

Minimum energy required for grain boundary movement is called activation energy. It is a parameter to understand the deformation mechanism during grain growth. Value of activation energy can vary with temperature and strain rate. Activation energy for grain boundary diffusion is 92 kJ mol^{-1} and activation energy for lattice self-diffusion is 135 kJ mol^{-1} in pure Mg [48]. Therefore, a relatively high activation energy is associated with lattice self-diffusion. However, from practical point of view, to assess precise superplastic deformation mechanisms by measuring activation energy is not a very promising approach [55].

Strain Hardening Exponent

Strain hardening exponent (n) is the ability of a material to harden. It measures how the metal behaves when it is being formed. It can be obtained from the slope of the log based true

stress-strain curve. Deformation mechanisms varies with the values of n. Deformation follows diffusional creep mechanism for n=1, grain boundary sliding for n=2, glide-controlled creep for n=3, climb-controlled creep for n=4-5, and dispersion-strengthened alloy for n>8 [55].

Strain Rate Sensitivity Index

Strain rate sensitivity index (m) is the indication of how much sensitive a material is to strain rate. It is inversely proportional to strain hardening exponent (n). The value of m is directly related to the tensile ductility of metallic alloys. When m is low, the increase in stress at the neck will lead to a large increase in strain rate in that region. Thus, the neck will grow sharply, leading to sudden failure and a low elongation to failure. Conversely, when m is large, the strain rate increases slowly due to the increased stress in the neck region. As a result, the neck forms gradually, a delay of onset of tensile failure, which leads to high tensile elongations [55]. A high m value is found to be a necessary and usually sufficient requirement to achieve superplastic behavior in metallic alloys. Different deformation mechanisms are found for different values of m, as, diffusional creep mechanism for m=1, grain boundary sliding for m=0.5, glide-controlled creep for m=0.33, climb-controlled creep for m=0.14-0.25, and dispersion-strengthened alloy for m< 0.125 [55].

2.7.2 The Hot Working of Magnesium

Deforming magnesium and its alloys at elevated temperatures is of great metallurgical importance as not only is the workability improved but the final grain size, and to a great extent the final properties of the material, are altered. The operation of dynamic recrystallization during the hot deformation of magnesium is of particular importance as it reduces the flow stress during deformation and controls the final grain size. Therefore, to be able to successfully control the microstructural evolution during bulk working operations, an understanding of hot deformation behavior of magnesium, particularly the operation of DRX, is essential.

Alloying elements affect the deformation behavior of magnesium. The following binary systems are discussed to understand the hot deformation of magnesium in the presence of other elements.

2.7.2.1 Mg-Ca System

Figure 2.13 shows the calcium and magnesium binary phase diagram. Calcium behaves like as a grain refiner and creates the stable intermetallic Mg_2Ca, which has a higher melting point (715°C) than magnesium, which if precipitated, may increase high temperature strength. Two eutectic reactions and a congruently melting compound characterize the system. The Mg-rich eutectic point is at 10.5 at.% Ca and at 516.5°C, and the Ca-rich eutectic point is at 73 at.% Ca and at 445°C [58]. The low melting temperature eutectics allow liquid formation during sintering, which may help quickly draw calcium through the compact by capillary action to disrupt a larger area of magnesium surface layer. The solid solubility of Mg in Ca is negligible. There is no homogeneity field for the Mg_2Ca compound. The Mg solidus is represented by an almost straight line originating from the melting point of Mg and terminating at 0.82 at.% Ca at 516.5°C. The low solubility of calcium in magnesium will impede the diffusion of calcium through magnesium particles. Glass formation in Mg-Ca alloys is occurred by rapid solidification. The complete glass phase in this system was formed in the composition range 57. 5 to 77.5 at.% Ca [43-45].

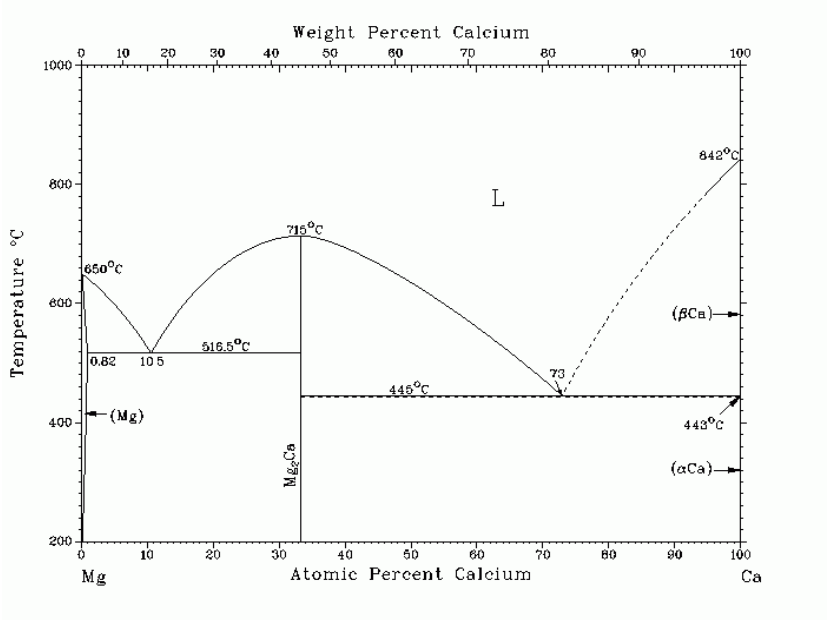

Figure 2.13: Magnesium rich corner of binary phase diagrams of Mg-Ca [43]

2.7.2.2 Mg-Sn System

Figure 2.14 shows the magnesium and tin binary phase diagram. Two eutectic reactions and a congruently melting line compound, Mg_2Sn, characterize the Mg-Sn system. The solubility

of Sn in Mg is restricted by the formation of the stable Mg_2Sn compound. The maximum solid solubility of Sn in Mg is at 3.35 at.% Sn and at 561.2°C. The maximum solid solubility of Mg in Sn appears to be infinitesimally small [58]. A metastable phase was found on the Sn-rich side of the Mg_2Sn compound. This phase appeared to be metastable from room temperature to ~150°C for Mg-rich specimens and from room temperature to ~325°C for Sn-rich specimens. The cubic Mg_2Sn, when exposed to temperatures of 600 to 1200°C and pressures of 2.5 to 5.5 GPa, transforms to a hexagonal structure. This transformation occurs readily and at a faster rate above 770.5°C, the melting point of Mg_2Sn at atmospheric pressure. Large grains of the new phase (hexagonal Mg_2Sn) were formed on cooling. The high-pressure structure can be preserved by quenching from a high temperature, followed by the release of pressure [58]. The addition of Sn is also known to reduce the degree of segregation formed during twin-roll casting, which has become the most efficient fabricating process for Mg alloy sheets.

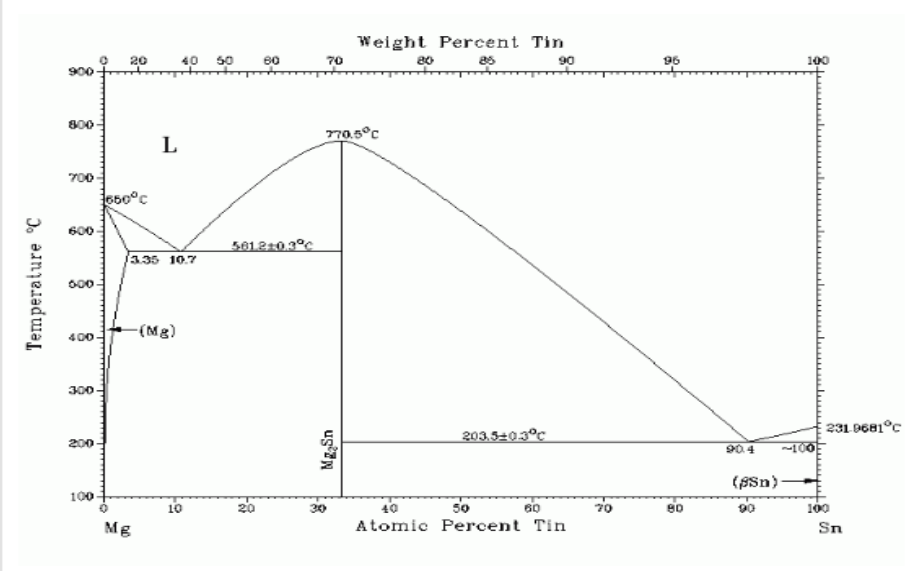

Figure 2.14: Magnesium rich corner of binary phase diagrams of Mg-Sn [58]

2.8 Effects of Tin in Deformation of Mg Alloys

Figure 2.15 shows the engineering stress-strain curves of (a) Mg alloy and (b) Sn containing Mg alloy, measured along the rolling direction (RD), transverse direction (TD), and 45° from the rolling direction. Mg alloy shows the highest strength (both yield and ultimate tensile) along the TD, followed by 45° and the RD. The uniform elongation value shows the opposite trend to that of strength, while the largest total elongation is obtained along 45°. Sn

containing Mg alloy shows slightly lower strength and larger elongation than Mg alloy when compared at the same specimen direction. Sn containing Mg alloy also shows quite similar behavior to that of Mg alloy in that the highest strength is obtained along the TD and the largest total elongation along 45°. Nevertheless, the difference in strength between the RD-loaded and TD-loaded specimens is smaller for Sn containing Mg alloy than for Mg alloy [24].

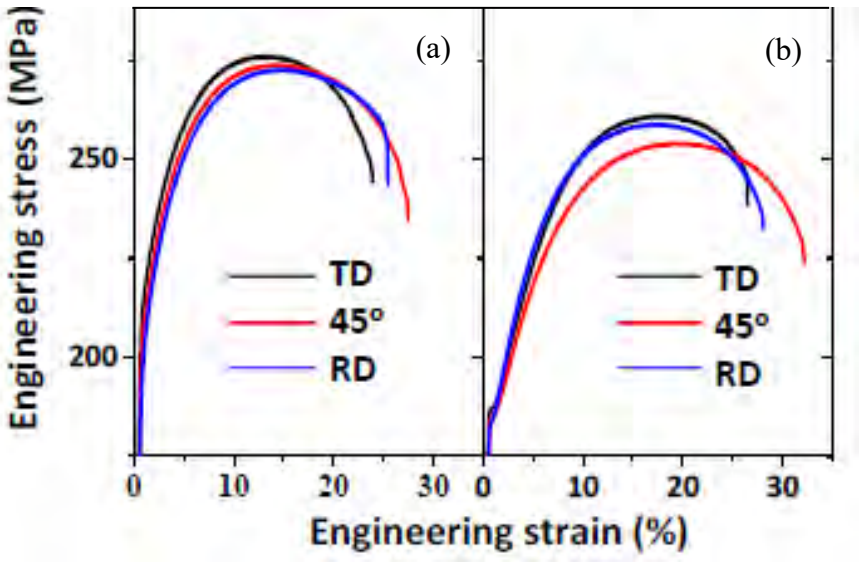

Figure 2.15: Engineering stress-strain curves of (a) Mg alloy and (b) Sn containing Mg alloy along the RD, 45°, and TD [24]

2.9 Effects of Tin on Microstructure

Figure 2.16 shows EBSD inverse pole figure (IPF) maps of as-annealed (a) Mg alloy and (b) Sn containing Mg alloy viewed along the transverse direction (TD); i.e., the viewing plane is the RD-ND plane. Average grain sizes of Mg alloy and Sn containing Mg alloy are 5.9 μm and 5.2 μm, respectively [24]. While the microstructure of Mg alloy is more or less uniform, the microstructure of Sn containing Mg alloy contains a small amount of grains elongated along the rolling direction (RD).

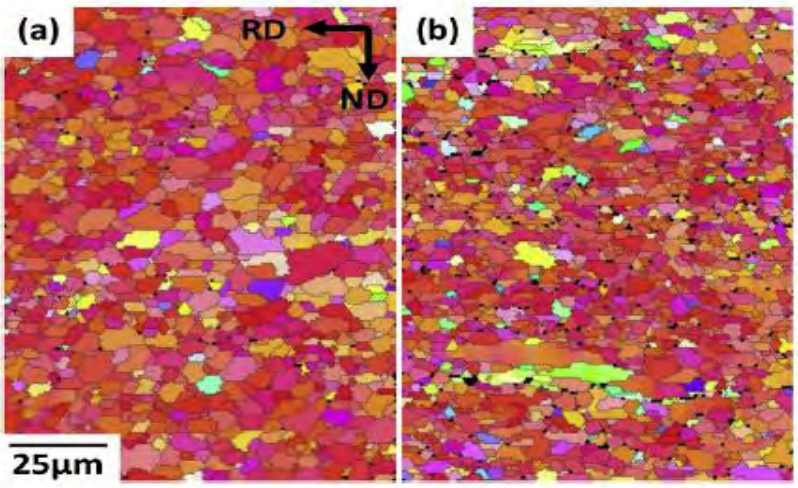

Figure 2.16: EBSD inverse pole figure (IPF) maps of (a) Mg alloy and (b) Sn containing Mg alloy [24]

Figure 2.17 shows the microstructure of the alloys after longitudinal tensile deformation to a strain of 10%. A small amount of tension twins is found to form in Mg alloy as shown in Figure 2.17(a) (marked by black dotted circles), while Sn containing Mg alloy does not show the formation of tension twins (Figure 2.17(b)).

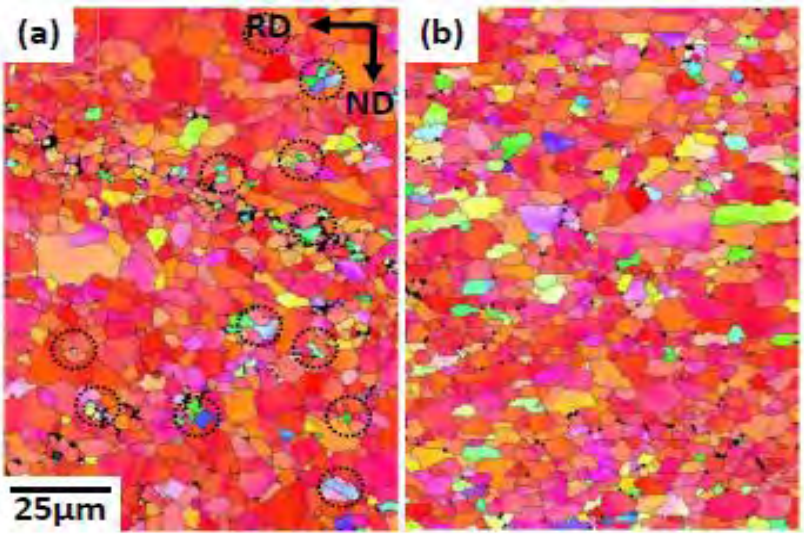

Figure 2.17: EBSD IPF maps of (a) Mg alloy and (b) Sn containing Mg alloy after tensile deformation (strain of 10%) along the RD [24]

Analyses of misorientation angles of the undeformed and deformed Mg alloy and Sn containing Mg alloy show that there is an increase in the number fraction of the misorientation angles near 86° after tensile deformation of Mg alloy, but virtually no increase in the case of Sn containing Mg alloy. These results indicate the active formation of tension

twins in Mg alloy during tensile deformation, but no tension twinning in Sn containing Mg alloy. Other types of twins like compression twin and double twin are not observed in both alloys [24].

2.10 Scope of the Work

The current work is focused on understanding the effects of Sn addition in binary Mg-Ca alloy system. The impact of Sn addition on microstructure of cast and rolled alloys will be investigated. Moreover, how different percentages of Sn addition modify the tensile strength and elongation to failure in different temperatures and strain rates will be perceived. Furthermore, dynamic grain growth will be studied to correlate underlying mechanisms of hot-deformation in the presence of Sn.

Chapter 3
Experimental Procedure

The following experimental procedure was conducted in the current work:

a) Samples were cast containing pure Mg ingot and pre-determined amounts of Ca and Sn.
b) Chemical compositions of these cast alloys were determined by X-ray fluorescence (XRF).
c) Chemical segregations were eliminated by homogenisation treatment.
d) Optical microscopy of these treated samples was carried out.
e) Hot Rolling (80% thickness reduction) was performed at 400^{o}C to obtain a recrystallized microstructure.
f) Optical microscopy of these rolled samples was carried out to examine microstructure.
g) SEM and EDX analysis were carried out to examine different phases.
h) Tensile tests were carried out at different temperatures (300, 350, 400 and 450˚C) on rolled sheets at different strain rates ($5x10^{-4}\ s^{-1}$ and $1x10^{-4}\ s^{-1}$).
i) Optical microscopy was carried out to examine microstructure and dynamic grain growth.
j) Strain hardening exponent, strain rate sensitivity index and activation energy were calculated to understand deformation mechanism.

3.1 Raw Materials

Mg-Ca alloy was used as a base alloy. For this, magnesium was attained from commercially available (99% Mg) magnesium ingots. Calcium granules of very good quality (99.99% pure) were used. Tin was used as an alloying element.

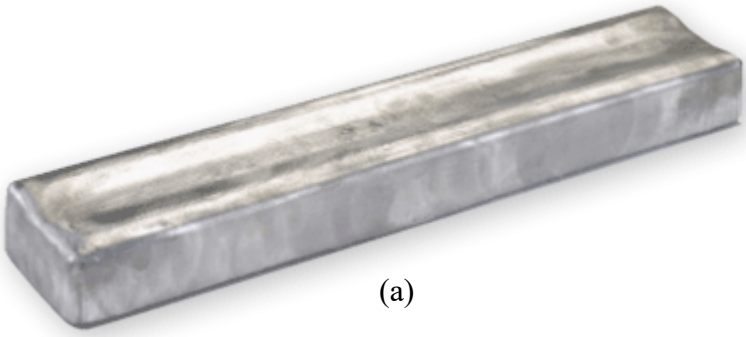

(a)

(b)

(c)

Figure 3.1: (a) Magnesium bar, (b) Ca granule and (c) Pure Sn

3.2 Casting

Casting was done in an induction furnace with the melting done in a ceramic crucible. Four alloys were cast. For each casting about 1 kg of raw materials were weighed. The raw materials were taken from its sources before casting and measured carefully. Amount of calcium and tin were adjusted so that the required composition is achieved after casting. The weight percentage of metals for each casting is given below.

Table 3.1: Raw materials for casting

Alloy	Sn	Ca	Mg
Mg-1Ca	-	1%	Balance
Mg-1Ca-1Sn	1%	1%	Balance
Mg-1Ca-2Sn	2%	1%	Balance
Mg-1Ca-4Sn	4%	1%	Balance

After taking right amount of material it was preheated at 150-200°C for 1-2 hours and then it was melted in the furnace. It was intermittently stirred to get a homogenous mixture and argon gas was applied over the melt as long as it was in the furnace until it was poured into the die. A metal die was used for each casting. The die dimension was 270mm x 120mm x 18 mm.

3.3 X-Ray Fluorescence

X-ray fluorescence (XRF) is an analytical technique used to determine the elemental composition of materials. XRF analyzers determine the chemistry of a sample by measuring the fluorescent (or secondary) X-ray emitted from a sample when it is excited by a primary X-ray source. For this test, a sequential X-ray fluorescence spectrometer (Model No: LAB CENTER XRF-1800) was used and 10mm x 10mm samples were made. XRF was used for all the alloys to evaluate compositions.

3.4 Homogenization

After casting of all four alloys, homogenization was carried out for all four alloys at 400°C for 21 hours followed by water quenching. It is assumed that at this temperature, porosities and flaws will minimize through high temperature diffusion. This heat treatment would result in a more homogenized structure. The furnace that was used was PROTHERM with a temperature controller (Model No: PC442T).

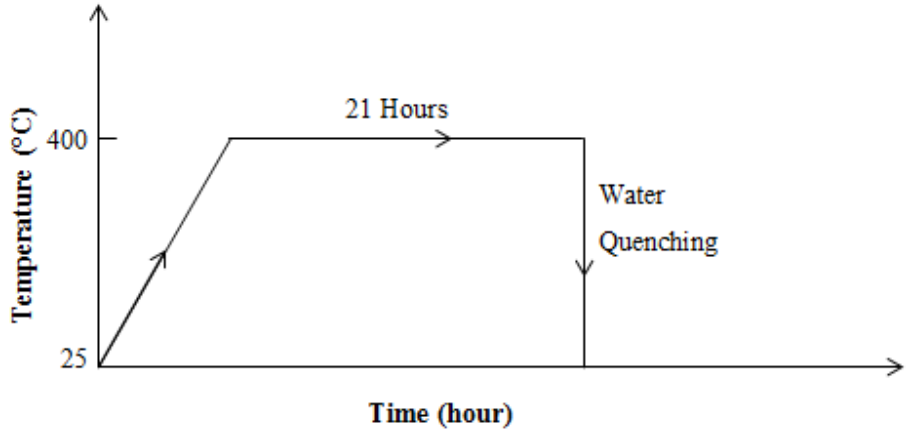

Figure 3.2: Homogenization of Mg alloys

3.5 Hot Rolling

Hot rolling means minimizing thickness through roller machine at a specific high temperature. This rolling was carried out using a roller machine with a motor (Model No: 225M-6) at 400°C. PROTHERM furnace was used to heat up the samples. Soaking time (holding time) at this temperature was 10 minutes. Then sample was passed through gap of two moving roller. After each pass, thickness was measured by slide calipers. Then again sample was kept in furnace for rising temperature. This procedure was followed up to final thickness of 2 mm. Initial thickness of samples was 12 mm. 80 percentage (%) reduction of thickness was conducted by this hot rolling.

3.6 Microstructural Observation

Microstructures are observed using light optical microscope. Samples were polished with different grades of emery papers. Then they were polished in polishing clothes with fine alumina powder. Microstructures were observed in etched conditions. Etching was done by 2% Nital solution. At first, the four alloys in as cast conditions were subjected for microscopic observations. Then the four rolled samples were subjected to above mentioned procedures to observe the microstructure.

3.7 Scanning Electron Microscopy

Scanning electron microscopy (SEM) was conducted to reveal imaging to see different phases. Samples were prepared of dimension (10mm x 10mm) and observed in unetched condition. Microstructures were observed in both secondary mode and backscattering modes. The machine used was JEOL JSM-7600F field emission SEM. This test was carried out only for rolled samples.

In addition, SEM system enables to obtain chemical information from a specimen by using various techniques, including by equipping the X-ray energy-dispersive spectrometer (EDS). The EDS micro-analyzer in an SEM that uses a primary electron beam to excite the emission of characteristic X-rays from the sample atoms. Since the electron beam can be readily focused on a microscopic area on a sample, the EDS micro-analyzer can examine

chemical compositions in a microscopic area.

3.8 Tensile Test

The tensile test was carried out in Testometric Materials Testing Machines (Model No: M500-50CT). Maximum load of this machine is 50 kN. The test was carried out at four different temperatures: 300, 350, 400 and 450˚C. Two strain rates were used: $5x10^{-4}$ and $1x10^{-4}$ s^{-1}. Tests were conducted on four rolled alloys (Mg-1Ca, Mg-1Ca-1Sn, Mg-1Ca-2Sn and Mg-1Ca-4Sn alloy) for four different temperatures and two strain rates. Therefore, a total of 32 samples of four alloys were examined.

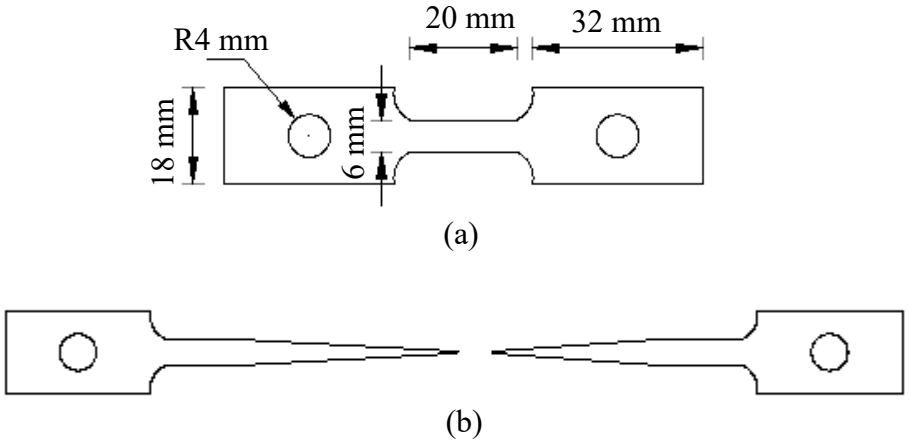

Figure 3.3: Sample (a) before and (b) after tensile test

The samples were gripped between the holders. After the samples were properly set, it was given time to reach the experimented temperature. After reaching the temperature, 20 minutes was waited prior to tensile test to stabilize the atmosphere. The sample was cooled naturally. The raw data was attained for further analysis. In Figure 3.3 (a) sample for tensile test and in Figure 3.3 (b) sample after tensile test are shown.

3.9 Dynamic Grain Growth Analysis

After tensile test, the fractured sample was observed by optical microscope for dynamic grain growth analysis. Samples were observed in etched condition. The observation was conducted along thickness of samples. Microstructure was taken in six different points of each sample. In Figure 3.4, six points of microstructural observation is shown. Point ‘a’ is on the static

region (grip). Points ‘b’, ‘c’, ‘d’, ‘e’ and ‘f’ are on the deformed region (gauge). By comparing grain size from these microstructures, dynamic grain growth can be analyzed. Different grain sizes were measured by using software during capturing optical microscopy imaging. Then average grain size was taken.

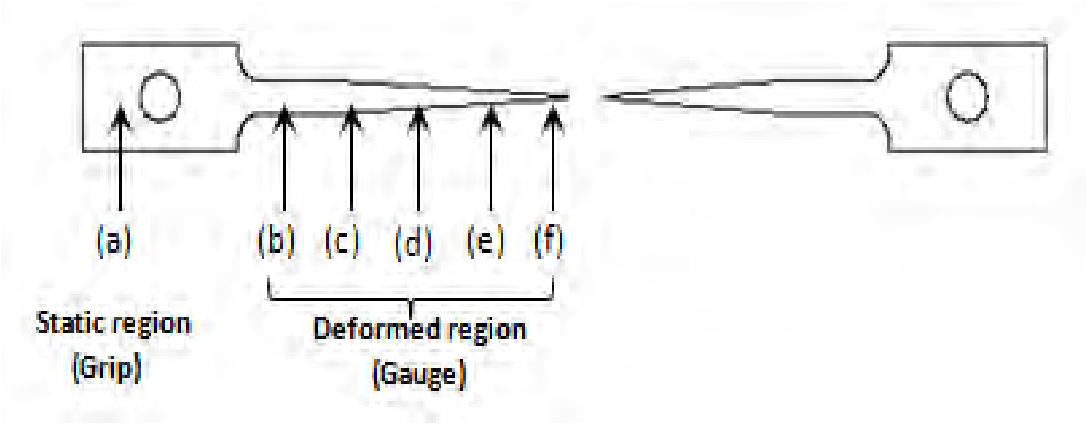

Figure 3.4: Different points of tensile tested sample for dynamic grain growth analysis

Chapter 4

Results and Discussions

4.1 Composition of the Alloys

After casting of samples, XRF was conducted so that compositions can be evaluated. The result of this test shows if the casting was properly done and the composition is matched. Four cast samples were taken for XRF. Results of XRF are shown from Tables 4.1 to 4.4.

Table 4.1: Compositions of Mg-1Ca cast alloy

Elements	Mg	Ca	Sn	Si	Al	Fe
Given %	Balance	1	0	0	0	0
XRF test (%)	Balance	0.85	0	0.10	0.05	0.01

Table 4.2: Compositions of Mg-1Ca-1Sn cast alloy

Elements	Mg	Ca	Sn	Si	Al	Fe
Given %	Balance	1	1	0	0	0
XRF test (%)	Balance	0.82	1.12	0.08	0.07	0.01

Table 4.3: Compositions of Mg-1Ca-2Sn cast alloy

Elements	Mg	Ca	Sn	Si	Al	Fe
Given %	Balance	1	2	0	0	0
XRF test (%)	Balance	0.93	2.08	0.05	0.05	0.01

Table 4.4: Compositions of Mg-1Ca-4Sn cast alloy

Elements	Mg	Ca	Sn	Si	Al	Fe
Given %	Balance	1	4	0	0	0
XRF test (%)	Balance	1.05	4.15	0.09	0.07	0.02

In Table 4.1, composition of Mg-1Ca alloy is shown. It is seen that percentages of elements from the test are not perfectly matched with the given percentages. Percentage of Ca was added 1%, but from test result 0.85% was found. This is due to elemental loss during casting. However, This difference of composition is very small (less than 0.2%). Therefore, this slightly difference of percentage can be ignored and it can be considered as Mg-1Ca alloy.

In Table 4.2, composition of Mg-1Ca-1Sn alloy is shown. Percentages of Ca and Sn were added 1% and 1% respectively, but from test result, percentages of these elements were found 0.82% and 1.12% respectively. Percentage of Ca decreased due to elemental loss. However, percentage of Sn increased. It is because, during casting, magnesium forms oxide. Because of this oxide formation, percentage of Mg decreases than the given percentage. During XRF analysis, as Mg percentage decreases, percentages of other elements can increase to make the total 100%. The differences of compositions of Ca and Sn are less than 0.2%. Therefore, these slightly differences of percentage can also be ignored and it can be considered as Mg-1Ca-1Sn alloy.

In Table 4.3, composition of Mg-1Ca-2Sn alloy is shown. Percentages of Ca and Sn were added 1% and 2% respectively, but from test result, percentages of these elements were found 0.93% and 2.08% respectively. The differences of compositions of Ca and Sn are less than 0.1%. Therefore, these slightly differences of percentage can also be ignored and it can be considered as Mg-1Ca-2Sn alloy.

In Table 4.4, composition of Mg-1Ca-4Sn alloy is shown. Percentages of Ca and Sn were added 1% and 4% respectively, but from test result, percentages of these elements were found 1.05% and 4.15% respectively. The differences of compositions of Ca and Sn are less than 0.2%. Therefore, these slightly differences of percentage can also be ignored and it can be considered as Mg-1Ca-4Sn alloy.

The elements having less than 0.1% Wt are assumed as trace elements. Since commercially pure Mg, Sn and Ca were used, there are possibilities of impurities. From Tables 4.1 to 4.4, it can be seen that Si, Al and Fe are also present in these alloys, but these elements are in very low amount (less than 0.1%). Therefore, these elements are considered as trace elements.

It is found that compositions of four alloys are in the limit of expectation.

4.2 Optical Microstructure Observation

Optical microstructures were taken from four alloys in both as cast conditions and after rolling. Difference between microstructures of as cast alloys and rolled alloys is clearly seen in Figures 4.1 and 4.2.

4.2.1 Microstructure of As-Cast Samples

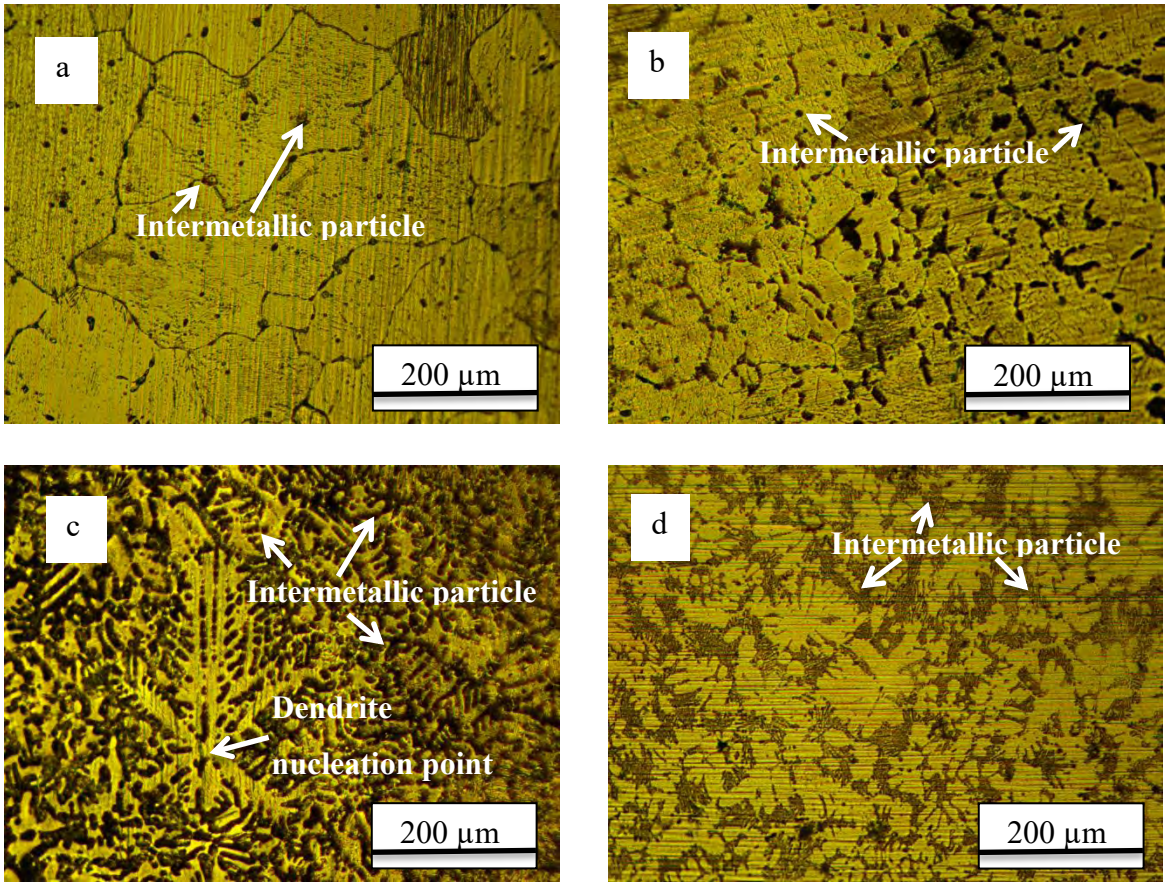

Figure 4.1: Optical microstructures of as-cast (a) Mg-1Ca (b) Mg-1Ca-1Sn (c) Mg-1Ca-2Sn (d) Mg-1Ca-4Sn alloy

Figure 4.1 shows the as-cast microstructures of the experimented alloys in homogenized condition. In Figure 4.1(a), no dendrite structure is found. However, with addition of Sn, dendrite formation happens. In Figure 4.1(b), 1% Sn is added and here start of dendrite formation is vividly clear. In Figures 4.1(c) and 4.1(d), 2% and 4% Sn is added respectively. Clear dendrite formation with nucleation point is found for 2% Sn addition. Further, for 4% Sn addition, very large dendrite arms are found. Primary intermetallic particles are observed at grain boundary and in the dendrite regions. Mendis and Tolnai also found dendrite formation with Sn addition in their work [46].

From microstructures of as-cast alloys, with addition of Sn, dendrite formation increased.

4.2.2 Microstructure of Rolled Samples

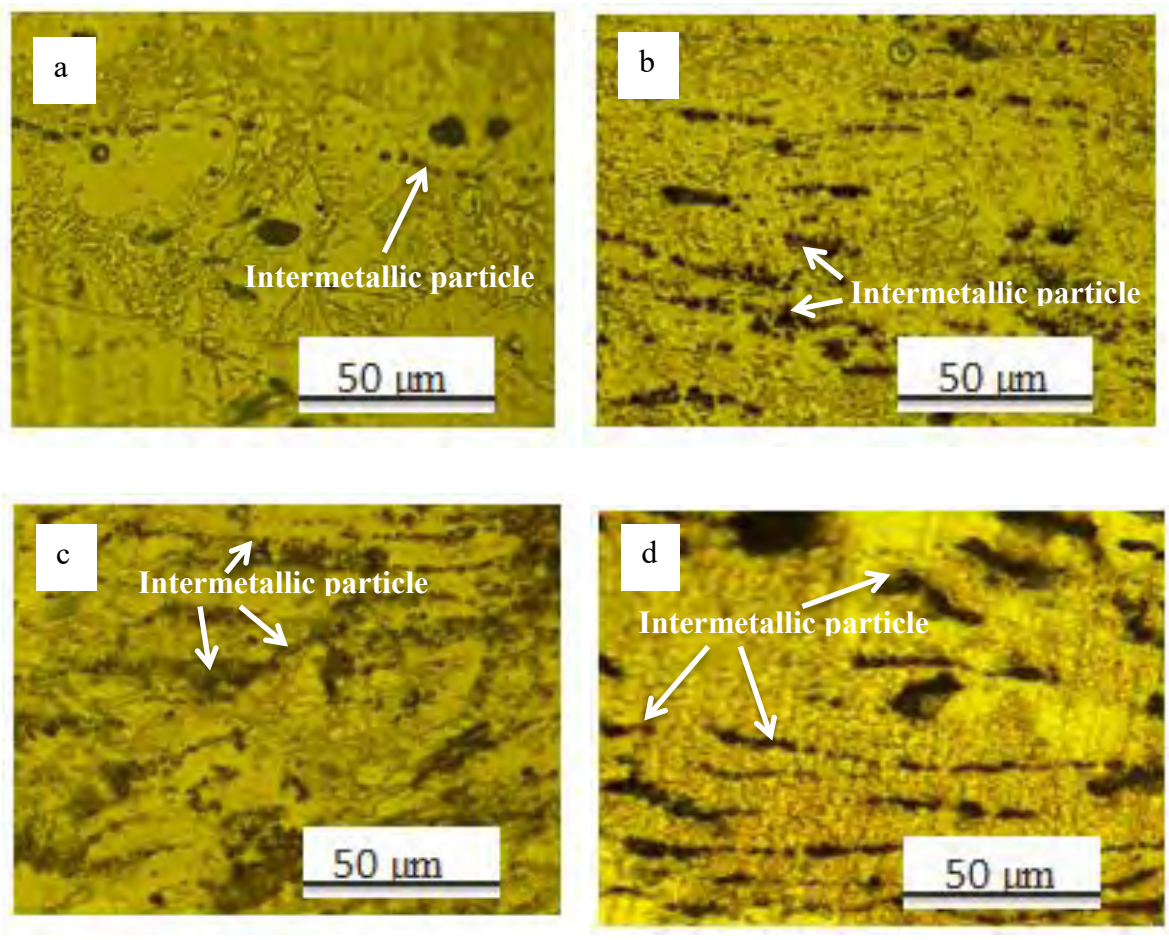

Figure 4.2: Optical microstructures of rolled (a) Mg-1Ca (b) Mg-1Ca-1Sn (c) Mg-1Ca-2Sn (d) Mg-1Ca-4Sn alloy

Figure 4.2 shows the microstructures of the rolled alloys. Grain size decreases after rolling. It is due to break down of grains and dynamic recrystallization during high temperature rolling. In Figure 4.2(a), microstructure of rolled Mg-1Ca alloy is shown. Grain size for this alloy is 15.35μm. Small amount of intermetallic particles is found in this alloy. In Figure 4.1(b), microstructure of rolled Mg-1Ca-1Sn alloy is shown. Grain size of this alloy is 10.2μm. Thus, 33.55% grain size reduction happens due to 1% Sn addition. Amounts of intermetallic particles are higher in this alloy than Mg-1Ca alloy. In Figures 4.2(c) and 4.2(d), microstructures of rolled Mg-1Ca-2Sn alloy and Mg-1Ca-4Sn alloy are shown respectively. For these two alloys, grain size is found 7.5μm and 2.3μm respectively. Very high intermetallic particles are found in these two alloys because of higher amount of Sn addition. Mendis [46] and Wang [47] also found the similar microstructures.

With addition of Sn, grain size decreased and amount of intermetallic particles increased.

4.3 SEM Observation with EDX

SEM revealed the phases with great depth of field and particle along with phase can easily be traceable with the data provided by the EDX. SEM imaging and EDX were only done in four rolled alloys. In Figure 4.3, SEM microstructures of rolled alloys are shown. EDX results are given in Appendix A. In Figure 4.3(a), SEM image of Mg-1Ca alloy is shown. In this micrograph, Mg matrix and only Mg_2Ca intermetallic particles are found. In Figure 4.3(b), SEM image of Mg-1Ca-1Sn alloy is shown. In this micrograph, Mg matrix and Mg_2Ca and CaMgSn intermetallic particles are found. Thus all Sn of 1% took place in the formation of CaMgSn particles in this alloy. In Figure 4.3(c), SEM image of Mg-1Ca-2Sn alloy is shown. With Mg_2Ca and CaMgSn particles, Mg_2Sn particle is found in this alloy. Thus, 2% addition of Sn not only formed CaMgSn particles, but also Mg_2Sn particles. In Figure 4.3(d), SEM image of Mg-1Ca-4Sn alloy is shown. In this alloy, excessive amounts of intermetallic particles are found. Mendis [46] and Wang [47] also reported the existence of high amount of intermetallic particles with addition of more Sn content.

Addition of Ca always forms Mg_2Ca particle. Addition of small amount of Sn with Ca, forms CaMgSn particle. Addition of Sn more than 1% forms both CaMgSn and Mg_2Sn particles [46].

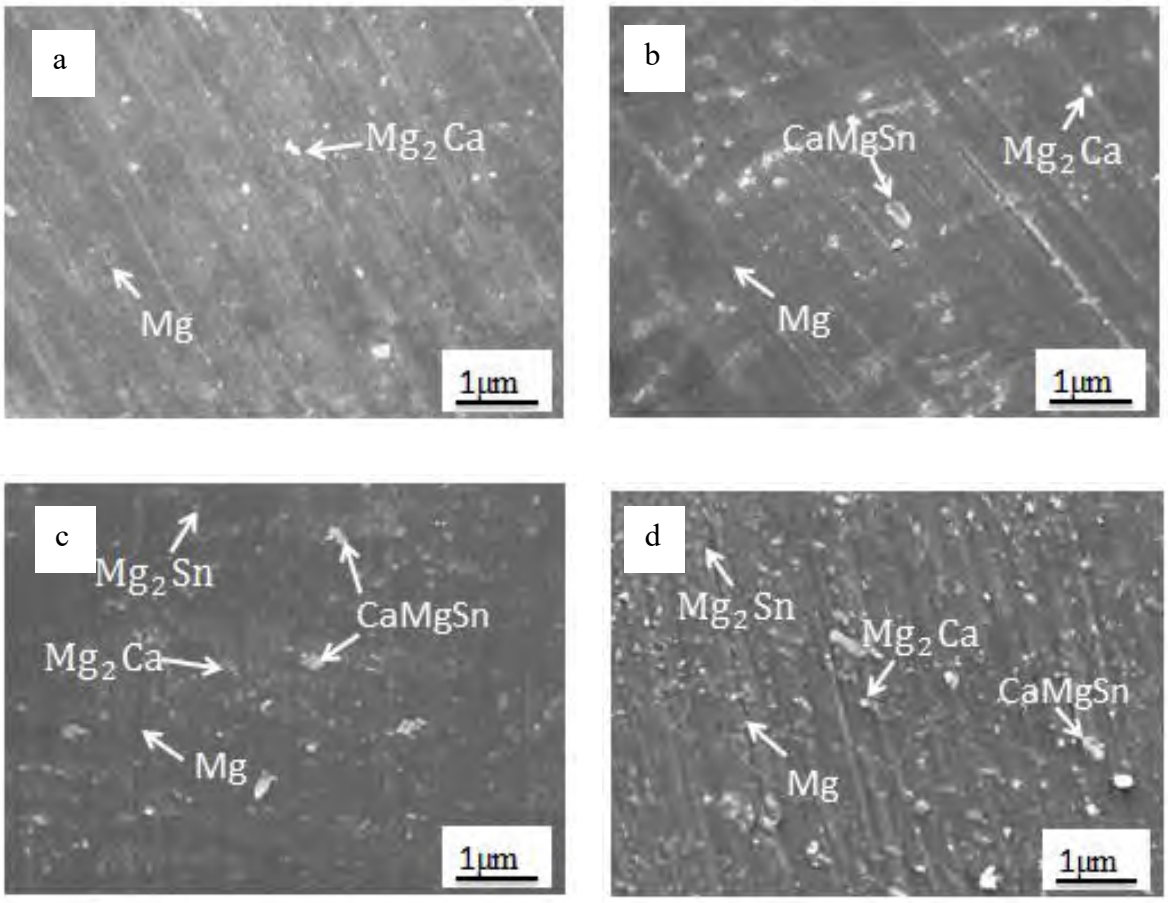

Figure 4.3: SEM image of rolled (a) Mg-1Ca (b) Mg-1Ca-1Sn (c) Mg-1Ca-2Sn (d) Mg-1Ca-4Sn alloy

4.5 Particle Size and Shape Distribution

In Figure 4.4, particle size and shape distribution are shown for Mg-1Ca alloy. In Figure 4.4(a), SEM image of this alloy is shown, and in Figure 4.4(b), only particles of the SEM image are shown. In Figures 4.4(c) and 4.4(d), particle size distribution and particle shape distribution are shown respectively. For particle size distribution, count versus particle size is plotted. From this plot, mean particle size and standard deviation are calculated. Particle size is found about 0.51 μm. For particle shape distribution, count versus circularity is plotted. From this plot mean circularity and standard deviation is calculated. Circularity 1 means particle shape is pure circular. For Mg-1Ca alloy, circularity is found about 0.8. Thus, particle slightly deviates from pure circular in shape.

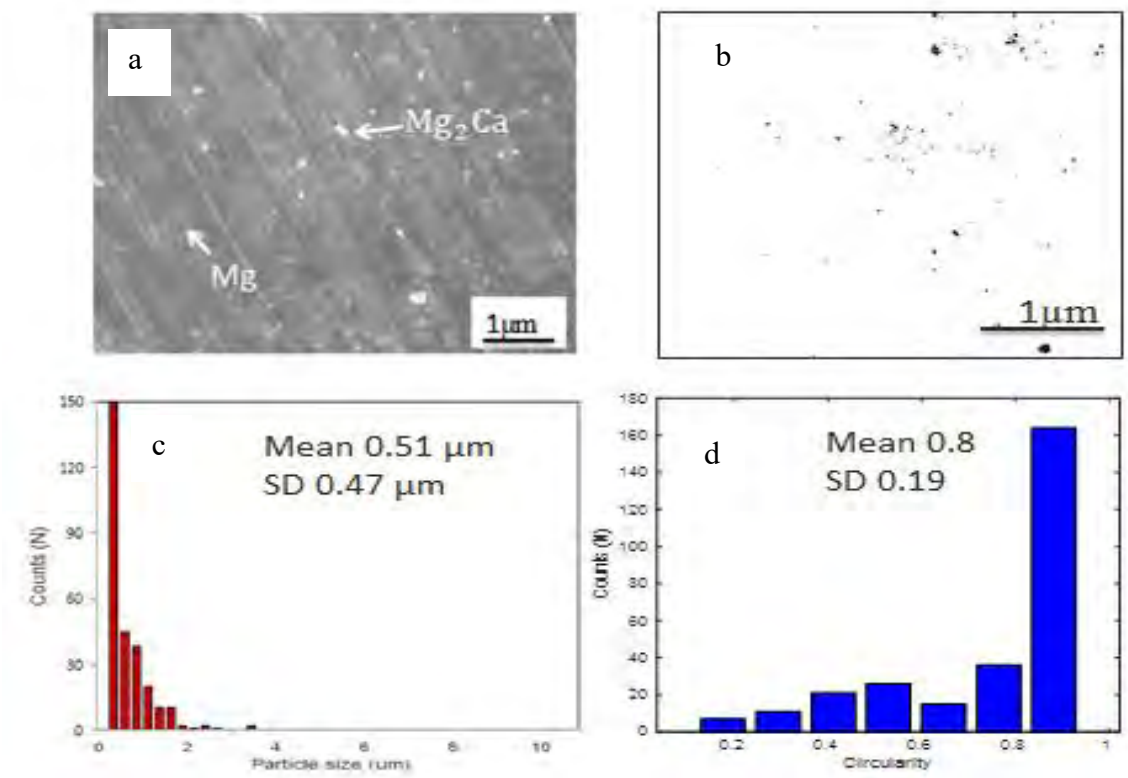

Figure 4.4: Mg-1Ca rolled alloy (a) SEM image (b) Image showing only Particle (c) Particle size distribution (d) Particle shape distribution

In Figure 4.5, particle size and shape distribution are shown for Mg-1Ca-1Sn alloy. In Figure 4.5(a), SEM image of this alloy is shown, and in Figure 4.5(b), only particles of the SEM image are shown. In Figures 4.5(c) and 4.5(d), particle size distribution and particle shape distribution are shown respectively. From count versus particle size plot, particle size is found about 0.71 µm. From count versus circularity plot, circularity is found about 0.84. With addition of Sn, CaMgSn particle appears which is very coarse. For this coarse particle, overall particle size increased. Further, circularity increased which indicates particle becomes more circular with addition 1% Sn content.

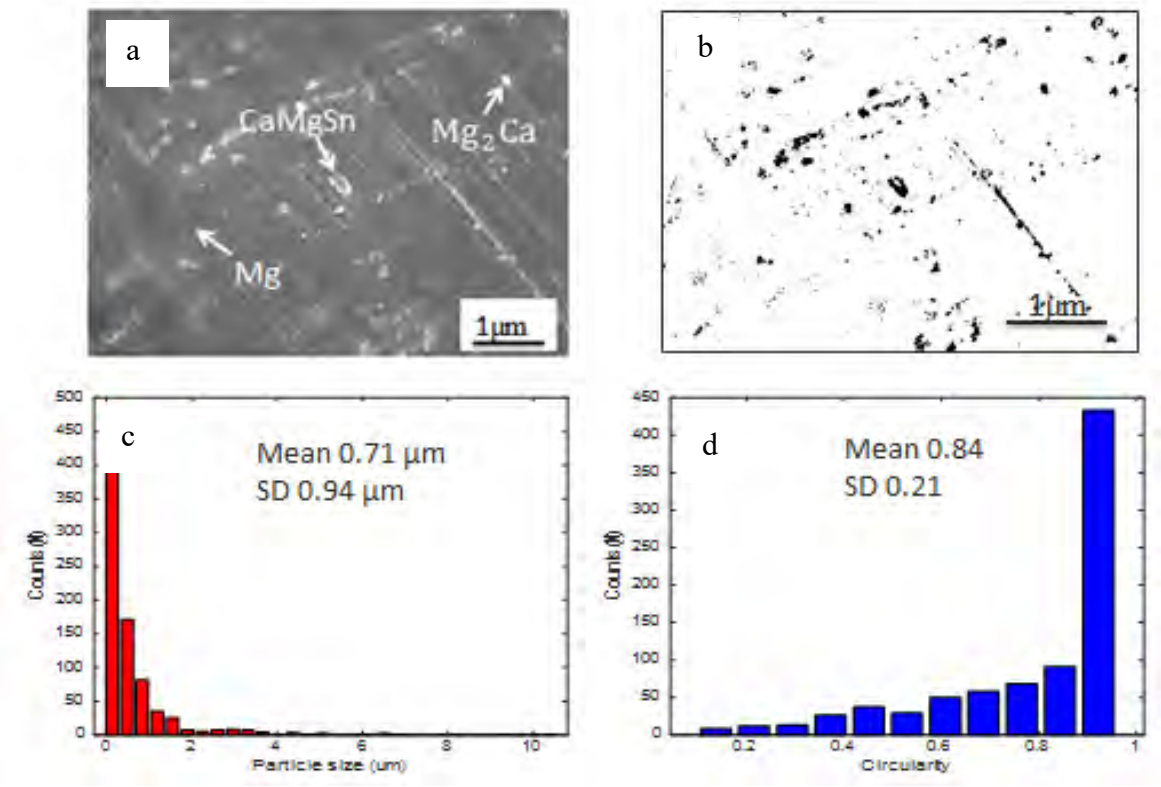

Figure 4.5: Mg-1Ca-1Sn rolled alloy (a) SEM image (b) Image showing only Particle (c) Particle size distribution (d) Particle shape distribution

In Figure 4.6, particle size and shape distribution are shown for Mg-1Ca-2Sn alloy. In Figure 4.6(a), SEM image of this alloy is shown, and, in Figure 4.6(b), only particles of the SEM image are shown. In Figures 4.6(c) and 4.6(d), particle size distribution and particle shape distribution are shown respectively. From count versus particle size plot, particle size is found about 0.58 μm. From count versus circularity plot, circularity is found about 0.88. With addition of more Sn, with CaMgSn particle, another particle Mg_2Sn appears which is very small. For this small particle, overall particle size decreased. However, circularity increased more which indicates particle becomes more circular with addition 2% Sn content.

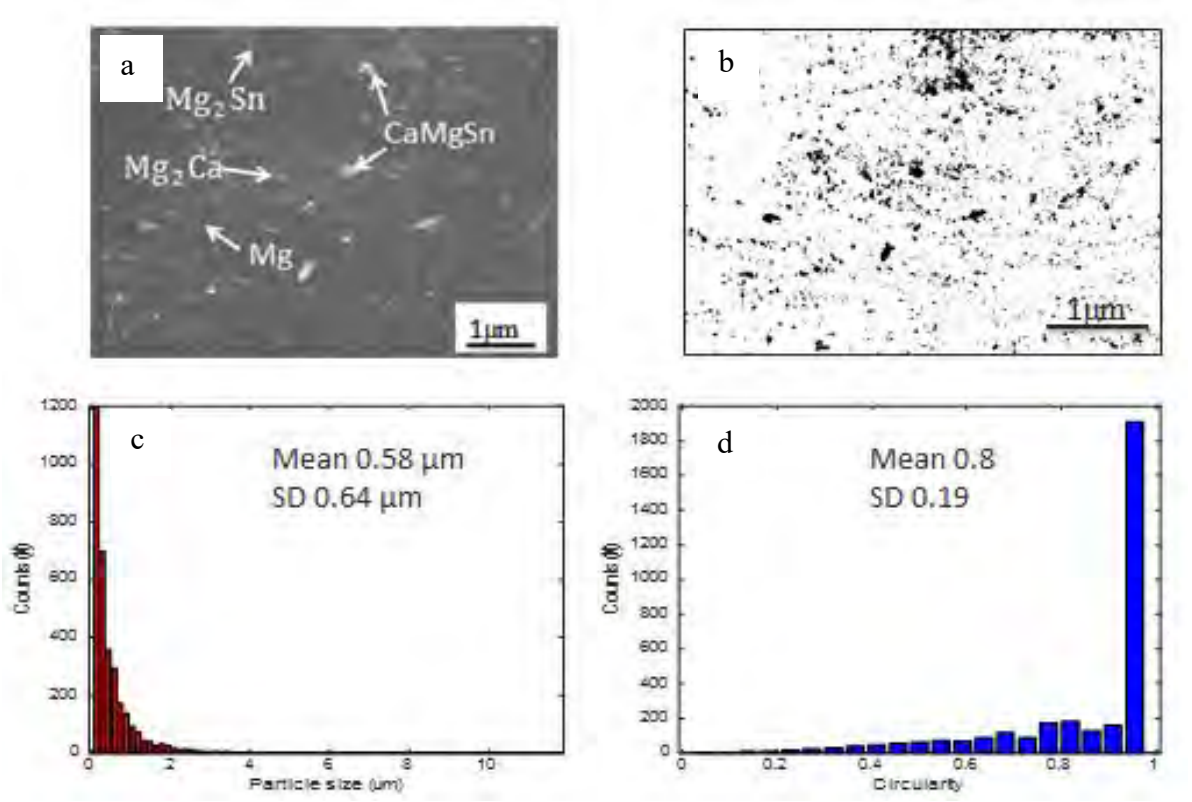

Figure 4.6: Mg-1Ca-2Sn rolled alloy (a) SEM image (b) Image showing only Particle (c) Particle size distribution (d) Particle shape distribution

In Figure 4.7, particle size and shape distribution are shown for Mg-1Ca-4Sn alloy. In Figure 4.7(a), SEM image of this alloy is shown, and, in Figure 4.7(b), only particles of the SEM image are shown. In Figures 4.7(c) and 4.7(d), particle size distribution and particle shape distribution are shown respectively. Particle size is found about 0.57 µm and circularity is found about 0.87. With addition of 4% Sn, excessive amounts of intermetallic particle forms. Among these particles, amount of Mg_2Sn particle is large which size is very small. For this small size particle formation, overall particle size decreased. However, circularity slightly decreases. Wang reported similar particle size in his work [47] and Ho-Kyung Kim reported particle size distribution in his work on Mg alloy [48].

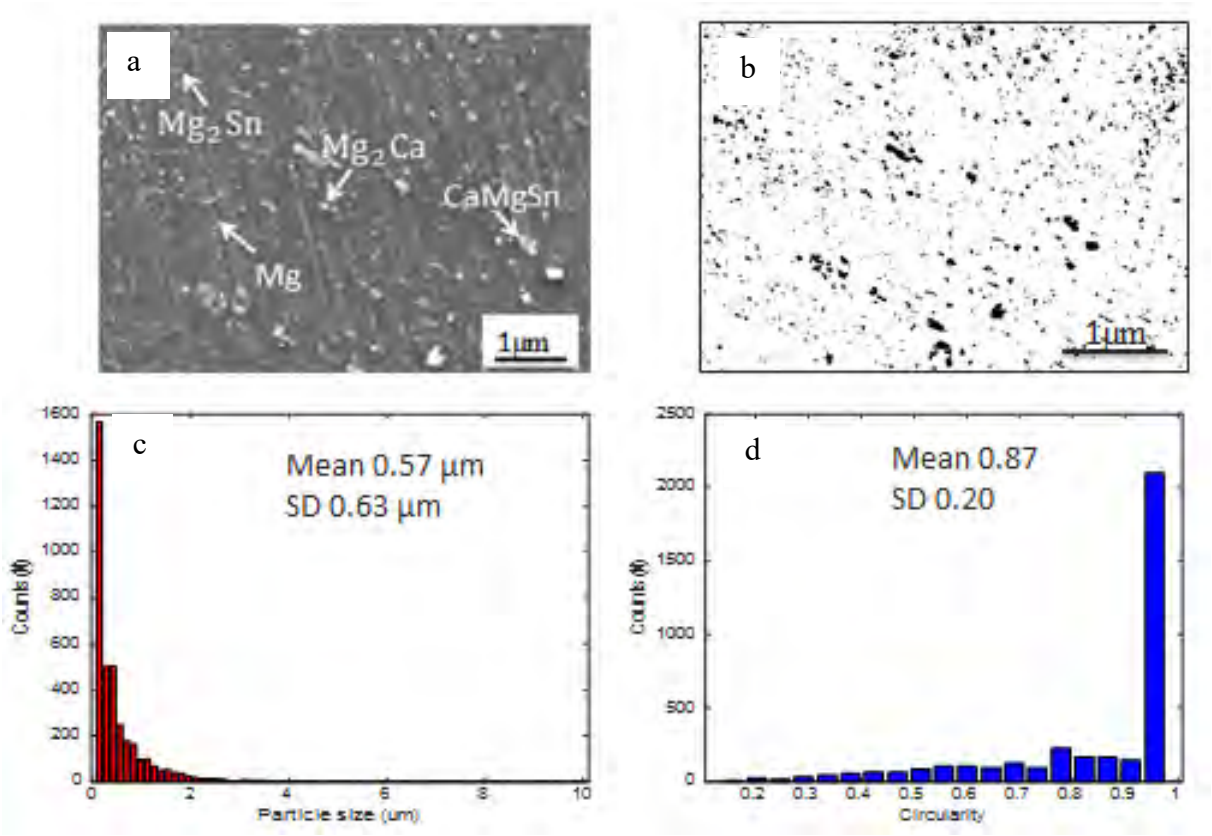

Figure 4.7: Mg-1Ca-4Sn rolled alloy (a) SEM image (b) Image showing only Particle (c) Particle size distribution (d) Particle shape distribution

Particle size and shape variation with Sn content is shown in Figure 4.8. With addition of 1% Sn content both particle size and circularity increased because of large CaMgSn particle formation. With addition of 2% Sn, particle size decreased because of small Mg_2Sn particle formation and with addition of 4% Sn, particle size decreased more because of more Mg_2Sn particle formation. Circularity increased with 2% Sn addition as before but with 4% Sn addition excessive amount of particle formation that deviates slightly from circularity.

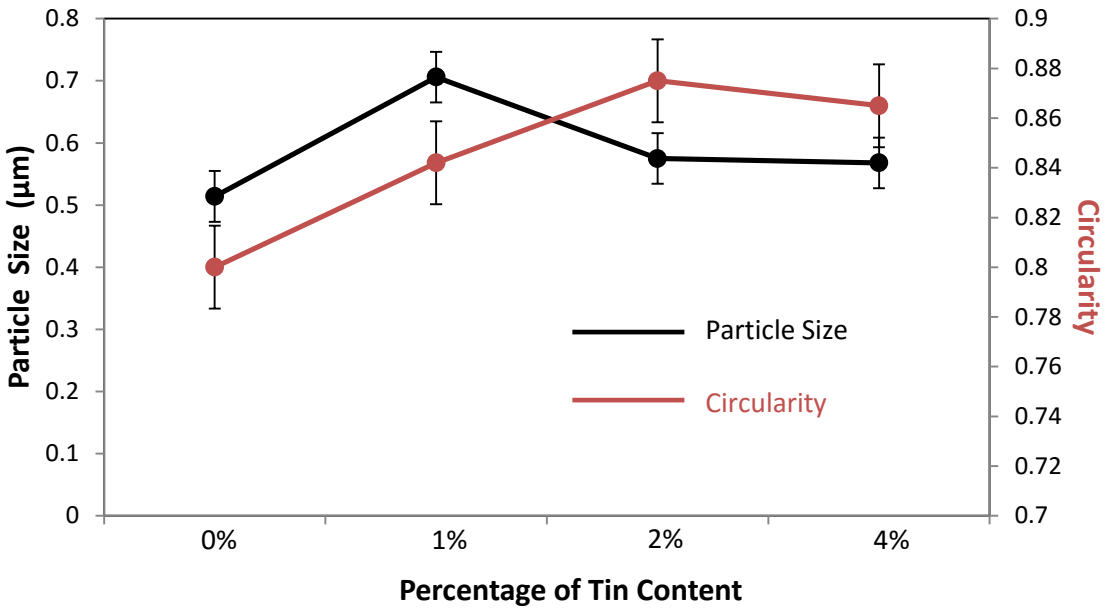

Figure 4.8: Particle size and shape variation with percentage of Sn content

It is found that with increasing Sn addition upto 1%, particle size increased. With more Sn addition, particle size decreased. Furthermore, with addition of Sn, particle shape becomes more circular. However, with excessive Sn addition, particle slightly deviated from circularity.

4.5 Tensile Test Results

4.5.1 Tensile Test Result at Strain Rate $5x10^{-4}$ s^{-1}

In Figure 4.9, tensile strength versus elongation to failure (%) curves are shown for four alloys at strain rate of $5x10^{-4}$ s^{-1} at four different temperatures (300, 350, 400 and 450°C). In Figure 4.9(a), tensile strength versus elongation to failure curves is shown for Mg-1Ca alloy. From this figure, it is found that for temperature 300°C, alloy showed ultimate tensile strength 50.30 MPa and elongation to failure 17.80%. When temperature increased to 350°C, alloy becomes soft and its ultimate tensile strength decreased to 25.46 MPa and elongation to failure increased to 72.68%. With increasing temperature more to 400°C, strength decreased more to 16.32 MPa and elongation to failure increased more to 100.02%. However, with increasing temperature more above 400°C, oxide formation happens and alloy degrades its

properties. Because of this, at 450°C, ultimate tensile strength decreased to 7.65 MPa and elongation to failure decreased to 68.86%.

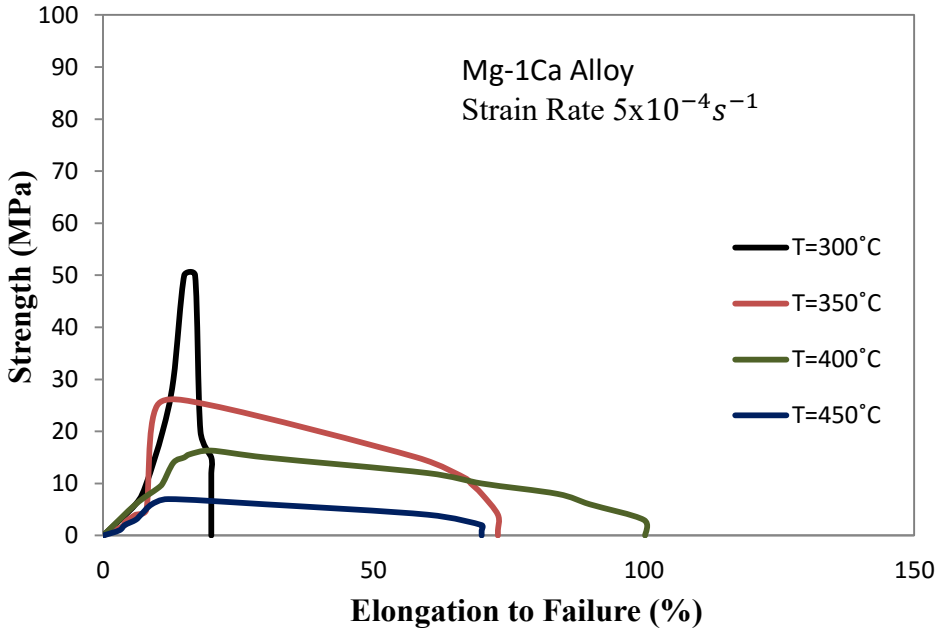

Figure 4.9(a): Tensile Strength versus Elongation to failure (%) curve at strain rate $5x10^{-4}$ s^{-1} for Mg-1Ca alloy

In Figure 4.9(b), tensile strength versus elongation to failure curves are shown for Mg-1Ca-1Sn alloy at strain rate of $5x10^{-4}$ s^{-1}. From this figure, it is found that for temperature 300°C, alloy showed ultimate tensile strength 92.16 MPa and elongation to failure 53.23%. Both ultimate tensile strength and elongation to failure increased compared to that of Mg-1Ca alloy. It is believed to be due to 1% Sn addition, grain size decreased. For this grain size reduction, number of grains per unit volume increased. So, the same strain deformation can be dispersed to more grains which result in a more uniform deformation and the decreased of stress concentration. Therefore, strength and elongation to failure improved. This is also reported by other researchers [47, 62]. When temperature increased to 350°C and 400°C, alloy becomes soft and relaxed due to diffusional activity, and its ultimate tensile strength decreased to 20.62 MPa and 10.13 MPa respectively and elongation to failure increased to 97.65% and 116.41% respectively. Elongation to failure increased 34.36% at 350°C and 16.39% at 400°C than that for Mg-1Ca alloy. Because of 1% Sn addition, CaMgSn particle is found in alloy. This particle is thermally stable so elongation to failure increases but coarse CaMgSn phase with cluster morphology decreased ultimate tensile strength [47]. With increasing temperature to 450°C, ultimate tensile strength is found 22.96 MPa and elongation

to failure is increased to 130.18%. Solubility of Ca in Mg matrix was increased by small amount of Sn addition which results in solid solution strengthening [47].

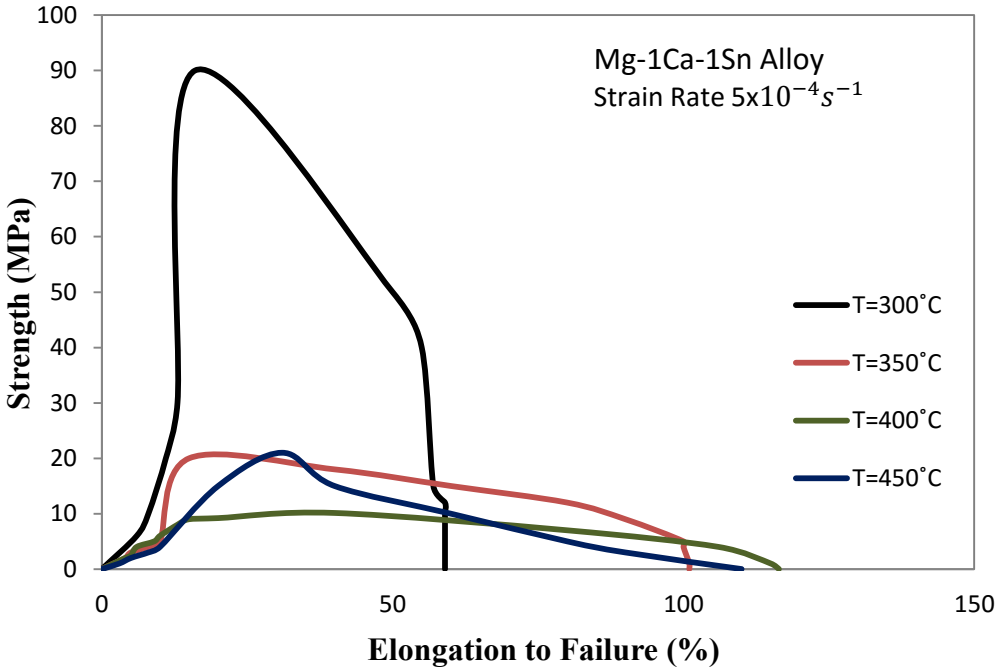

Figure 4.9(b): Tensile Strength versus Elongation to failure (%) curve at strain rate $5x10^{-4}$ s^{-1} for Mg-1Ca-1Sn alloy

In Figure 4.9(c), tensile strength versus elongation to failure curves are shown for Mg-1Ca-2Sn alloy at strain rate of $5x10^{-4}$ s^{-1}. From this figure, it is found that for temperature 300°C, alloy showed ultimate tensile strength 33.69 MPa and elongation to failure 34.08%. Both ultimate tensile strength and elongation to failure decreased than Mg-1Ca-1Sn alloy. It is due to 2% Sn addition, solubility of Ca in Mg matrix decreased with high amount of Sn addition [47]. Hence, effect of solid solution strengthening in Mg-1Ca-2Sn alloy is weaker than that for Mg-1Ca-1Sn alloy. When temperature increased to 350, 400 and 450°C, ultimate tensile strength decreased and elongation to failure increased as the alloy becomes soft. The ultimate tensile strength is found decreased to 20.30 MPa, 14.70 MPa and 9.25 MPa respectfully. Elongation to failure increased to 39.71%, 59.13% and 70.32% respectively.

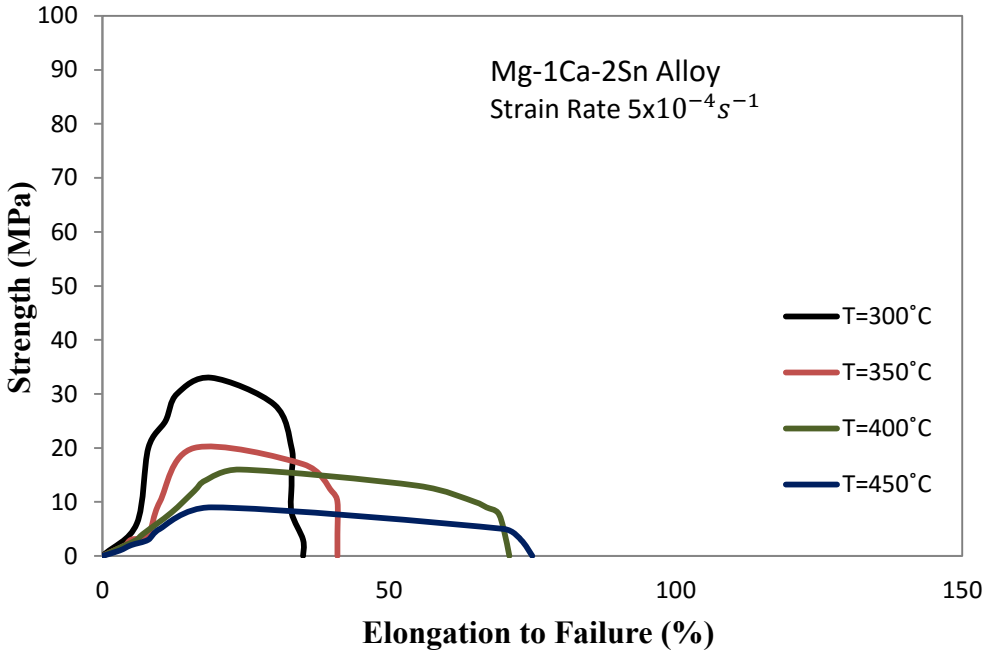

Figure 4.9(c): Tensile Strength versus Elongation to failure (%) curve at strain rate $5x10^{-4}$ s^{-1} for Mg-1Ca-2Sn alloy

In Figure 4.9(d), tensile strength versus elongation to failure curves is shown for Mg-1Ca-4Sn alloy at strain rate of $5x10^{-4}$ s^{-1}. At 300°C, ultimate tensile strength and elongation to failure are found 9.07 MPa and 12.02% respectively. At 350°C, ultimate tensile strength and elongation to failure are found 16.87 MPa and 12.52% respectively. At 400°C, ultimate tensile strength and elongation to failure are found 8.61 MPa and 26.72% respectively. At 450°C, ultimate tensile strength and elongation to failure are found 12.81 MPa and 83.30% respectively. Due to 4% Sn addition, excessive amounts of primary intermetallic particles formed and tensile properties deteriorated. So, from Figure 4.9(d), it is found that for each temperature alloy showed very poor tensile properties.

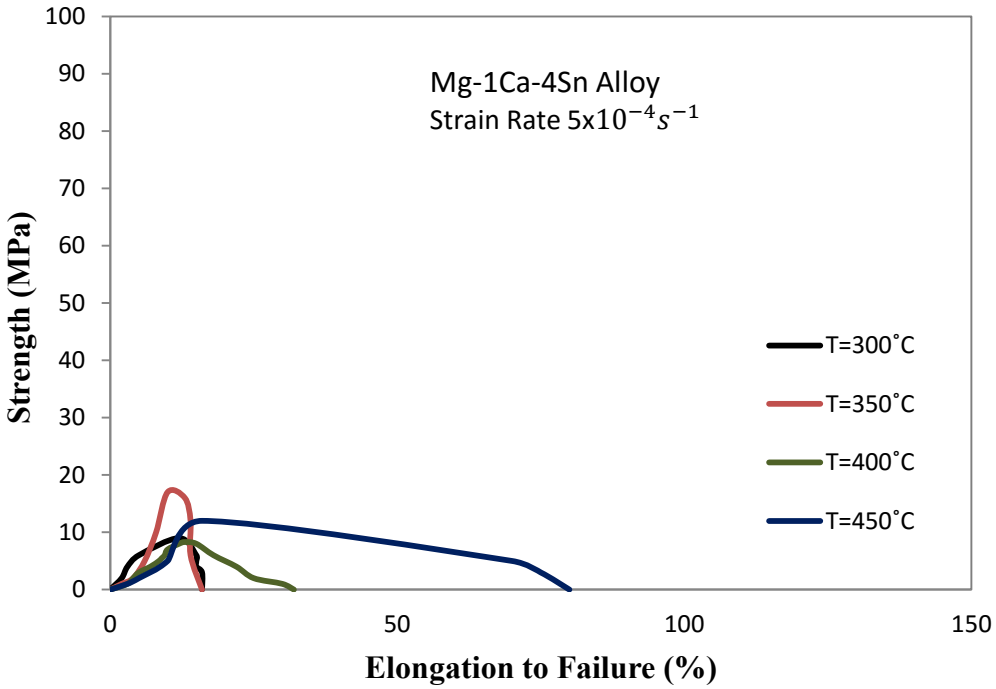

Figure 4.9(d): Tensile Strength versus Elongation to failure (%) curve at strain rate $5x10^{-4}$ s^{-1} for Mg-1Ca-4Sn alloy

At strain rate $5x10^{-4}$ s^{-1}, with addition of 1% Sn, both tensile strength and elongation to failure increased. However, with 2% and 4% Sn addition, both of these properties decreased, because of excessive primary intermetallic particles formation. With increasing temperature upto 400°C for all alloys, tensile strength decreased, while elongation to failure increased. Above 400°C, elongation to failure decreased, due to oxide formation.

4.5.2 Tensile Test Result at Strain Rate $1x10^{-4}$ s^{-1}

In Figure 4.10, tensile strength versus elongation to failure (%) curves are shown for four alloys at strain rate of $1x10^{-4}$ s^{-1} at four different temperatures (300, 350, 400 and 450°C). In Figure 4.10(a), tensile strength versus elongation to failure curves is shown for Mg-1Ca alloy. From this figure, it is found that at temperature 300°C, this alloy showed ultimate tensile strength 28.62 MPa and elongation to failure 95.9%. Ultimate tensile strength decreased than strain rate $5x10^{-4}$ s^{-1} and elongation to failure increased than strain rate $5x10^{-4}$ s^{-1}. This is because at slower strain rate grain gets more time to grow that can retard the onset of necking during tensile test [49]. When temperature increased to 350°C, its ultimate tensile strength decreased to 18.70 MPa and elongation to failure is found 90%. With increasing temperature more to 400°C, strength decreased more to 12.25 MPa and elongation

to failure is found 88.24% and at temperature 450°C, ultimate tensile strength and elongation to failure are found 13.75 MPa and 95% respectively.

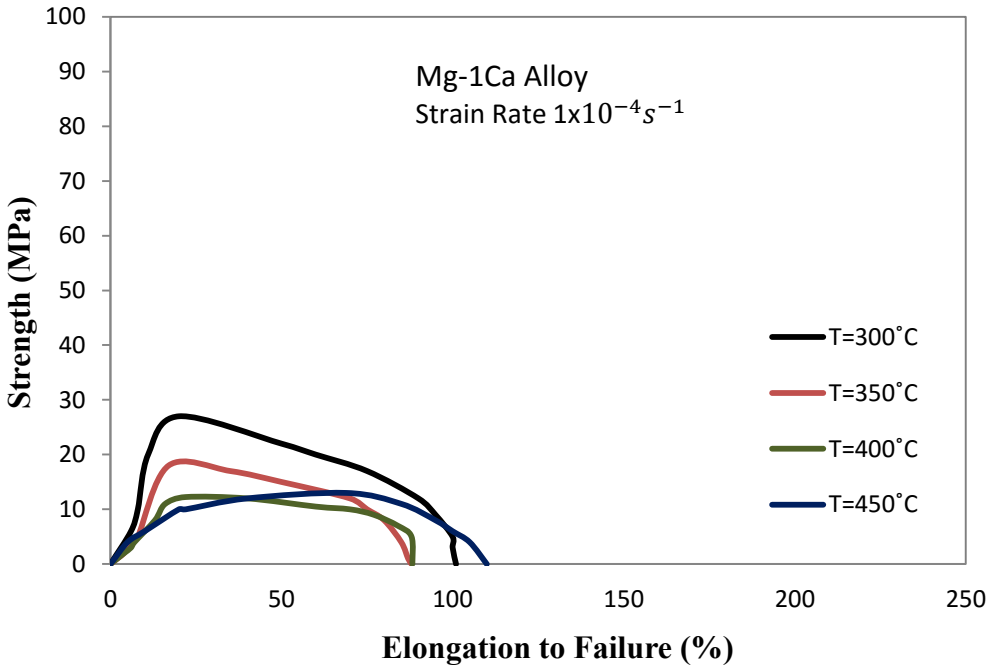

Figure 4.10(a): Tensile Strength versus Elongation to failure (%) curve at strain rate $1x10^{-4}$ s^{-1} for Mg-1Ca alloy

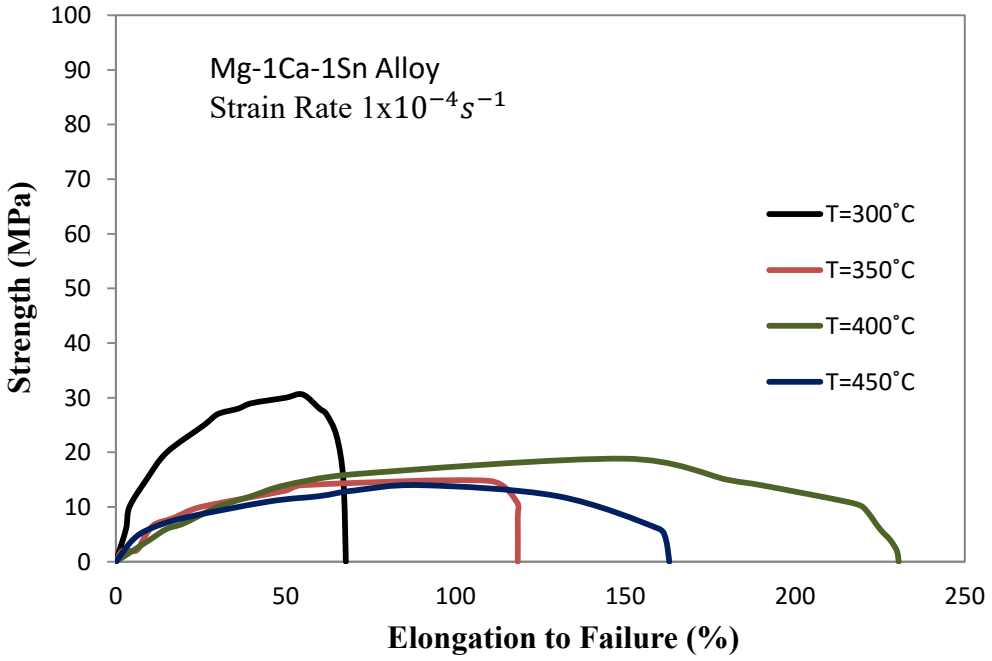

Figure 4.10(b): Tensile Strength versus Elongation to failure (%) curve at strain rate $1x10^{-4}$ s^{-1} for Mg-1Ca-1Sn alloy

In Figure 4.10(b), tensile strength versus elongation to failure curves are shown for Mg-1Ca-1Sn alloy at strain rate of $1x10^{-4}$ s^{-1}. From this figure, it is found that at temperature 300°C, alloy showed ultimate tensile strength 30.54 MPa and elongation to failure 67.74%. When temperature increased to 350°C and 400°C, alloy becomes relaxed and its ultimate tensile strength decreased to 14.78 MPa and 18.84 MPa respectively and elongation to failure increased to 118.36% and 230.55% respectively. With increasing temperature more to 450°C, ultimate tensile strength is found 14.01 MPa and elongation to failure is found 162.91%. 1% Sn addition decreases grain sizes. However, at slower strain rate grain growth occurs. This grain growh gives a decrease in ultimate tensile strength, but an increase in elongation to failure. Other researchers also found simillar results [49, 50].

In Figure 4.10(c), tensile strength versus elongation to failure curves are shown for Mg-1Ca-2Sn alloy at strain rate of $1x10^{-4}$ s^{-1}. From this figure, it is found that for temperature 300°C, alloy showed ultimate tensile strength 31.92 MPa and elongation to failure 43.67%. When temperature increased to 350, 400 and 450°C, ultimate tensile strength is found decreased to 11.50 MPa, 17.51 MPa and 12.04 MPa respectively. Elongation to failure increased to 52.57%, 150.64% and 105.50% respectively. With 2% Sn addition, large amount of intermetallic particles formed and solubility of Ca decreased. So, tensile properties degraded. However, at high temperature, large grain growth happened. This was attributed

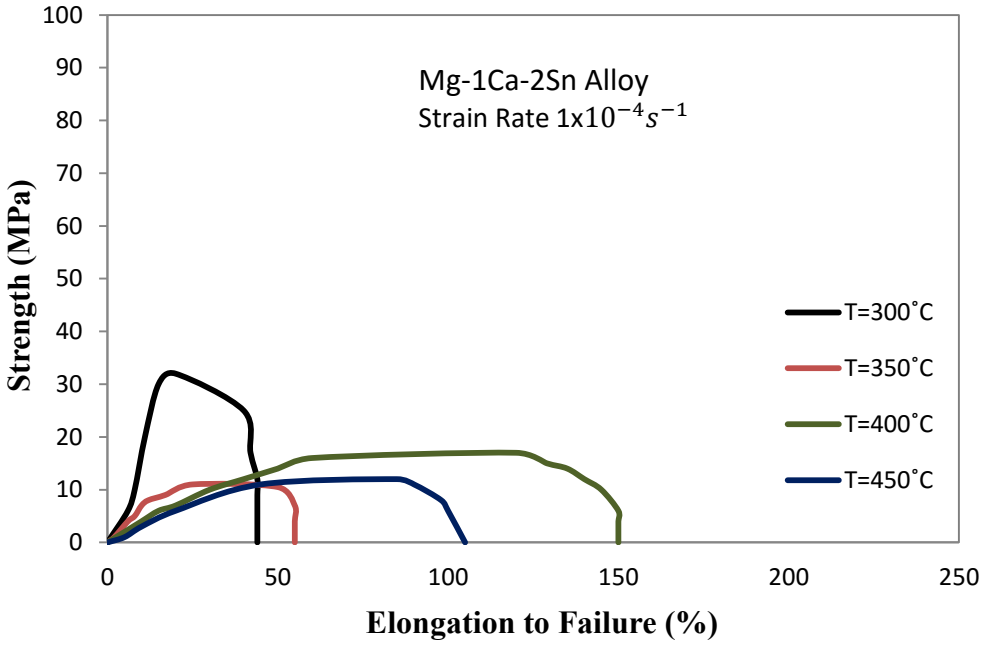

Figure 4.10(c): Tensile Strength versus Elongation to failure (%) curve at strain rate $1x10^{-4}$ s^{-1} for Mg-1Ca-2Sn alloy

for large elongation to failure.

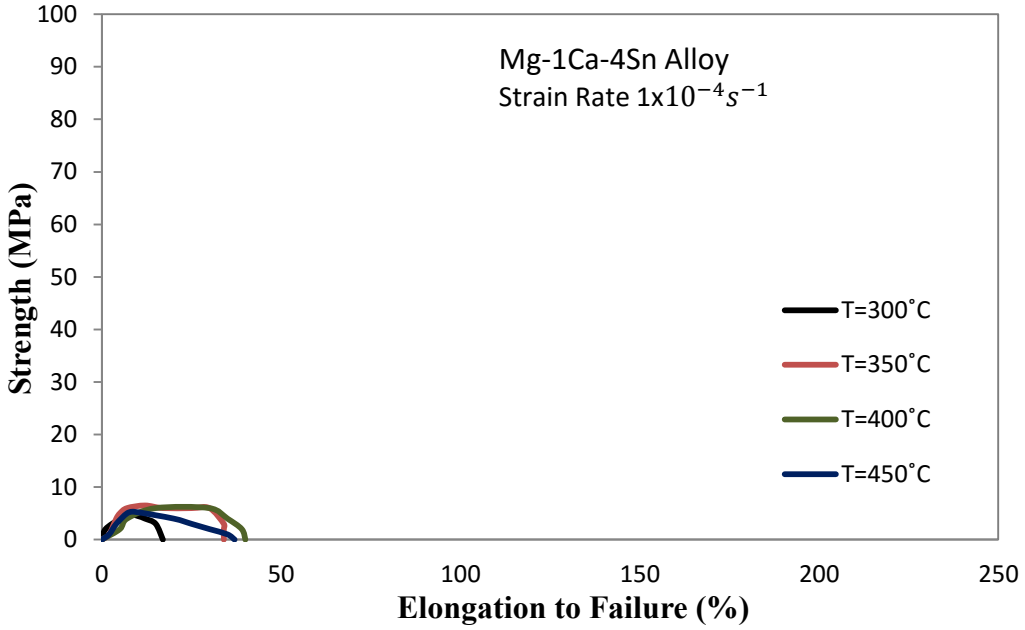

Figure 4.10(d): Tensile Strength versus Elongation to failure (%) curve at strain rate $1x10^{-4}$ s^{-1} for Mg-1Ca-4Sn alloy

Figure 4.11: Oxide formation of Mg-1Ca-4Sn alloy during tensile test at 450°C and strain rate $1x10^{-4}$ s^{-1}

In Figure 4.10(d), tensile strength versus elongation to failure curves is shown for Mg-1Ca-4Sn alloy at strain rate of $1x10^{-4}$ s^{-1}. Excessive amounts of primary intermetallic particles formed with 4% Sn addition. At slower strain rate, these intermetallic formed oxide [Figure 4.11]. Because of this, at slower strain rate and at high temperature properties of Mg-1Ca-4Sn

alloy totally deteriorated. This results a very small ultimate tensile strength and elongation to failure [Figure 4.10(d)].

At strain rate $1x10^{-4}$ s^{-1}, with increasing Sn addition, tensile strength decreased, and elongation to failure increased, due to higher grain growth. With increasing temperature, tensile strength decreased more, and elongation to failure increased more. However, at 450°C, because of formation of oxide, these properties totally collapsed.

4.5.3. Comparison between Two Strain Rates

In Figure 4.12, tensile strength variation with tin content at strain rates $5x10^{-4}$ s^{-1} and $1x10^{-4}$ s^{-1} at different temperatures (300, 350, 400 and 450°C) is shown.

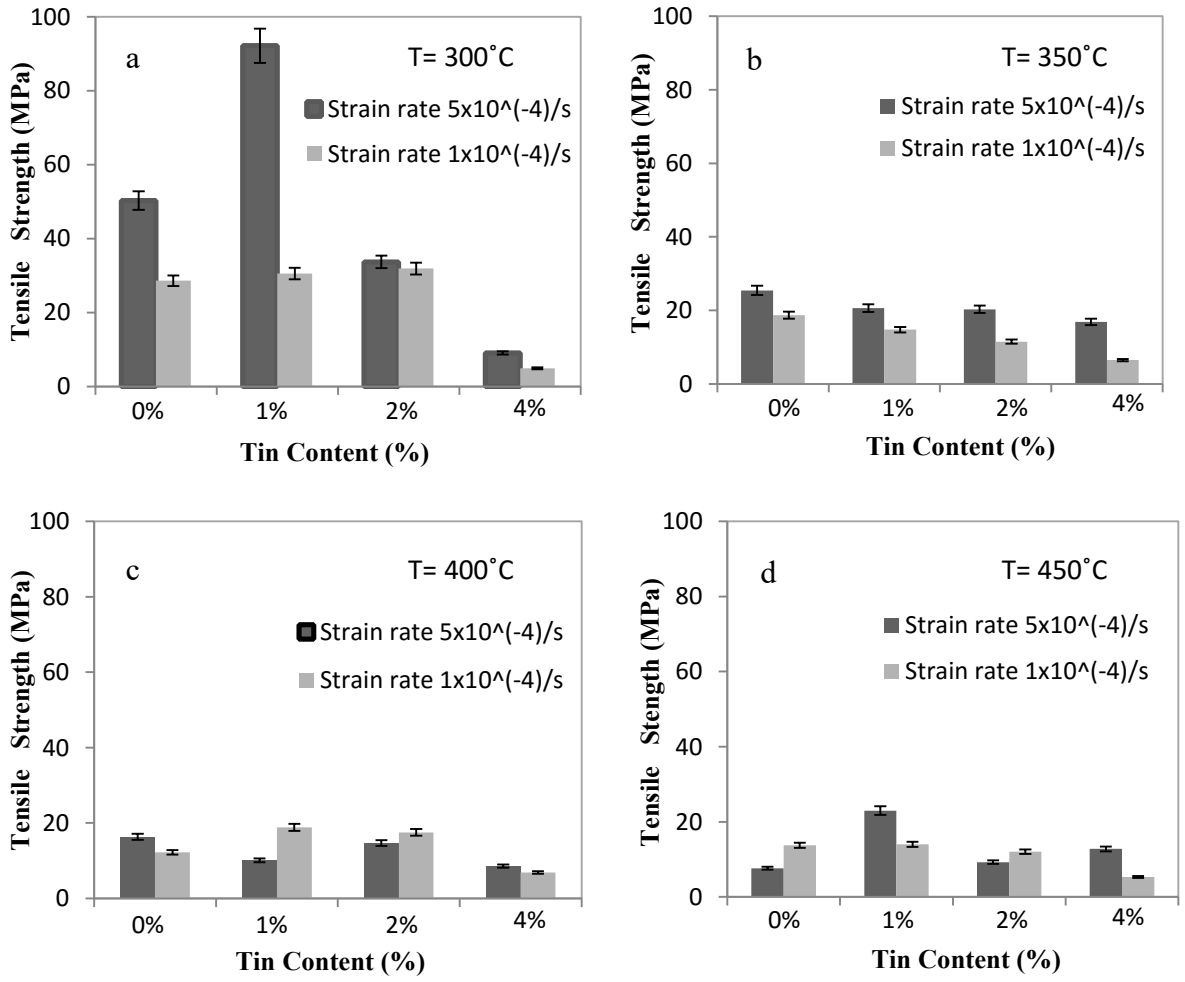

Figure 4.12: Tensile Strength variation with Tin content(%) at strain rate $5x10^{-4}$ s^{-1} and $1x10^{-4}$ s^{-1} at temperature (a) 300°C, (b) 350°C, (c) 400°C and (d) 450°C

Strain rate $5x10^{-4}$ s^{-1} shows higher tensile strength than strain rate $1x10^{-4}$ s^{-1}. Because at

slower strain rate ($1x10^{-4}$ s^{-1}), more grain growth takes place (as discussed later) and this large grain gives lower strength value owing to Hall-Petch relationship. At 300°C, with increasing Sn content (%), tensile strength increased and then with high Sn content tensile strength decreased [Figure 4.12(a)]. This is because high amount of Sn content formed very high amount of intermetallic particles. These particles degraded tensile strength. At 350°C [Figure 4.12(b)], tensile strength decreased than 300°C. This is attributed to with increasing temperature, strength values decreasing. For 400 and 450°C, tensile strength becomes more lower. At high temperature, oxide formation happens with high amount of alloying elements. Thus, at high temperature, 2% and 4% Sn containing alloy gives lower values [Figures 4.12(c) and 4.12(d)].

In Figure 4.13, elongation to failure variation with tin content at strain rates $5x10^{-4}$ s^{-1} and $1x10^{-4}$ s^{-1} at different temperatures (300, 350, 400 and 450°C) is shown.

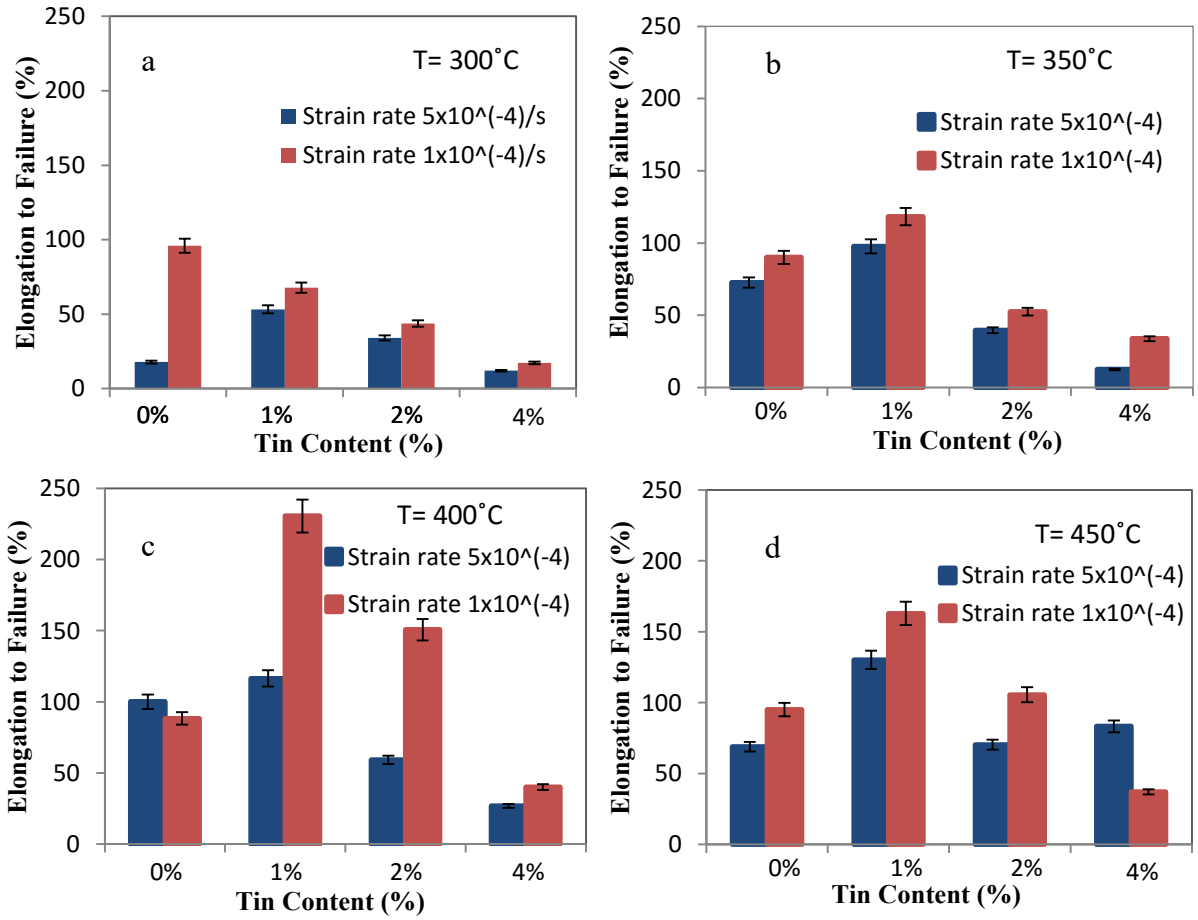

Figure 4.13: Elongation to failure(%) variation with Tin content(%) at strain rate $5x10^{-4}$ s^{-1} and $1x10^{-4}$ s^{-1} at temperature (a) 300°C, (b) 350°C, (c) 400°C and (d) 450°C

Strain rate $5x10^{-4}$ s^{-1} shows lower elongation to failure than strain rate $1x10^{-4}$ s^{-1}. Because at slower strain rate ($1x10^{-4}$ s^{-1}), grain growth takes place and this can retard the onset of neck formation. In this time, material can elongate more to failure. At 300°C [Figure 4.13(a)] and 350°C [Figure 4.13(b)], with increasing Sn content (%), elongation to failure increased and then with high Sn content elongation to failure decreased. This is because high amount of intermetallic particles degraded the elongation to failure. At 350°C, elongation to failure increased than 300°C. This is because with increasing temperature, material becomes soft and it showed higher elongation to failure. At 400°C, elongation to failure increased more [Figure 4.13(c)]. At 450°C, elongation to failure decreased slightly because of oxide formation [Figure 4.13(d)].

At strain rate $5x10^{-4}$ s^{-1}, tensile strength is higher, and elongation to failure is lower than strain rate $1x10^{-4}$ s^{-1}, because of higher grain growth at lower strain rate $1x10^{-4}$ s^{-1}. With increasing temperature, tensile strength decreased, and elongation to failure increased, for both strain rates.

4.6 Dynamic Grain Growth (DGG) Analysis

For dynamic grain growth analysis, microstructures are taken at six different positions of tensile tested samples, as shown in Figure 3.3.

4.6.1. Dynamic Grain Growth (DGG) Analysis at Strain Rate $5x10^{-4}$ s^{-1}

For Mg-1Ca alloy, after tensile test at strain rate $5x10^{-4}$ s^{-1} and at 300°C, microstructure of six positions are shown in Figure 4.14. In this figure, ‘a’ is in the static zone. In this zone, grain growth happens before tensile test due to placing the samples in high temperatures. At ‘a’ point, average grain size is 20.17 µm. Position of ‘b’, ‘c’, ‘d’, ‘e’ and ‘f’ are in the deformed zone. At ‘b’ point, grain size is 25.81 µm. At ‘c’ point, grain size is 35.07 µm. Grain size at ‘c’ point increases than ‘b’ point because of stretching or loading. At ‘d’ point, grain size is increased more and found 55.18 µm. But at ‘e’ point grain size is decreased and become 46.9 µm and at ‘f’ point grain size is 50.12 µm. The point where sample faced maximum load and necking happened at that point. Because of breaking at that point failure occurred. Point ‘e’ and ‘f’ are just beside the fracture point, so grain also broke at these points

due to very higher load. Thus maximum grain size is found before certain distance of fractured point.

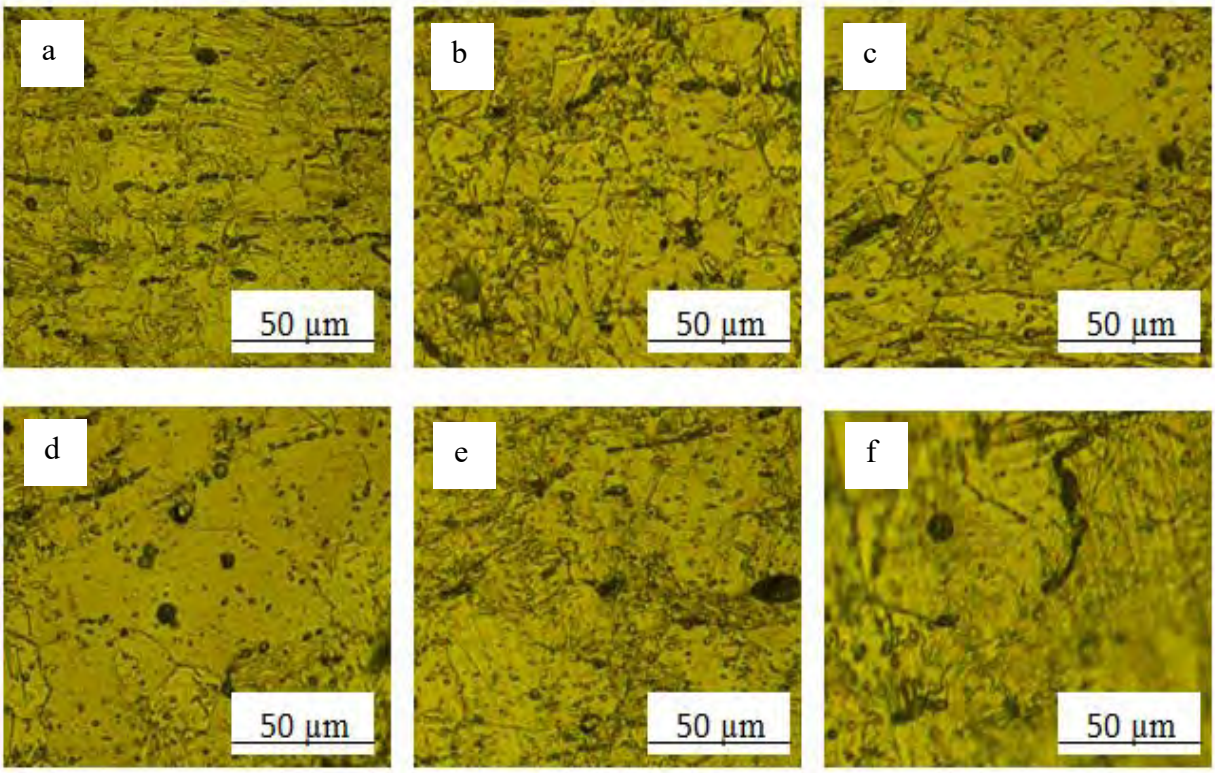

Figure 4.14: Optical microstructure of Mg-1Ca alloy at strain rate $5x10^{-4}$ s^{-1} at 300°C (a) Static zone and (b), (c), (d), (e), (f) deformed Zone

In Figure 4.15, after tensile test at strain rate $5x10^{-4}$ s^{-1} and at 350°C, microstructure of six positions of Mg-1Ca alloy are shown. At 'a' point, average grain size is 25.75 µm. Static grain size increased at 350°C than 300°C. It is due to at higher temperature grain growth happens. At points 'b', 'c', 'd', 'e' and 'f', grain size are found 27.12 µm, 30.17 µm, 36.45 µm, 50.72 µm and 35.57 µm, respectively.

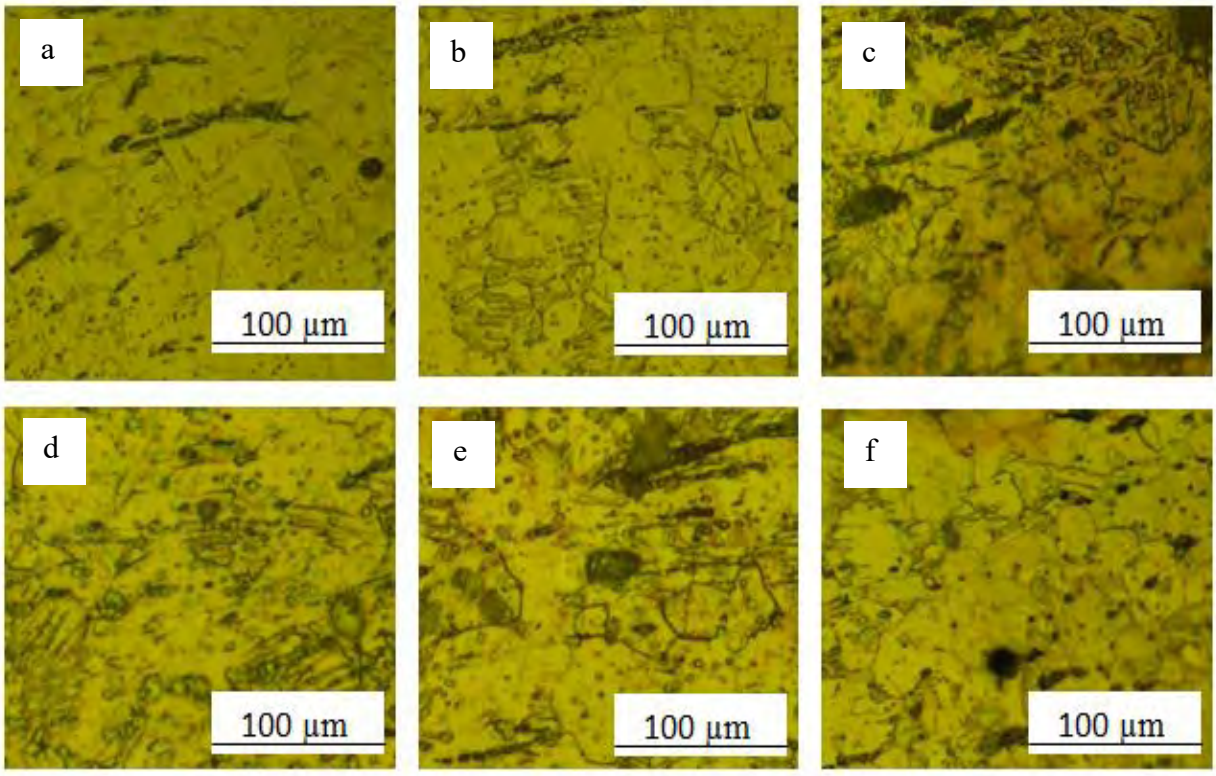

Figure 4.15: Optical microstructure of Mg-1Ca alloy at strain rate $5x10^{-4}$ s^{-1} 350°C (a) Static zone and (b), (c), (d), (e), (f) deformed Zone

In Figure 4.16, after tensile test at strain rate $5x10^{-4}$ s^{-1} and at 400°C, microstructure of six positions of Mg-1Ca alloy are shown. At 'a' point, average grain size is 43.35 µm. At points 'b', 'c', 'd', 'e' and 'f', grain size are found 45.07 µm, 61.93 µm, 75.15 µm, 65.92 µm and 52.73 µm, respectively. Maximum grain size is found to be 75.15 µm. Due to high temperature, grain size increased in both static and deformed zone.

In Figure 4.17, after tensile test at strain rate $5x10^{-4}$ s^{-1} and at 450°C, microstructure of six positions of Mg-1Ca alloy are shown. At 'a' point, average grain size is 91.93 µm. At points 'b', 'c', 'd', 'e' and 'f', grain size are 107.75 µm, 122.52 µm, 135.88 µm, 153.81 µm and 204.98 µm, respectively. Maximum grain size is 204.98 µm.

With increasing temperature, both static and dynamic grain growth increased for Mg-1Ca alloy at strain rate $5x10^{-4}$ s^{-1}.

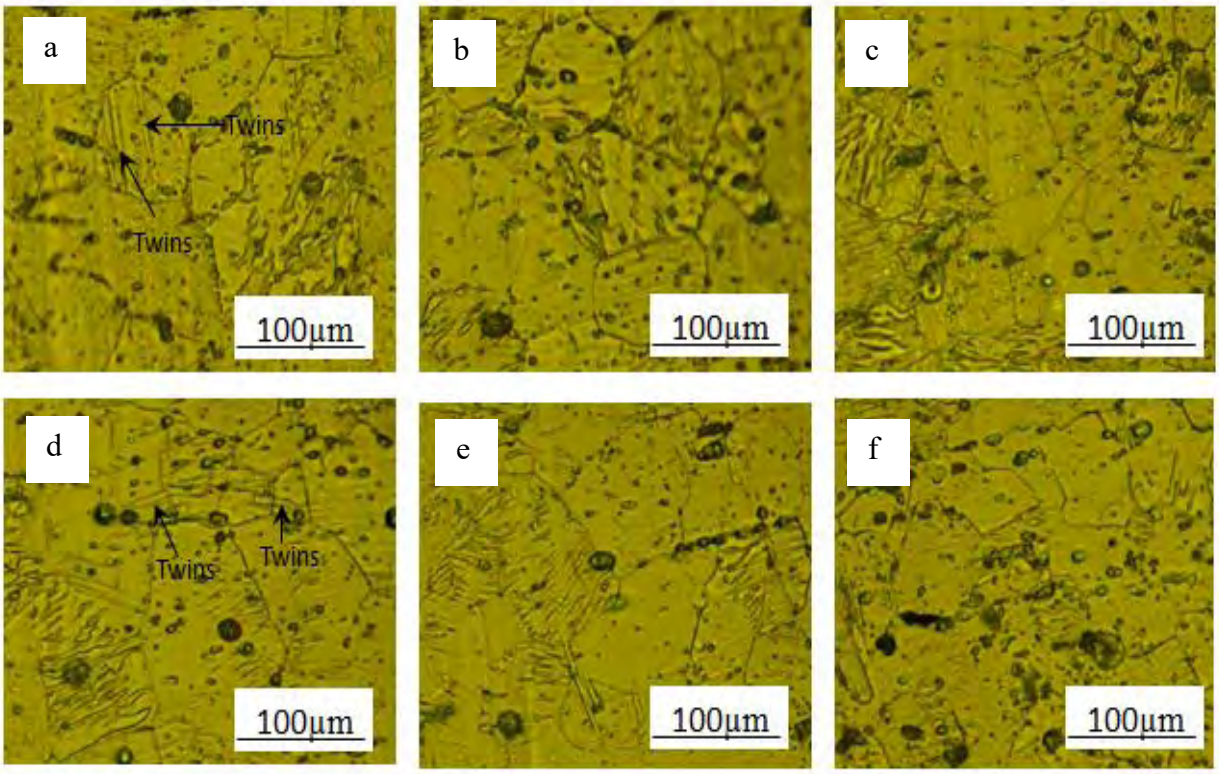

Figure 4.16: Optical microstructure of Mg-1Ca alloy at strain rate $5x10^{-4}$ s^{-1} 400°C (a) Static zone and (b), (c), (d), (e), (f) deformed Zone

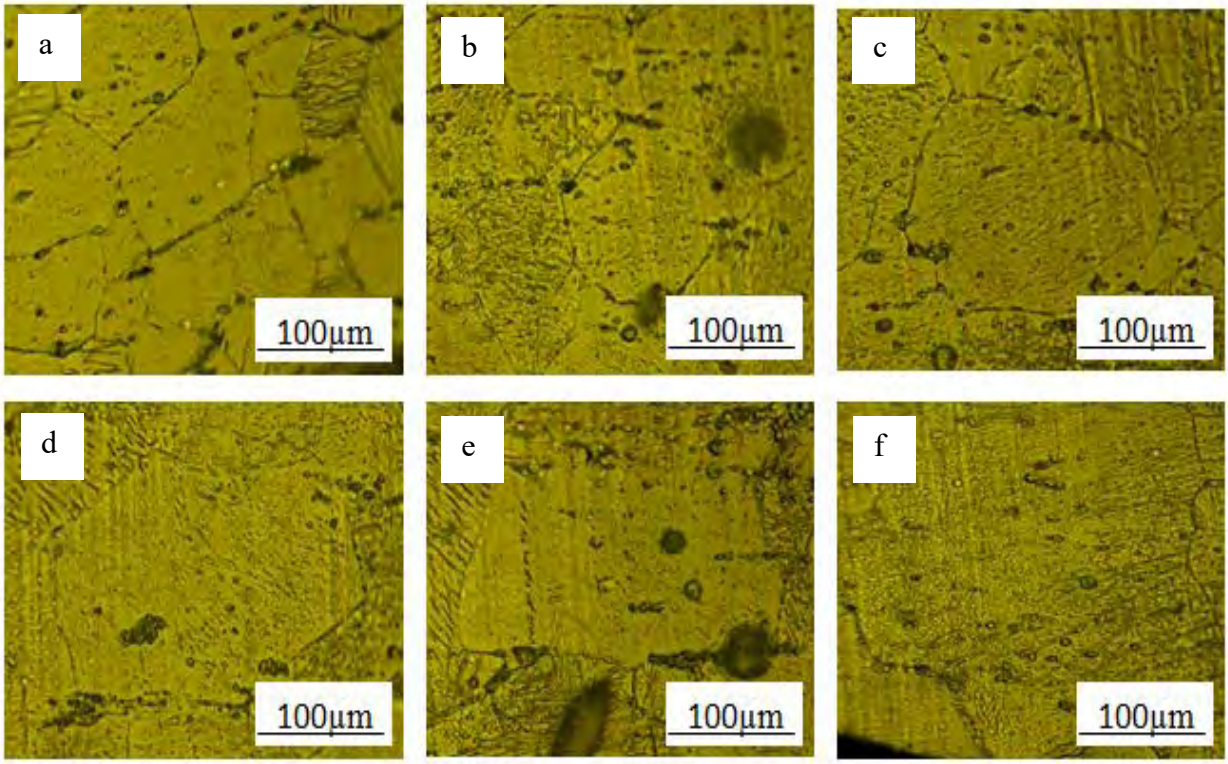

Figure 4.17: Optical microstructure of Mg-1Ca alloy at strain rate $5x10^{-4}$ s^{-1} 450°C (a) Static zone and (b), (c), (d), (e), (f) deformed Zone

For Mg-1Ca-1Sn alloy, after tensile test at strain rate $5x10^{-4}$ s^{-1} and at 300°C, microstructure of six positions are shown in Figure 4.18. At 'a' point, average grain size is 13.18 µm. Due to addition of 1% Sn, grain size decreased in this alloy than Mg-1Ca alloy. At points 'b', 'c', 'd', 'e' and 'f', grain size are 17.58 µm, 22.21 µm, 25.49 µm, 33.39 µm and 39.55 µm, respectively. Maximum grain size is 39.55 µm.

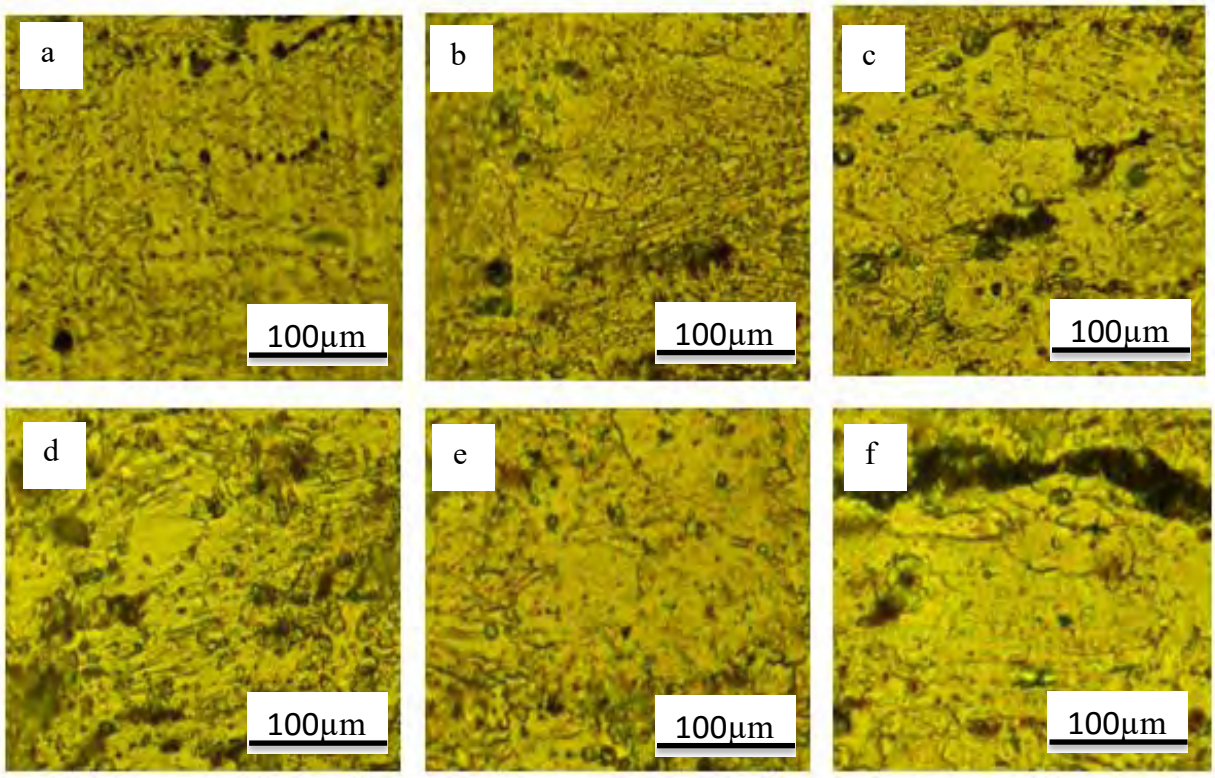

Figure 4.18: Optical microstructure of Mg-1Ca-1Sn alloy at strain rate $5x10^{-4}$ s^{-1} at 300°C (a) Static zone and (b), (c), (d), (e), (f) deformed Zone

For Mg-1Ca-1Sn alloy, after tensile test at strain rate $5x10^{-4}$ s^{-1} and at 350°C, microstructure of six positions are shown in Figure 4.19. At 'a' point, average grain size is 18.46 µm. Due to increase in temperature (350°C), grain size increased than Mg-1Ca-1Sn alloy at 300°C. At points 'b', 'c', 'd', 'e' and 'f', grain size are 22.85 µm, 29.88 µm, 33.41 µm, 43.51 µm and 51.25 µm, respectively. Maximum grain size is 51.25 µm.

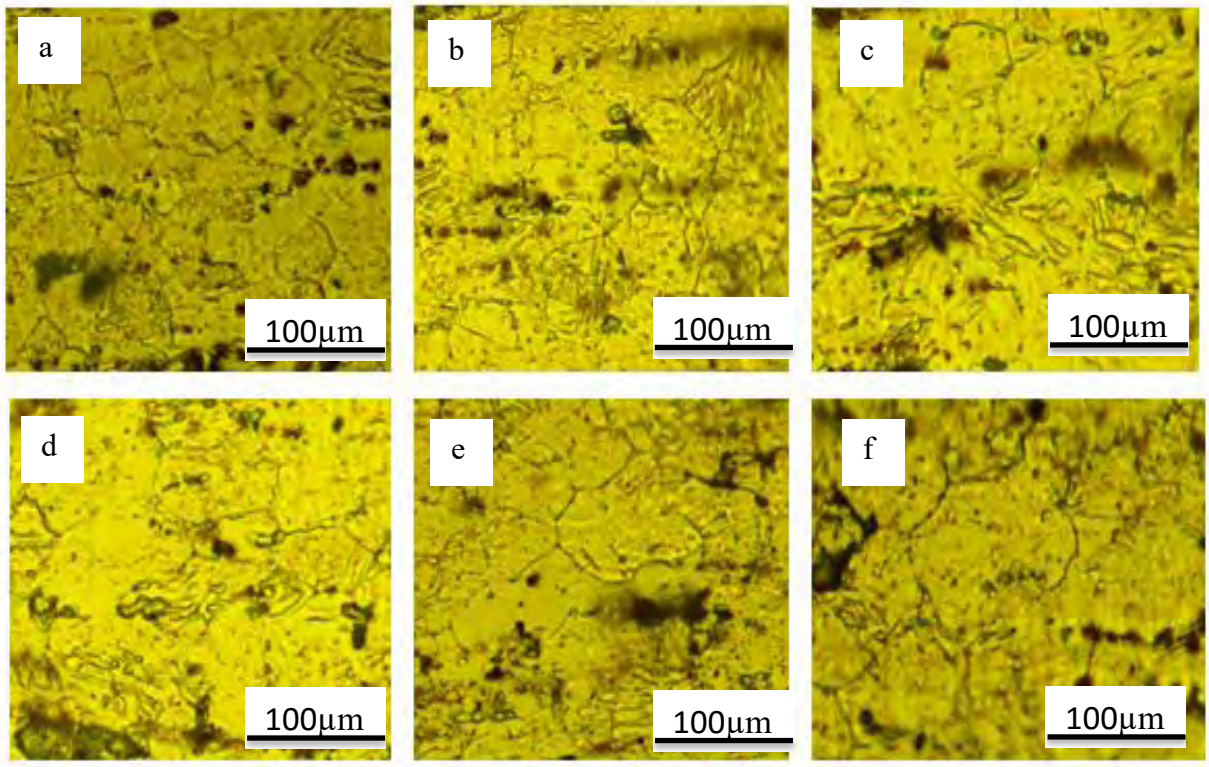

Figure 4.19: Optical microstructure of Mg-1Ca-1Sn alloy at strain rate $5x10^{-4}$ s^{-1} at 350°C (a) Static zone and (b), (c), (d), (e), (f) deformed Zone

For Mg-1Ca-1Sn alloy, after tensile test at strain rate $5x10^{-4}$ s^{-1} and at 400°C, microstructure of six positions are shown in Figure 4.20. At 'a' point, average grain size is 29.36 µm. At points 'b', 'c', 'd', 'e' and 'f', grain size are 50.10 µm, 52.77 µm, 54.12 µm, 56.37 µm and 61.52 µm, respectively. Maximum grain size is 61.52 µm. Grain size increased more in this alloy at 400°C than at 350°C of this alloy.

For Mg-1Ca-1Sn alloy, after tensile test at strain rate $5x10^{-4}$ s^{-1} and at 450°C, microstructure of six positions are shown in Figure 4.21. At 'a' point, average grain size is 35.16 µm. At points 'b', 'c', 'd', 'e' and 'f', grain size are 50.10 µm, 44.47 µm, 47.99 µm, 58.36 µm and 50.98 µm, respectively. Maximum grain size is 58.36 µm.

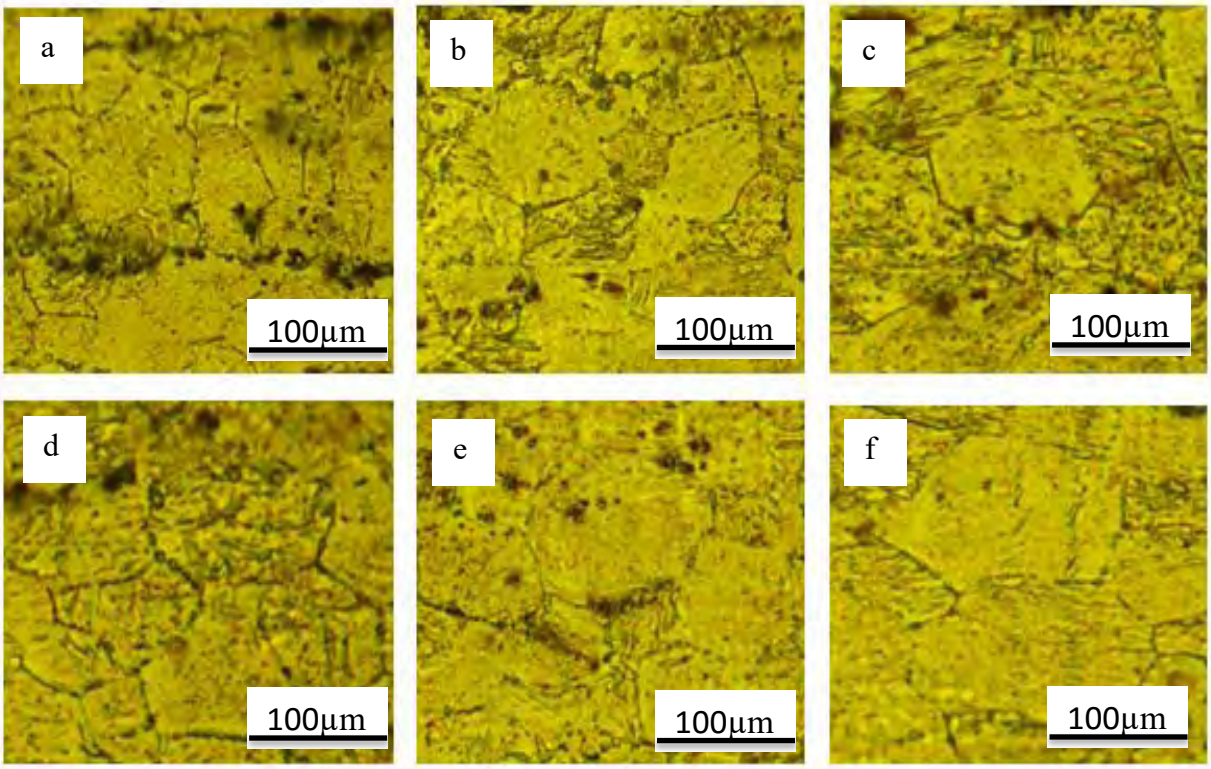

Figure 4.20: Optical microstructure of Mg-1Ca-1Sn alloy at strain rate $5x10^{-4}$ s^{-1} at 400°C (a) Static zone and (b), (c), (d), (e), (f) deformed Zone

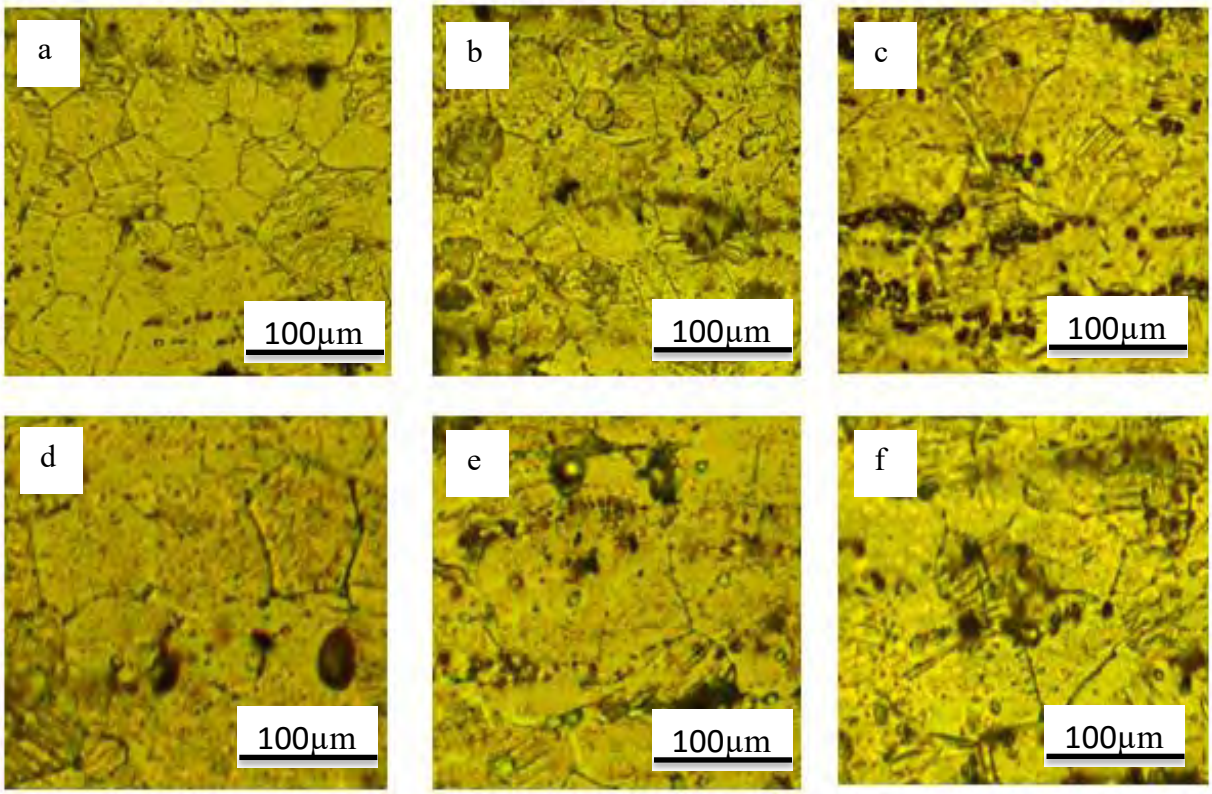

Figure 4.21: Optical microstructure of Mg-1Ca-1Sn alloy at strain rate $5x10^{-4}$ s^{-1} at 450°C (a) Static zone and (b), (c), (d), (e), (f) deformed Zone

For Mg-1Ca-2Sn alloy, after tensile test at strain rate $5x10^{-4}$ s^{-1} and at 300°C, microstructure of six positions are shown in Figure 4.22. At 'a' point, average grain size is 17.69 µm. At points 'b', 'c', 'd', 'e' and 'f', grain size are 33.40 µm, 75.59 µm, 36.04 µm, 31.29 µm and 29.53 µm, respectively. Maximum grain size is 75.59 µm.

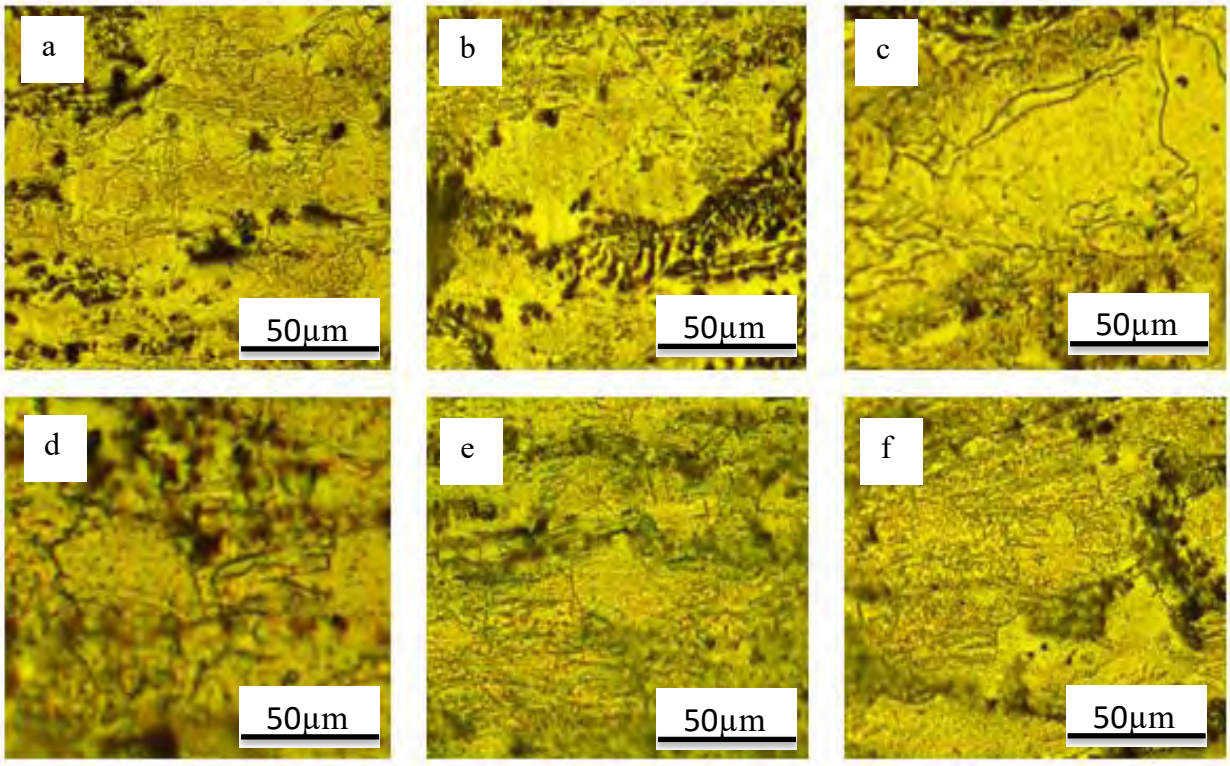

Figure 4.22: Optical microstructure of Mg-1Ca-2Sn alloy at strain rate $5x10^{-4}$ s^{-1} at 300°C (a) Static zone and (b), (c), (d), (e), (f) deformed Zone

For Mg-1Ca-2Sn alloy, after tensile test at strain rate $5x10^{-4}$ s^{-1} and at 350°C, microstructure of six positions are shown in Figure 4.23. At 'a' point, average grain size is 28.14 µm. Due to increase in temperature (350°C), grain size increased than Mg-1Ca-2Sn alloy at 300°C. At points 'b', 'c', 'd', 'e' and 'f', grain size are 30.29 µm, 35.16 µm, 40.89 µm, 45.20 µm and 30.23 µm, respectively. Maximum grain size is 45.20 µm.

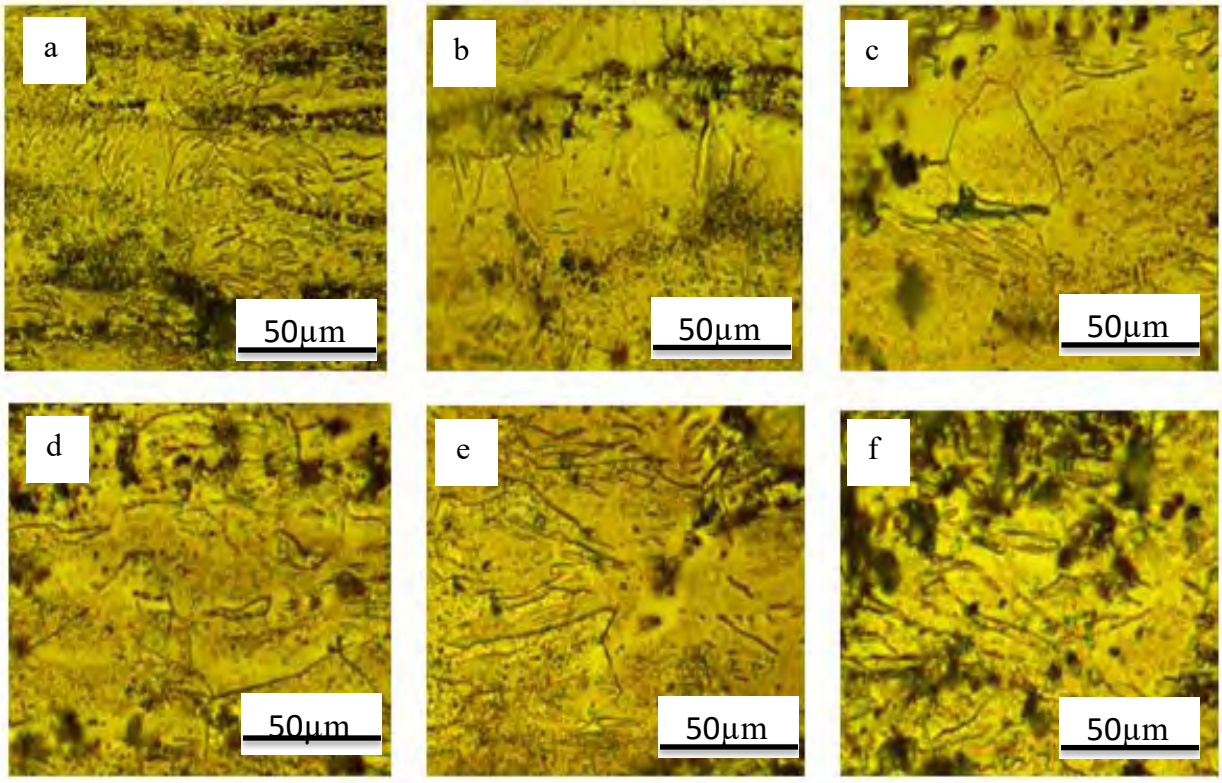

Figure 4.23: Optical microstructure of Mg-1Ca-2Sn alloy at strain rate $5x10^{-4}$ s^{-1} at 350°C (a) Static zone and (b), (c), (d), (e), (f) deformed Zone

For Mg-1Ca-2Sn alloy, after tensile test at strain rate $5x10^{-4}$ s^{-1} and at 400°C, microstructure of six positions are shown in Figure 4.24. At 'a' point, average grain size is 33.56 µm. At points 'b', 'c', 'd', 'e' and 'f', grain size are 35.32 µm, 38.40 µm, 41.84 µm, 53.95µm and 75.59 µm, respectively. Maximum grain size is 75.59 µm. Grain size increased more in this alloy at 400°C than at 350°C of this alloy.

For Mg-1Ca-2Sn alloy, after tensile test at strain rate $5x10^{-4}$ s^{-1} and at 450°C, microstructure of six positions are shown in Figure 4.25. At 'a' point, average grain size is 42.54 µm. At points 'b', 'c', 'd', 'e' and 'f', grain size are 48.18 µm, 55.64 µm, 60.12 µm, 74.18 µm and 85.25 µm, respectively. Maximum grain size is 85.25 µm. Due to high temperature grain size increased more at 450°C than at 400°C of this alloy.

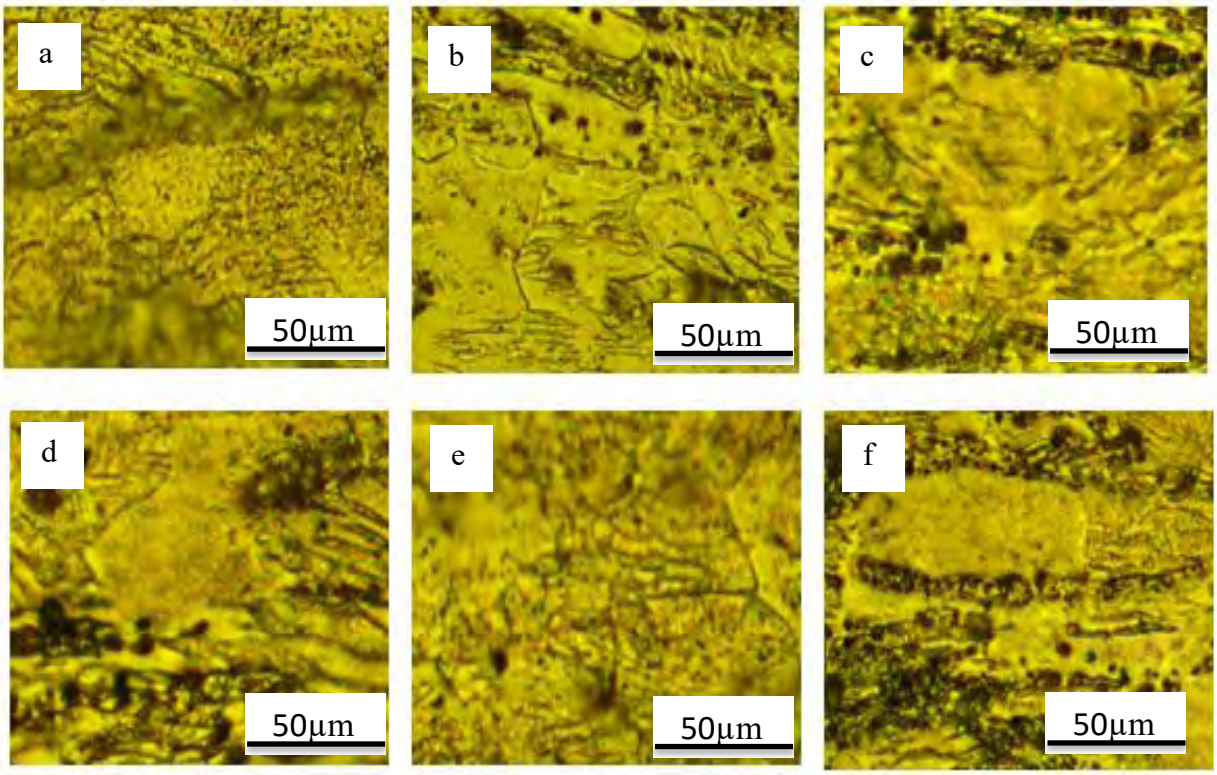

Figure 4.24: Optical microstructure of Mg-1Ca-2Sn alloy at strain rate $5x10^{-4}$ s^{-1} at 400°C (a) Static zone and (b), (c), (d), (e), (f) deformed Zone

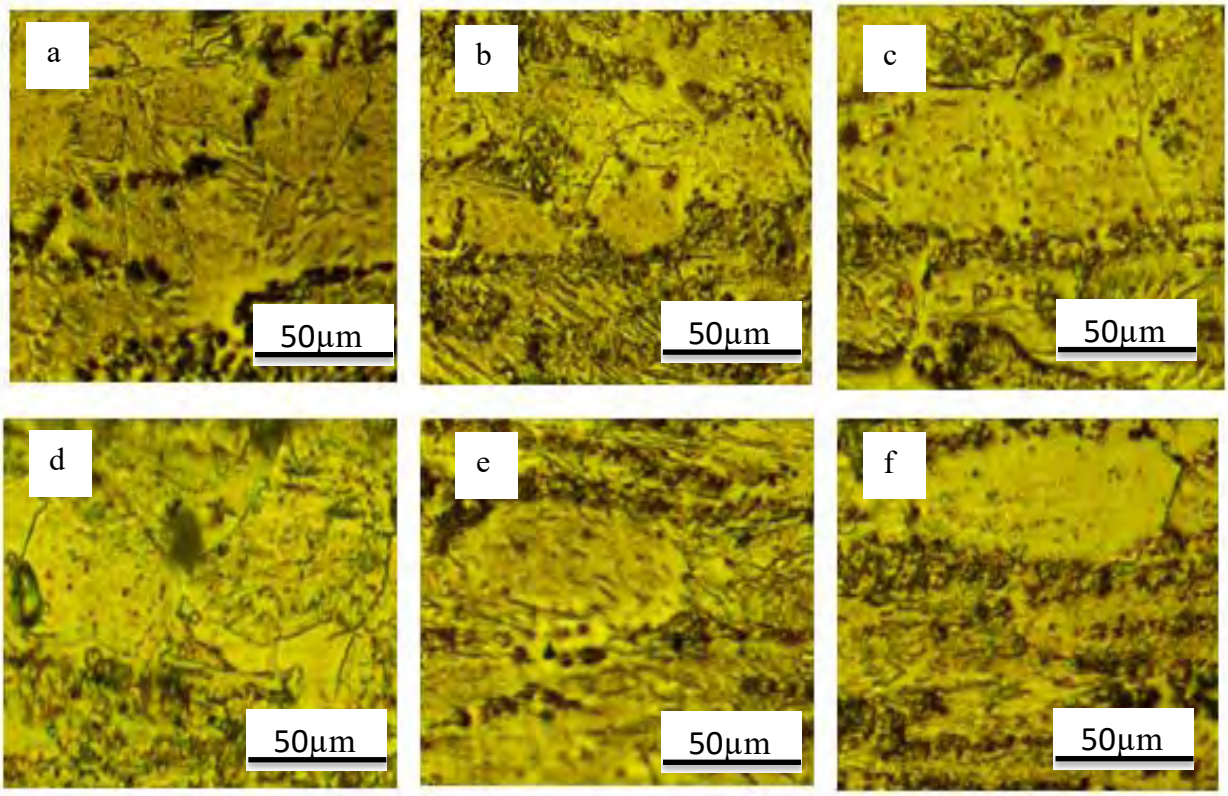

Figure 4.25: Optical microstructure of Mg-1Ca-2Sn alloy at strain rate $5x10^{-4}$ s^{-1} at 450°C (a) Static zone and (b), (c), (d), (e), (f) deformed Zone

For Mg-1Ca-4Sn alloy, after tensile test at strain rate $5x10^{-4}$ s^{-1} and at 300°C, microstructure of six positions are shown in Figure 4.26. At 'a' point, average grain size is 10.9 µm. Due to addition of 4% Sn, grain size decreased in this alloy than Mg-1Ca-2Sn alloy. At points 'b', 'c', 'd', 'e' and 'f', grain size are 12.3 µm, 17.58 µm, 31.99 µm, 42.54 µm and 45.18 µm, respectively. Maximum grain size is 45.18 µm.

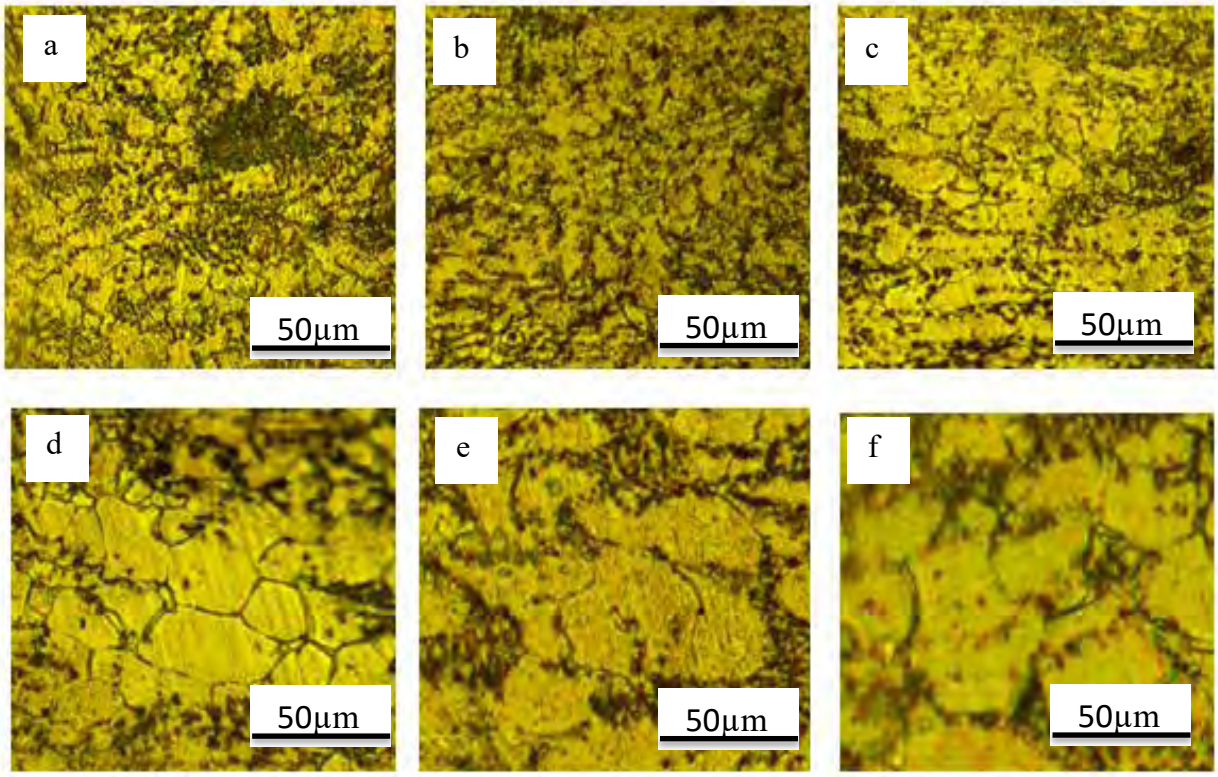

Figure 4.26: Optical microstructure of Mg-1Ca-4Sn alloy at strain rate $5x10^{-4}$ s^{-1} at 300°C (a) Static zone and (b), (c), (d), (e), (f) deformed Zone

For Mg-1Ca-4Sn alloy, after tensile test at strain rate $5x10^{-4}$ s^{-1} and at 350°C, microstructure of six positions are shown in Figure 4.27. At 'a' point, average grain size is 15.47 µm. At points 'b', 'c', 'd', 'e' and 'f', grain size are 29.53 µm, 31.29 µm, 40.18 µm, 69.43 µm and 16.35 µm, respectively. Maximum grain size is 69.43 µm. Due to increase in temperature (350°C), grain size increased than at 300°C in this alloy.

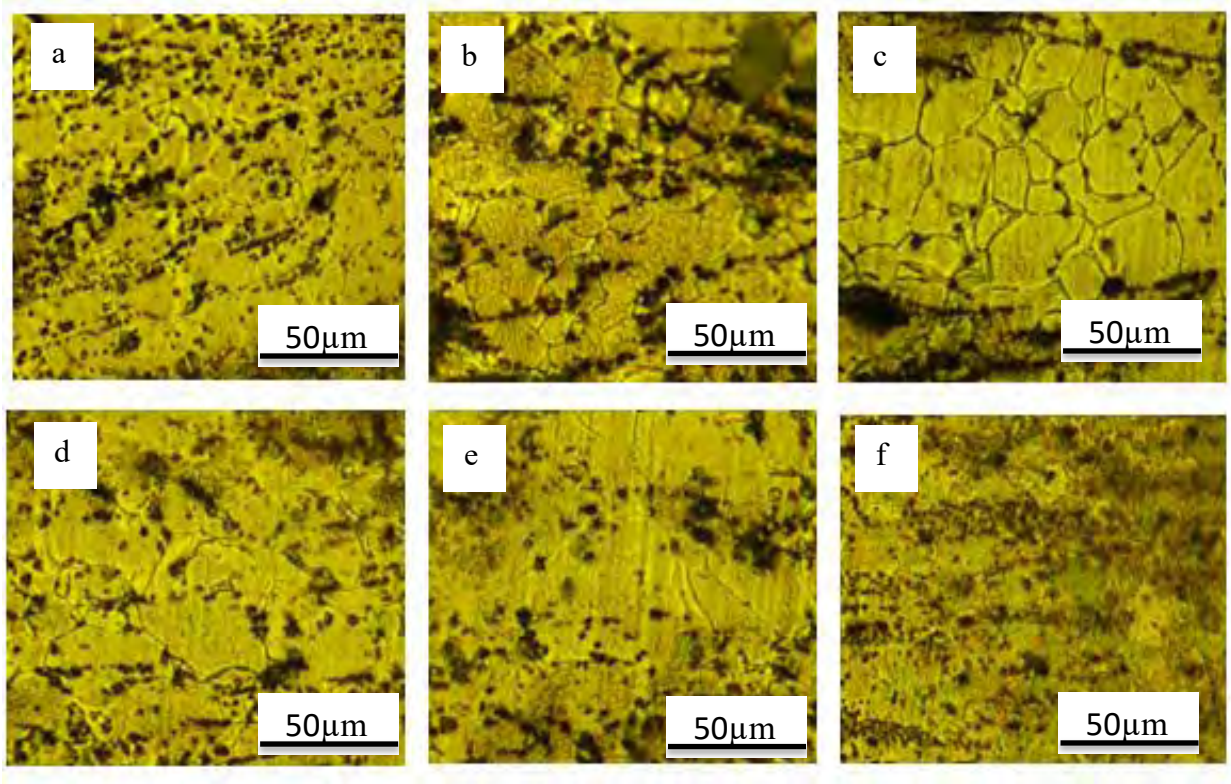

Figure 4.27: Optical microstructure of Mg-1Ca-4Sn alloy at strain rate $5x10^{-4}$ s^{-1} at 350°C (a) Static zone and (b), (c), (d), (e), (f) deformed Zone

For Mg-1Ca-4Sn alloy, after tensile test at strain rate $5x10^{-4}$ s^{-1} and at 400°C, microstructure of six positions are shown in Figure 4.28. At 'a' point, average grain size is 25.15 µm. At points 'b', 'c', 'd', 'e' and 'f', grain size are 30.96 µm, 43.61 µm, 55.71 µm, 96.23 µm and 28.52 µm, respectively. Maximum grain size is 96.23 µm. Grain size increased more in this alloy at 400°C than at 350°C of this alloy.

For Mg-1Ca-4Sn alloy, after tensile test at strain rate $5x10^{-4}$ s^{-1} and at 450°C, microstructure of six positions are shown in Figure 4.29. At 'a' point, average grain size is 57.68 µm. At points 'b', 'c', 'd', 'e' and 'f', grain size are 67.13 µm, 84.02 µm, 135.35 µm, 149.41 µm and 99.84 µm, respectively. Maximum grain size is 149.41 µm.

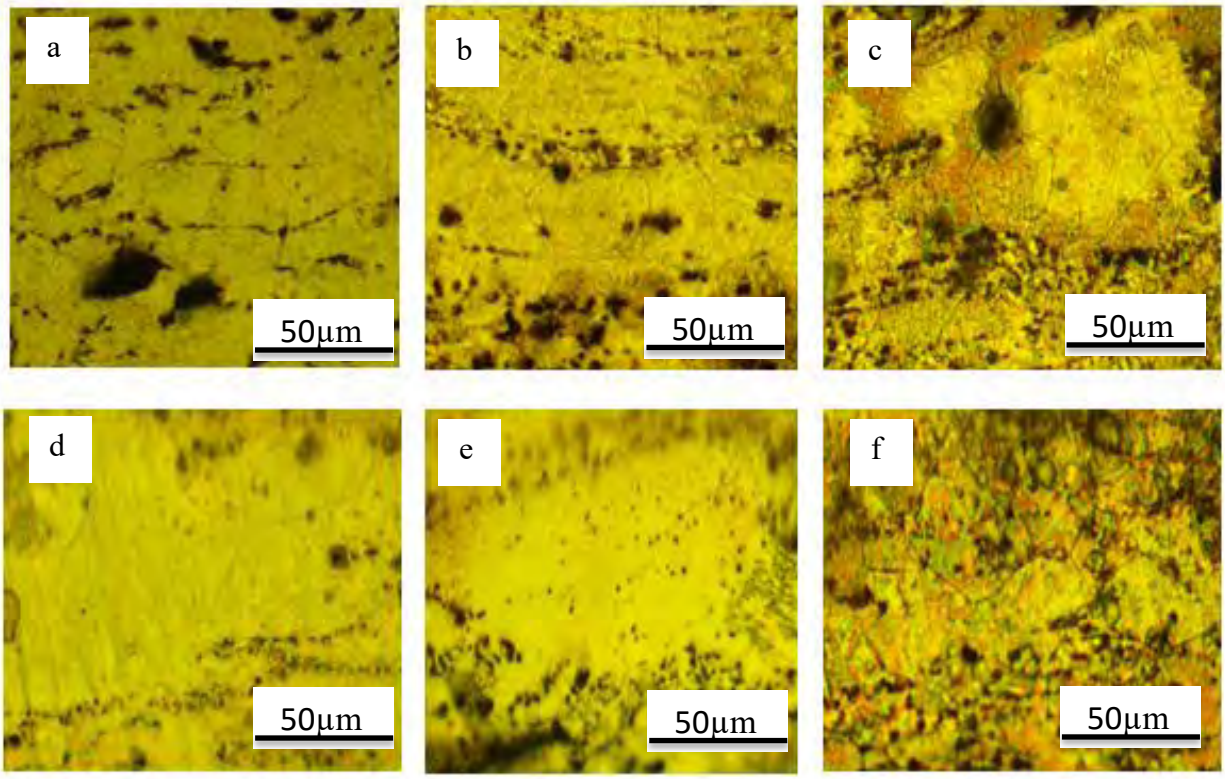

Figure 4.28: Optical microstructure of Mg-1Ca-4Sn alloy at strain rate $5x10^{-4}$ s^{-1} at 400°C (a) Static zone and (b), (c), (d), (e), (f) deformed Zone

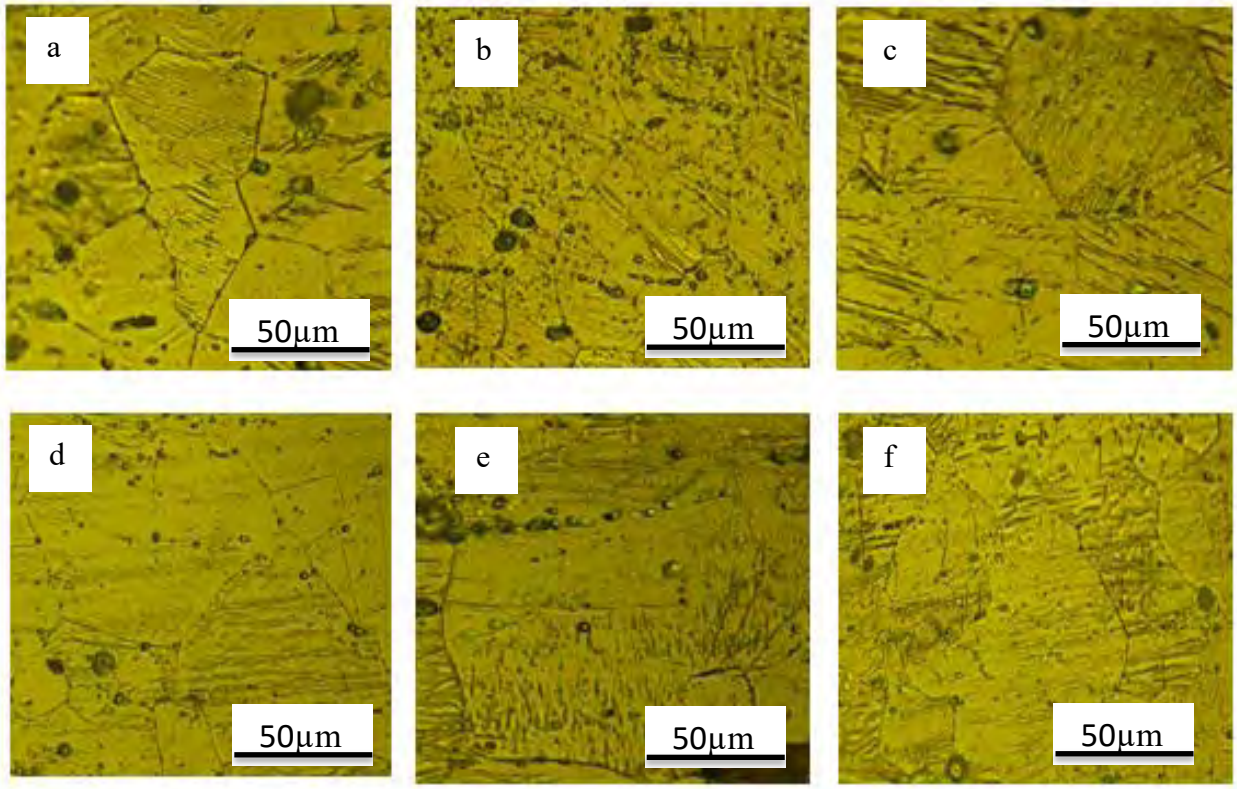

Figure 4.29: Optical microstructure of Mg-1Ca-4Sn alloy at strain rate $5x10^{-4}$ s^{-1} at 450°C (a) Static zone and (b), (c), (d), (e), (f) deformed Zone

At strain rate 5x10^{-4} s^{-1}, grain growth in the gauge region is higher than that in the grip region for all alloys. Maximum grain size is before certain distance of fracture point. With increasing Sn content, grain size decreased in both grip and gauge regions. However, with increasing temperature, grain size increased in both regions. Thus, both static and dynamic grain growth increased for all alloys with increasing temperature.

4.6.2. Dynamic Grain Growth (DGG) Analysis at Strain Rate 1x10^{-4} s^{-1}

For Mg-1Ca alloy, after tensile test at strain rate 1x10^{-4} s^{-1} and at 300°C, microstructures of six positions are shown in Figure 4.30. At 'a' point, average grain size is 32.87 µm. At points 'b', 'c', 'd', 'e' and 'f', grain size are 34.63 µm, 38.18 µm, 45.67 µm, 48.34 µm and 64.16 µm, respectively. Maximum grain size is 64.16µm. Due to slower strain rate more grain growth happens. So, grain size is found larger than strain rate 5x10^{-4} s^{-1} in Mg-1Ca alloy at 300°C.

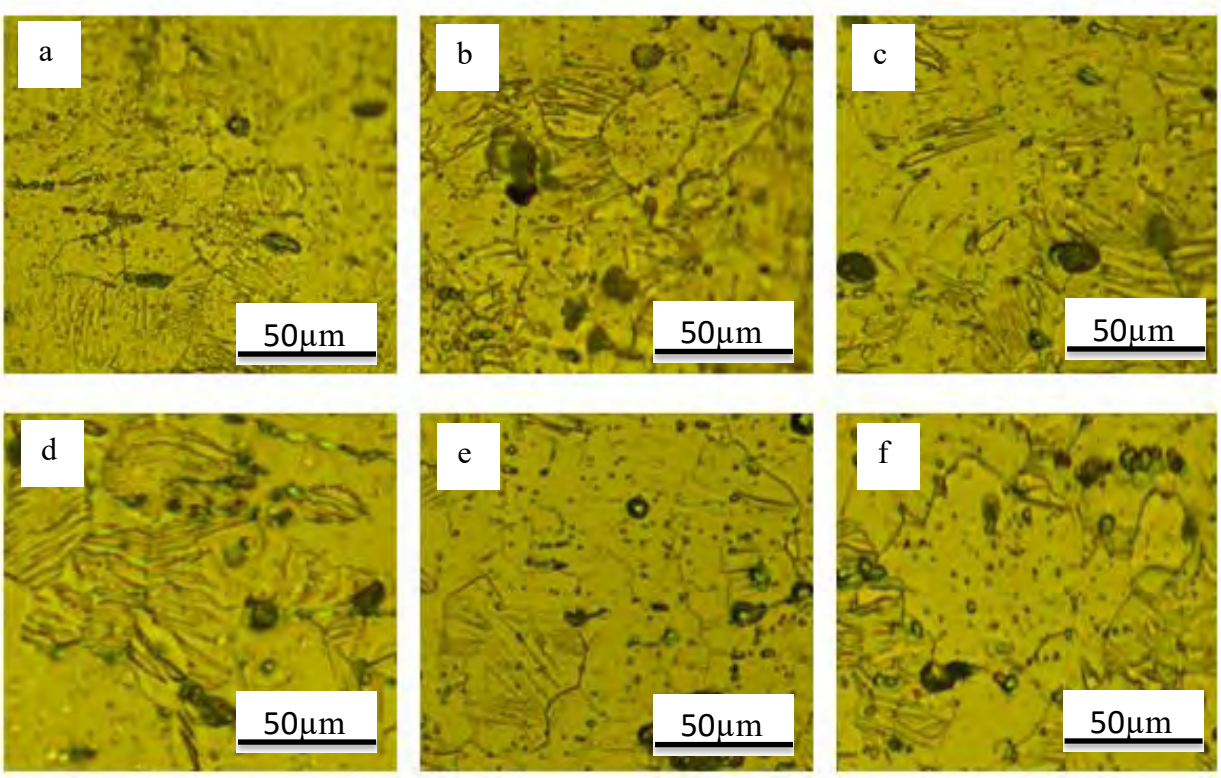

Figure 4.30: Optical microstructure of Mg-1Ca alloy at strain rate 1x10^{-4} s^{-1} at 300°C (a) Static zone and (b), (c), (d), (e), (f) deformed Zone

In Figure 4.31, after tensile test at strain rate $1x10^{-4}$ s^{-1} and at 350°C, microstructures of six positions of Mg-1Ca alloy are shown. At 'a' point, average grain size is 36.04µm. It is because grain growth happens at higher temperature. At points 'b', 'c', 'd', 'e' and 'f', grain size are 42.19 µm, 54.49 µm, 65.57 µm, 74.71 µm and 38.56 µm, respectively. Maximum Grain size is 74.71 µm.

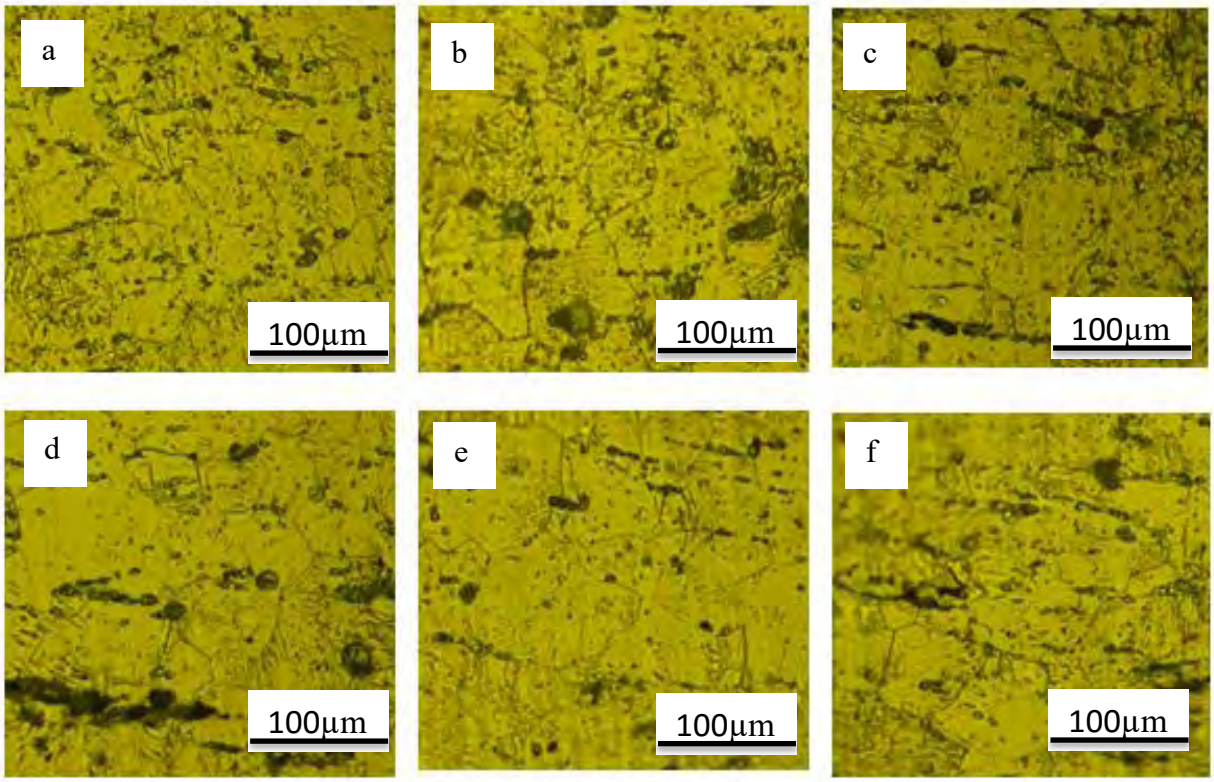

Figure 4.31: Optical microstructure of Mg-1Ca alloy at strain rate $1x10^{-4}$ s^{-1} 350°C (a) Static zone and (b), (c), (d), (e), (f) deformed Zone

In Figure 4.32, after tensile test at strain rate $1x10^{-4}$ s^{-1} and at 400°C, microstructures of six positions of Mg-1Ca alloy are shown. At 'a' point, average grain size is 51.63 µm. At points 'b', 'c', 'd', 'e' and 'f', grain size are 56.25 µm, 106.35 µm, 119.53 µm, 123.05 µm and 159.43 µm, respectively. Maximum grain size is 159.43 µm.

In Figure 4.33, after tensile test at strain rate $1x10^{-4}$ s^{-1} and at 450°C, microstructures of six positions of Mg-1Ca alloy are shown. At 'a' point, average grain size is 223.59 µm. At points 'b', 'c', 'd', 'e' and 'f', grain size are 289.16 µm, 341.89 µm, 351.56 µm, 322.67 µm and 288.28 µm, respectively. Maximum grain size is 351.56 µm.

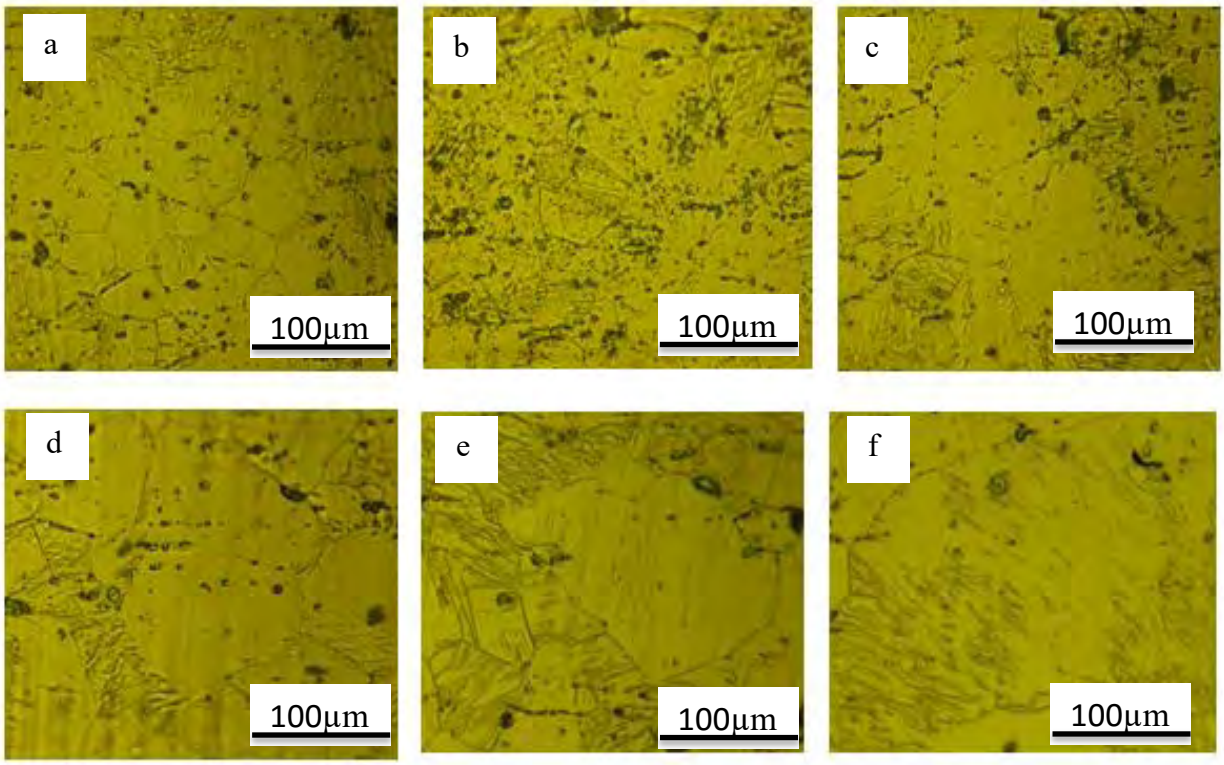

Figure 4.32: Optical microstructure of Mg-1Ca alloy at strain rate $1x10^{-4}$ s^{-1} 400°C (a) Static zone and (b), (c), (d), (e), (f) deformed Zone

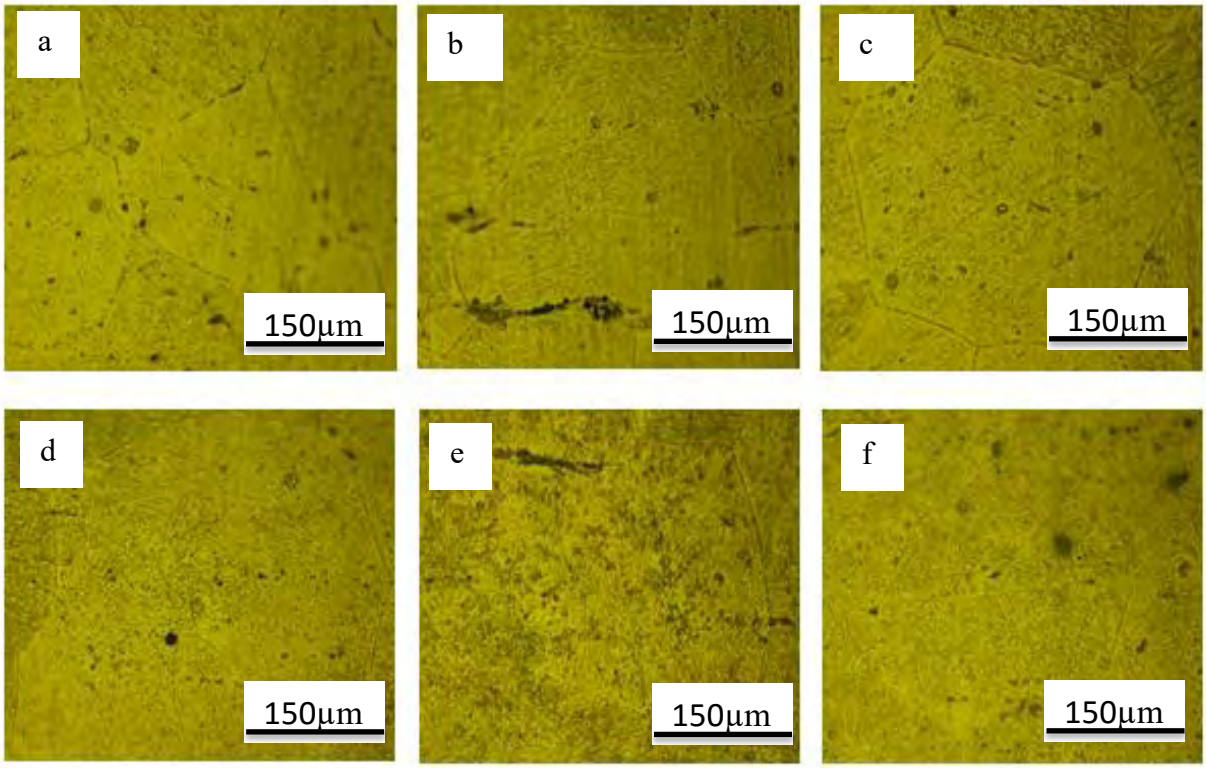

Figure 4.33: Optical microstructure of Mg-1Ca alloy at strain rate $1x10^{-4}$ s^{-1} 450°C (a) Static zone and (b), (c), (d), (e), (f) deformed Zone

With increasing temperature both static and dynamic grain growth increased for Mg-1Ca alloy at strain rate $1x10^{-4}$ s^{-1}.

For Mg-1Ca-1Sn alloy, after tensile test at strain rate $1x10^{-4}$ s^{-1} and at 300°C, microstructures of six positions are shown in Figure 4.34. At 'a' point, average grain size is 15.82 µm. Due to addition of 1% Sn, grain size decreased in this alloy than Mg-1Ca alloy. At points 'b', 'c', 'd', 'e' and 'f', grain size are 22.85 µm, 28.37 µm, 25.84 µm, 24.61 µm and 18.46 µm, respectively. Maximum grain size is 28.37 µm.

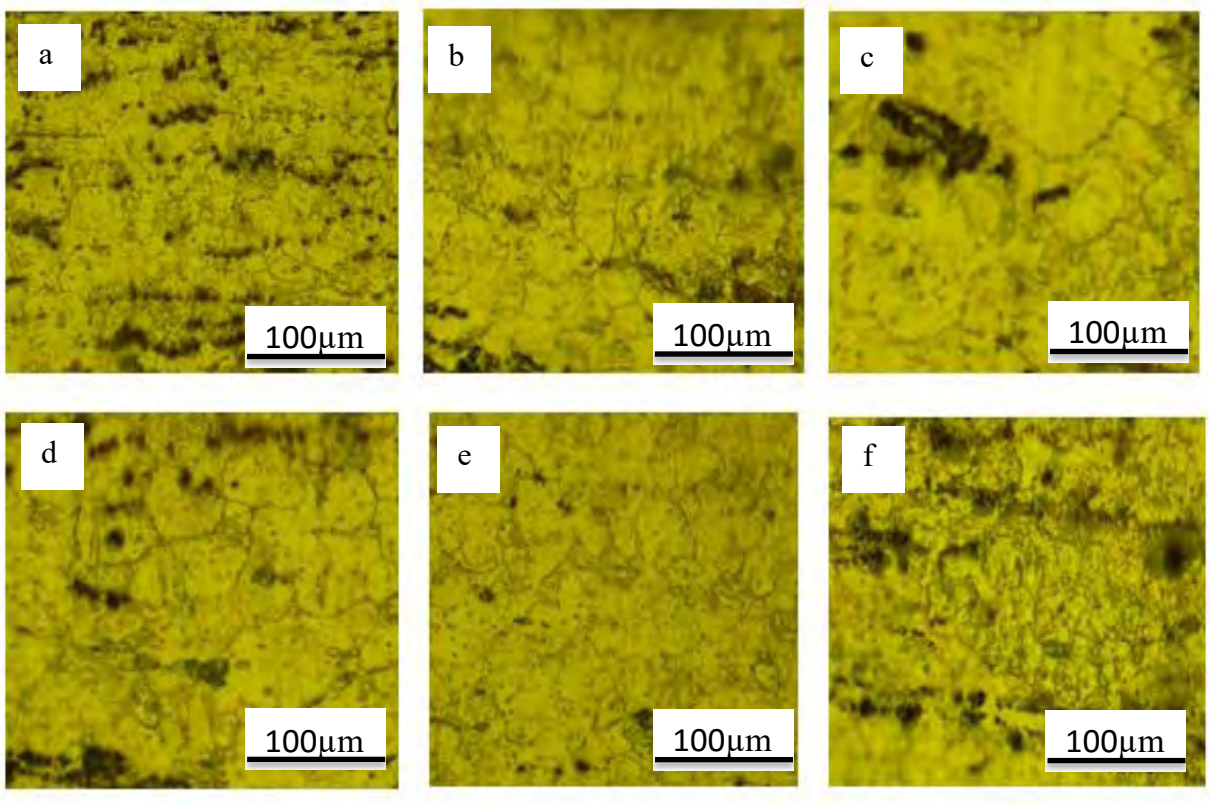

Figure 4.34: Optical microstructure of Mg-1Ca-1Sn alloy at strain rate $1x10^{-4}$ s^{-1} at 300°C (a) Static zone and (b), (c), (d), (e), (f) deformed Zone

For Mg-1Ca-1Sn alloy, after tensile test at strain rate $1x10^{-4}$ s^{-1} and at 350°C, microstructures of six positions are shown in Figure 4.35. At 'a' point, average grain size is 24.72 µm. At points 'b', 'c', 'd', 'e' and 'f', grain size are 37.27 µm, 46.93 µm, 56.25 µm, 76.99 µm and 65.81 µm, respectively. Maximum grain size is 76.99 µm.

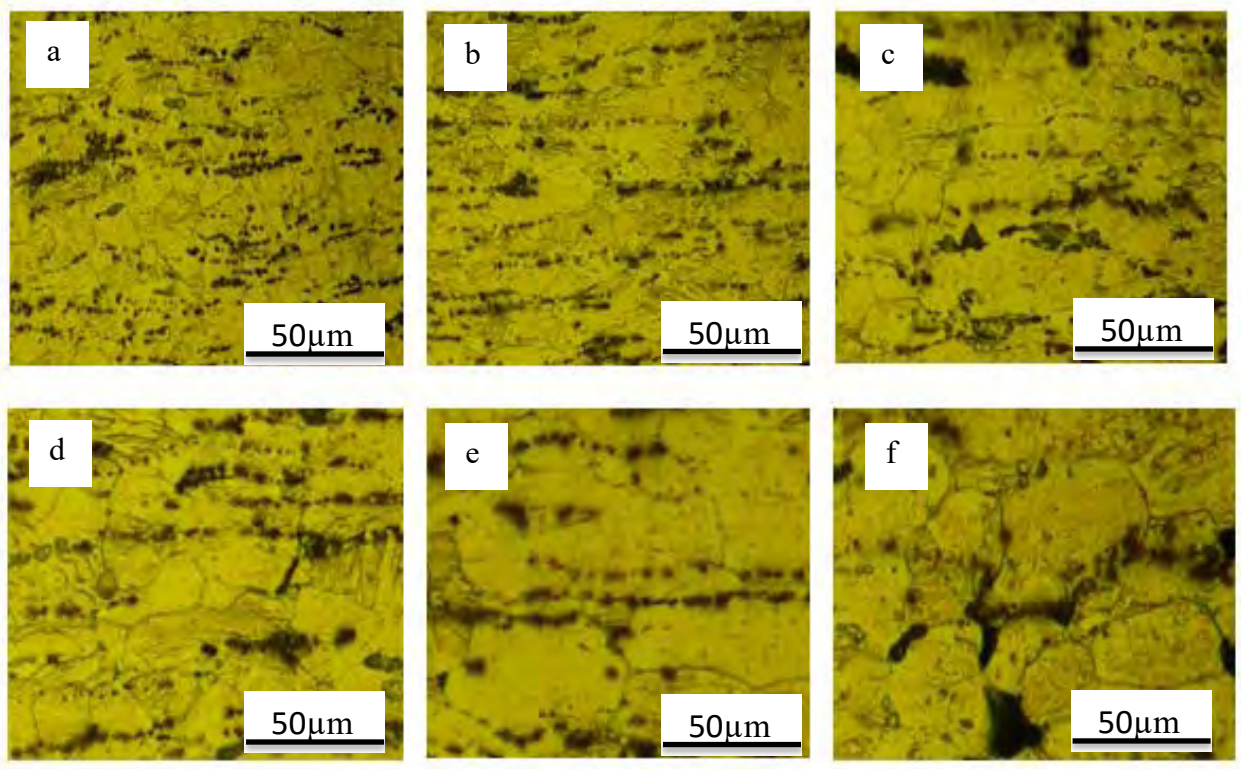

Figure 4.35: Optical microstructure of Mg-1Ca-1Sn alloy at strain rate $1x10^{-4}$ s^{-1} at 350°C (a) Static zone and (b), (c), (d), (e), (f) deformed Zone

For Mg-1Ca-1Sn alloy, after tensile test at strain rate $1x10^{-4}$ s^{-1} and at 400°C, microstructures of six positions are shown in Figure 4.36. At 'a' point, average grain size is 47.87 µm. At points 'b', 'c', 'd', 'e' and 'f', grain size are 65.92 µm, 97.21 µm, 103.71 µm, 101.95 µm and 98.09 µm, respectively. Maximum grain size is 103.71 µm.

For Mg-1Ca-1Sn alloy, after tensile test at strain rate $1x10^{-4}$ s^{-1} and at 450°C, microstructures of six positions are shown in Figure 4.37. At 'a' point, average grain size is 74.71 µm. At points 'b', 'c', 'd', 'e' and 'f', grain size are 92.29 µm, 103.29 µm, 238.71 µm, 175.78 µm and 183.69 µm, respectively. Maximum grain size is 238.71 µm.

With increasing temperature both static and dynamic grain growth increased for Mg-1Ca-1Sn alloy at strain rate $1x10^{-4}$ s^{-1}.

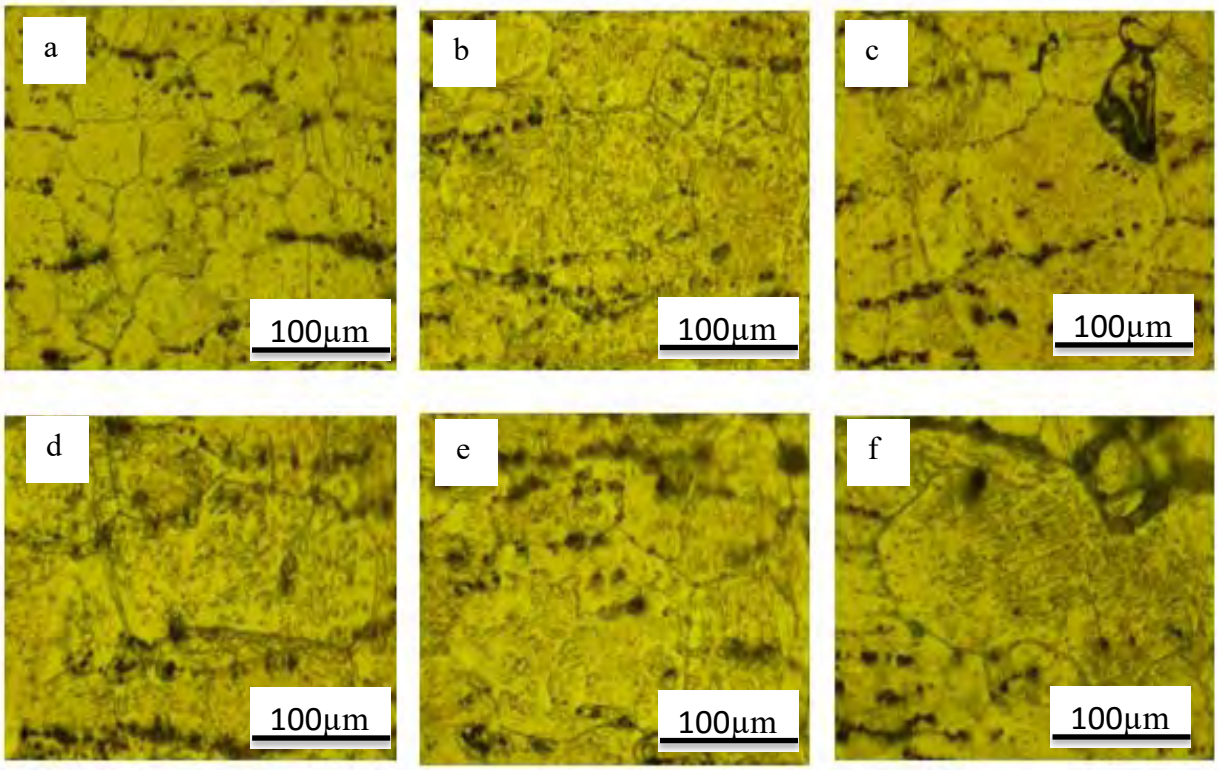

Figure 4.36: Optical microstructure of Mg-1Ca-1Sn alloy at strain rate $1x10^{-4}$ s^{-1} at 400°C (a) Static zone and (b), (c), (d), (e), (f) deformed Zone

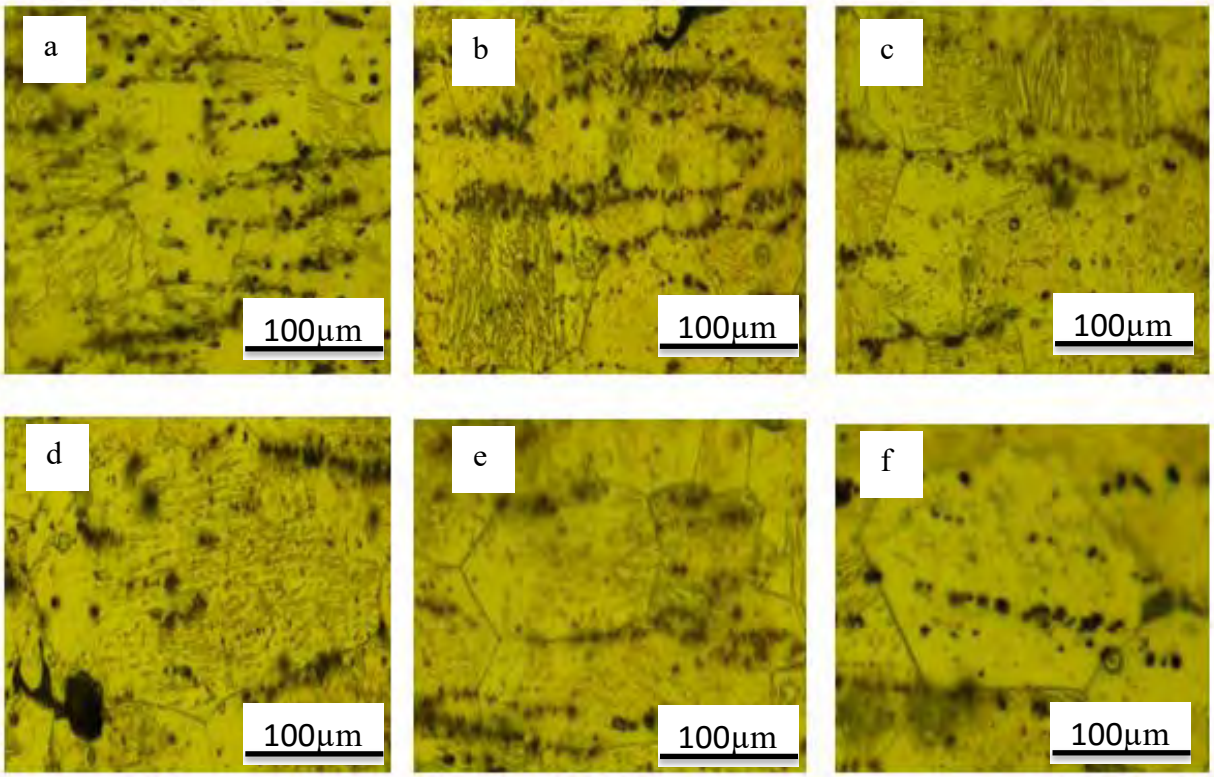

Figure 4.37: Optical microstructure of Mg-1Ca-1Sn alloy at strain rate $1x10^{-4}$ s^{-1} at 450°C (a) Static zone and (b), (c), (d), (e), (f) deformed Zone

For Mg-1Ca-2Sn alloy, after tensile test at strain rate $1x10^{-4}$ s^{-1} and at 300°C, microstructures of six positions are shown in Figure 4.38. At 'a' point, average grain size is 19.86 µm. At points 'b', 'c', 'd', 'e' and 'f', grain size are 28.13 µm, 43.95 µm, 29.53 µm, 30.70 µm and 36.39 µm, respectively. Maximum grain size is 43.95 µm.

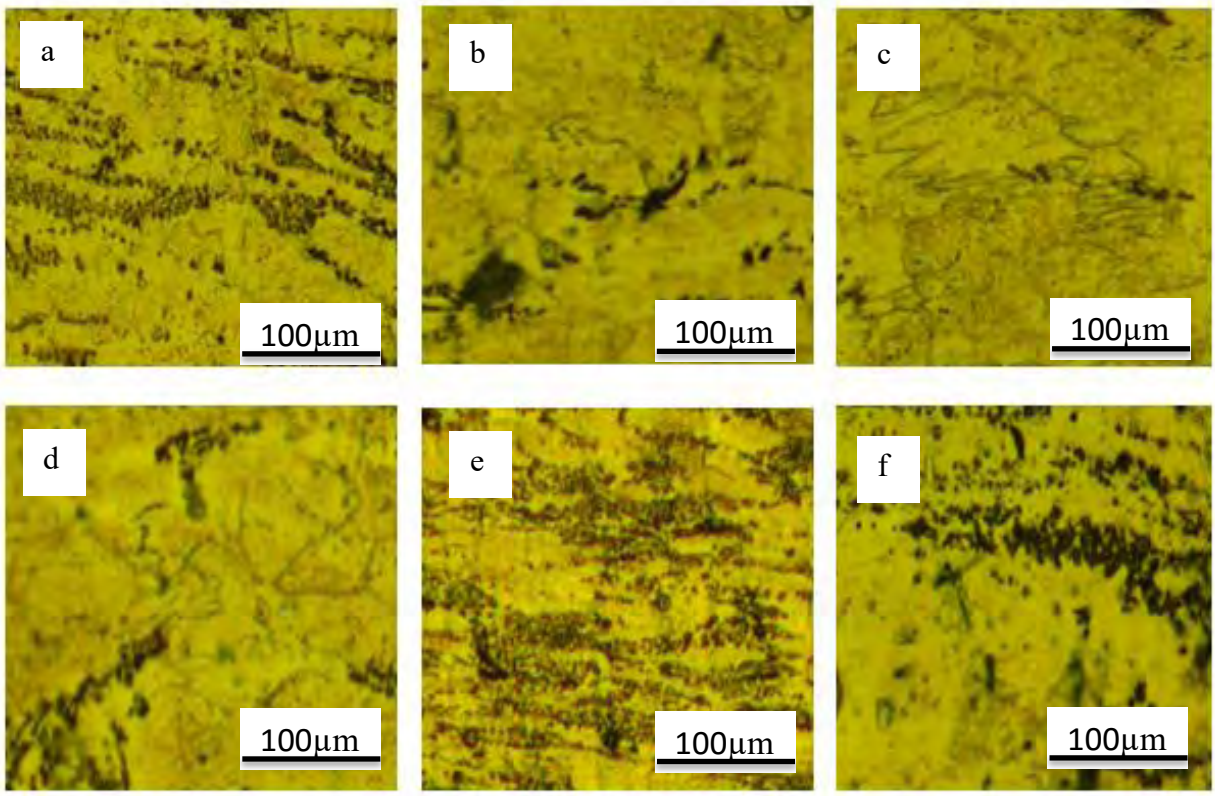

Figure 4.38: Optical microstructure of Mg-1Ca-2Sn alloy at strain rate $1x10^{-4}$ s^{-1} at 300°C (a) Static zone and (b), (c), (d), (e), (f) deformed Zone

For Mg-1Ca-2Sn alloy, after tensile test at strain rate $1x10^{-4}$ s^{-1} and at 350°C, microstructures of six positions are shown in Figure 4.39. At 'a' point, average grain size is 27.6 µm. At points 'b', 'c', 'd', 'e' and 'f', grain size are 36.17 µm, 46.45 µm, 99.32 µm, 51.86 µm and 41.31 µm, respectively. Maximum grain size is 99.32 µm.

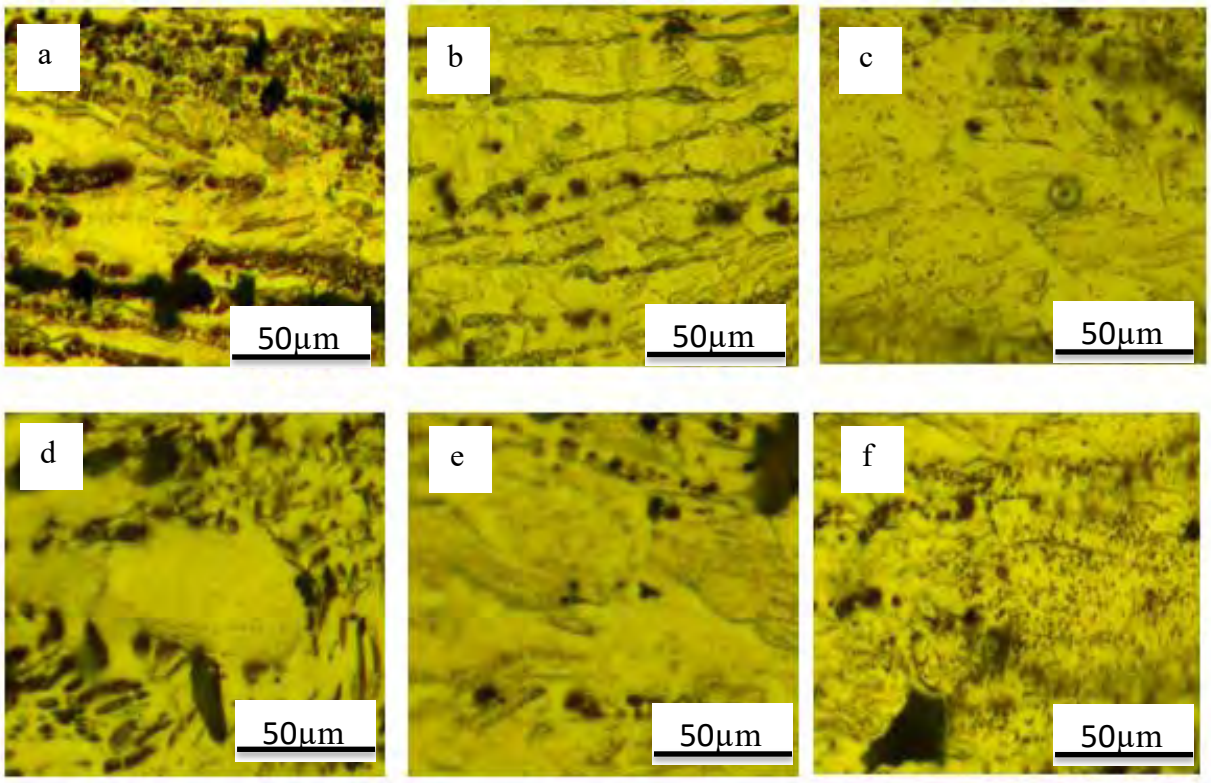

Figure 4.39: Optical microstructure of Mg-1Ca-2Sn alloy at strain rate $1x10^{-4}$ s^{-1} at 350°C (a) Static zone and (b), (c), (d), (e), (f) deformed Zone

For Mg-1Ca-2Sn alloy, after tensile test at strain rate $1x10^{-4}$ s^{-1} and at 400°C, microstructures of six positions are shown in Figure 4.40. At 'a' point, average grain size is 64.16 µm. At points 'b', 'c', 'd', 'e' and 'f', grain size are 79.45 µm, 100.80 µm, 150.82 µm, 136.76 µm and 95.45 µm, respectively. Maximum grain size is 150.82 µm.

For Mg-1Ca-2Sn alloy, after tensile test at strain rate $1x10^{-4}$ s^{-1} and at 450°C, microstructures of six positions are shown in Figure 4.41. At 'a' point, average grain size is 90.18 µm. At points 'b', 'c', 'd', 'e' and 'f', grain size are 94.04 µm, 143.26 µm, 130.43 µm, 125.3 µm and 110.7 µm, respectively. Maximum grain size is 143.26 µm.

With increasing temperature both static and dynamic grain growth increased for Mg-1Ca-2Sn alloy at strain rate $1x10^{-4}$ s^{-1}.

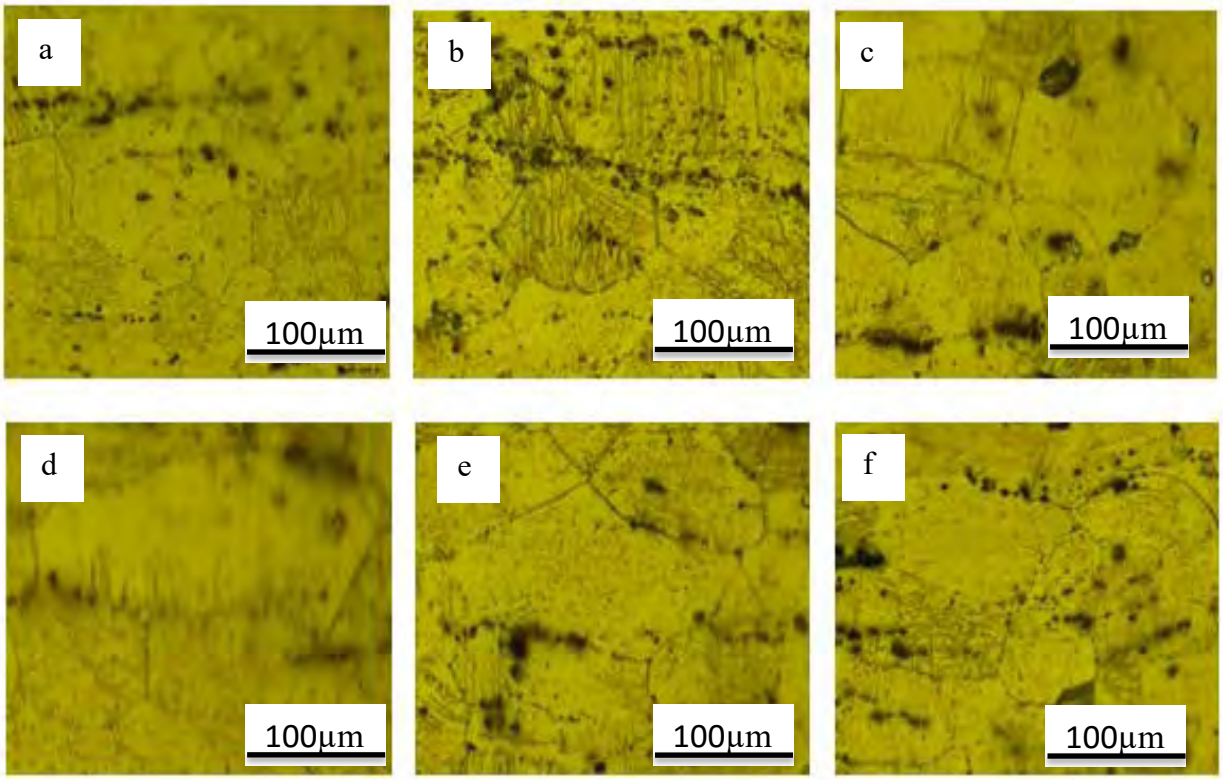

Figure 4.40: Optical microstructure of Mg-1Ca-4Sn alloy at strain rate $1x10^{-4}$ s^{-1} at 400°C (a) Static zone and (b), (c), (d), (e), (f) deformed Zone

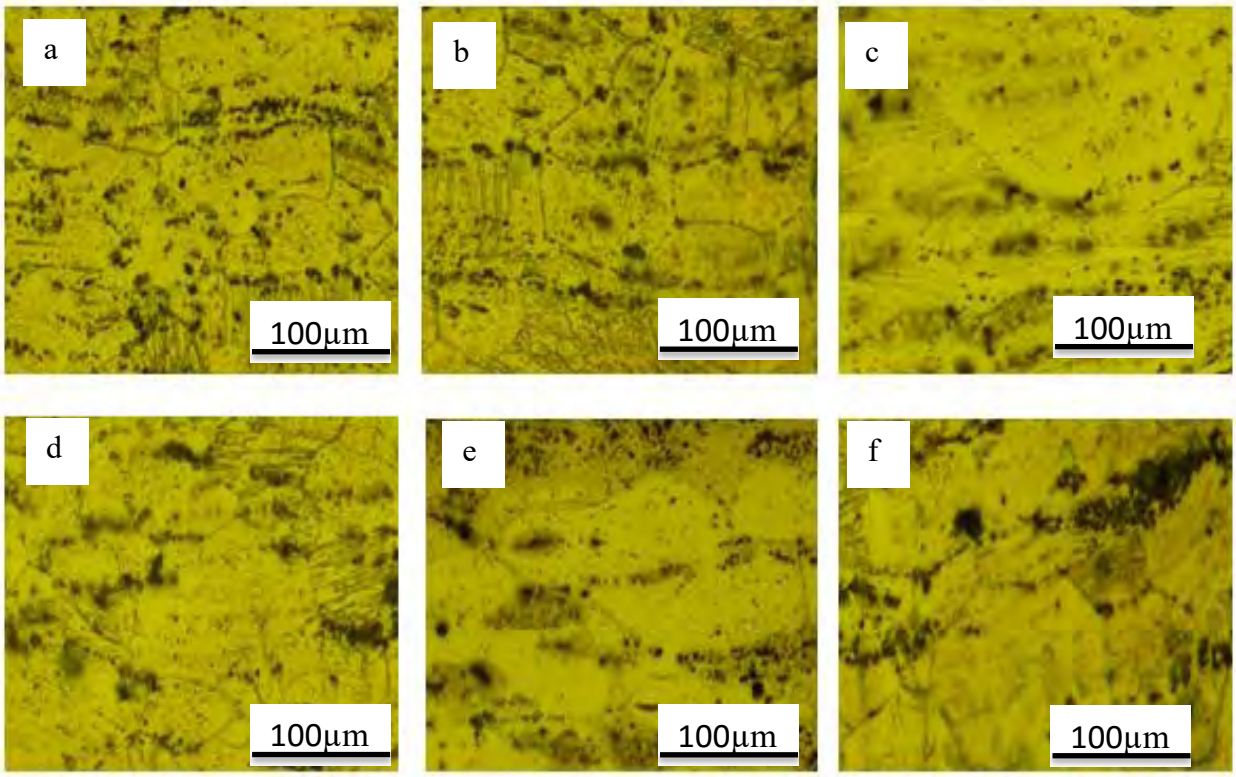

Figure 4.41: Optical microstructure of Mg-1Ca-4Sn alloy at strain rate $1x10^{-4}$ s^{-1} at 450°C (a) Static zone and (b), (c), (d), (e), (f) deformed Zone

For Mg-1Ca-4Sn alloy, after tensile test at strain rate $1x10^{-4}$ s^{-1} and at 300°C, microstructures of six positions are shown in Figure 4.42. At 'a' point, average grain size is 19.73 µm. Due to addition of 4% Sn, grain size decreased in this alloy than Mg-1Ca-2Sn alloy. At points 'b', 'c', 'd', 'e' and 'f', grain size are 25.97 µm, 29.17 µm, 31.99 µm, 38.32 µm and 58.36 µm, respectively. Maximum grain size is 58.36 µm.

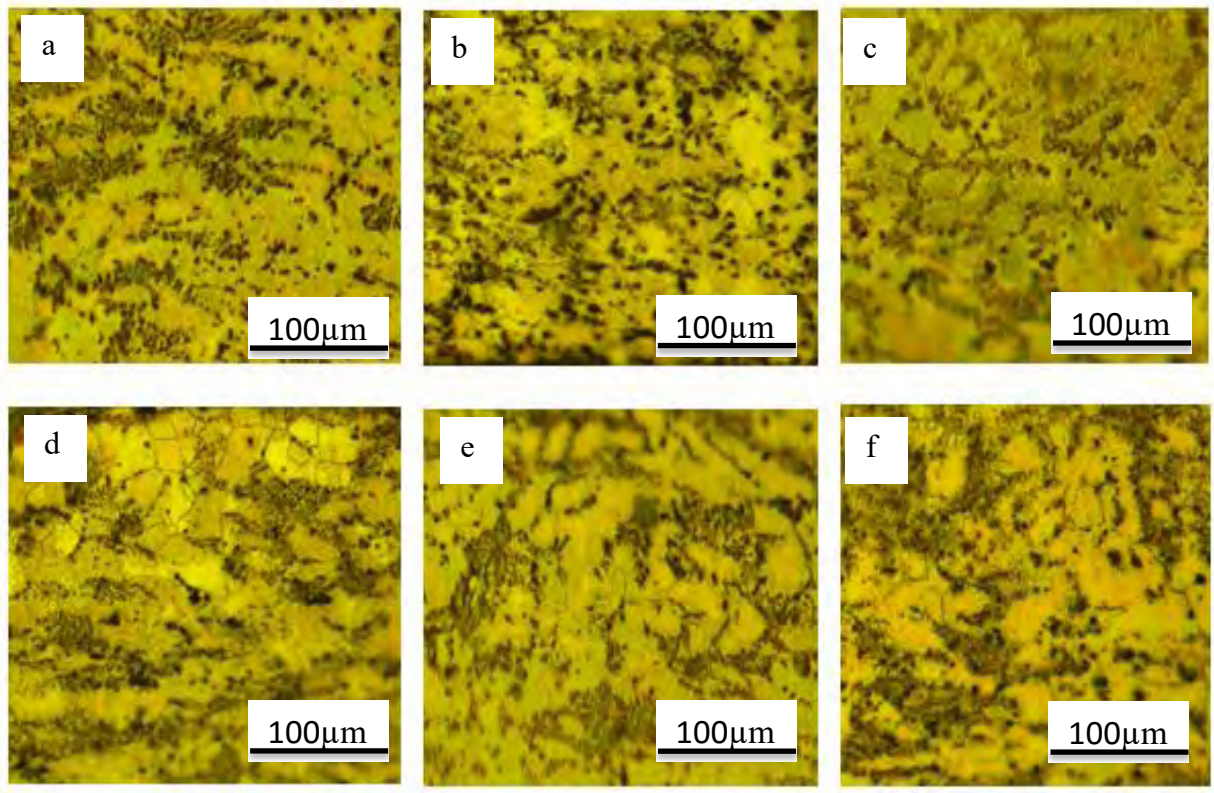

Figure 4.42: Optical microstructure of Mg-1Ca-4Sn alloy at strain rate $1x10^{-4}$ s^{-1} at 300°C (a) Static zone and (b), (c), (d), (e), (f) deformed Zone

For Mg-1Ca-4Sn alloy, after tensile test at strain rate $1x10^{-4}$ s^{-1} and at 350°C, microstructures of six positions are shown in Figure 4.43. At 'a' point, average grain size is 28.14 µm. At points 'b', 'c', 'd', 'e' and 'f', grain size are 33.93 µm, 58.54 µm, 67.68 µm, 51.86 µm and 61.00 µm, respectively. Maximum grain size is 67.68 µm.

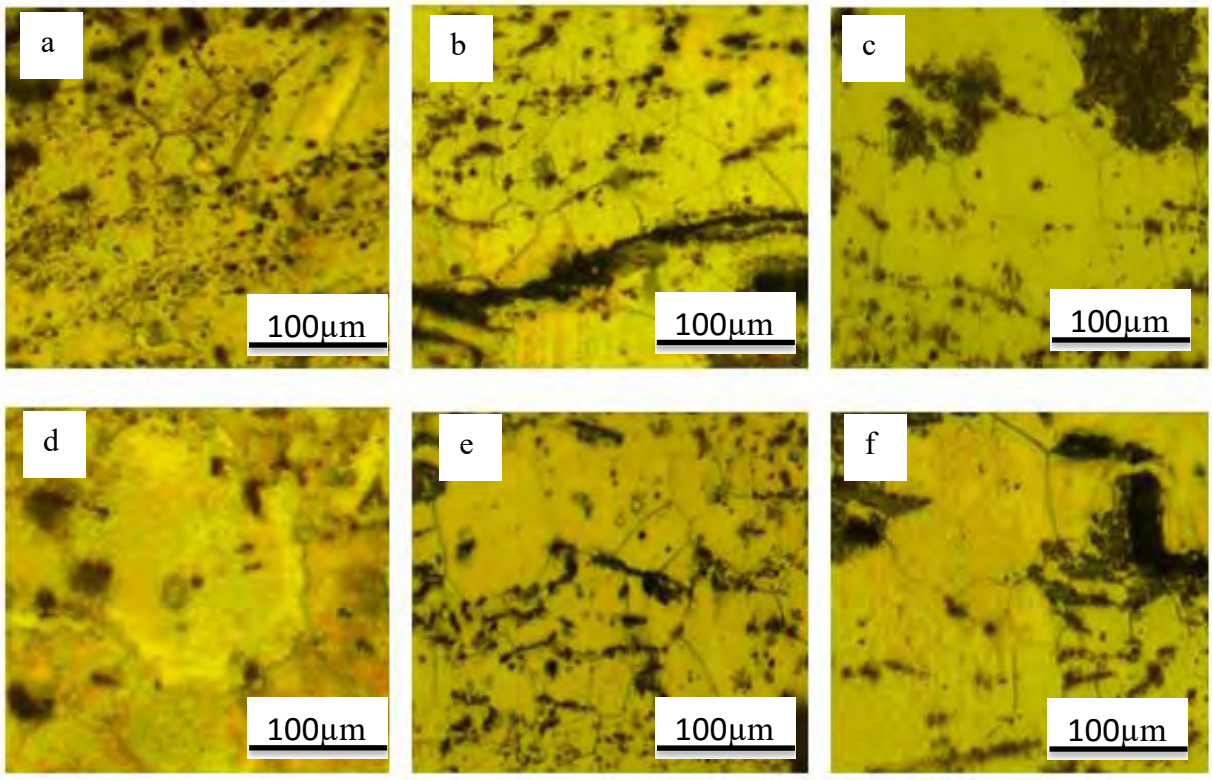

Figure 4.43: Optical microstructure of Mg-1Ca-4Sn alloy at strain rate $1x10^{-4}$ s^{-1} at 350°C (a) Static zone and (b), (c), (d), (e), (f) deformed Zone

For Mg-1Ca-4Sn alloy, after tensile test at strain rate $1x10^{-4}$ s^{-1} and at 400°C, microstructures of six positions are shown in Figure 4.44. At 'a' point, average grain size is 39.55 µm. At points 'b', 'c', 'd', 'e' and 'f', grain size are 47.46 µm, 72.95 µm, 77.43 µm, 79.60 µm and 87.01 µm, respectively. Maximum grain size is 87.01 µm.

Mg-1Ca-4Sn alloy after tensile test at strain rate $1x10^{-4}$ s^{-1} and at 450°C, formed oxide and deteriorated.

With increasing temperature both static and dynamic grain growth increased for Mg-1Ca-4Sn alloy at strain rate $1x10^{-4}$ s^{-1}.

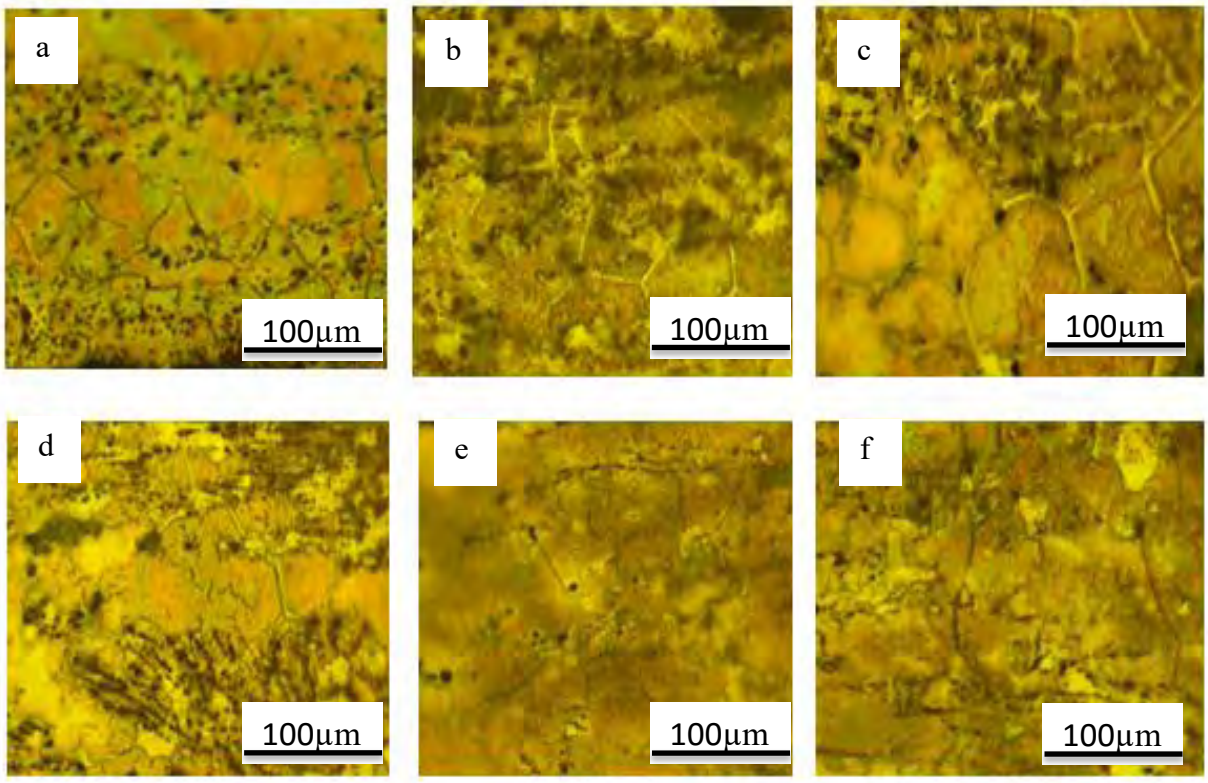

Figure 4.44: Optical microstructure of Mg-1Ca-4Sn alloy at strain rate $1x10^{-4}$ s^{-1} at 400°C (a) Static zone and (b), (c), (d), (e), (f) deformed Zone

At strain rate $1x10^{-4}$ s^{-1}, grain growth in the gauge region is higher than that in the grip region for all alloys. Maximum grain size is before some distance of fracture point. With increasing Sn content, grain size decreased in both grip and gauge regions. However, with increasing temperature, grain size increased in both regions. Thus, both static and dynamic grain growth increased for all alloys with increasing temperature. At 450°C, 4% Sn containing alloy formed oxide, which made this alloy collapsed.

4.6.3. Comparison between Two Strain Rates

In Figure 4.45, grain size variation with temperature at grip and gauge region for Mg-1Ca alloy is shown. Grain size of grip region is taken from 'a' point of all alloys and among points 'b', 'c', 'd', 'e' and 'f' of gauge region, one fixed point (as 'd' point) is taken for all alloys. With increasing temperature, grain size increased in both grip and gauge regions. It is due to high temperature softening. From Figure 4.45(a), it is seen that for all temperatures, grain size of gauge region is larger than grip region at strain rate $5x10^{-4}$ s^{-1}. This is also

observed at strain rate $1x10^{-4}$ s^{-1} in Figure 4.45(b). At gauge region, grain growth happens for high temperature loading, but in grip region grain growth happens only for holding at high temperature, no loading is involve in this region. So, in gauge region grain grows more than grip region. However, at slower strain rate $1x10^{-4}$ s^{-1}, at each point, grain size is larger than grain size at higher strain rate $5x10^{-4}$ s^{-1}. It is because at slower strain rate grain gets more time to grow and starting of neck formation delays.

Other researchers observed the similar results in grip and gauge regions [51-53]. Jeong [51] observed that, in the gauge region, rapid grain growth took place. Li [52] and Zhang [53] observed that dynamic grain growth was higher than static grain growth. Moreover, Zhang [53] observed larger grain size at slower strain rate.

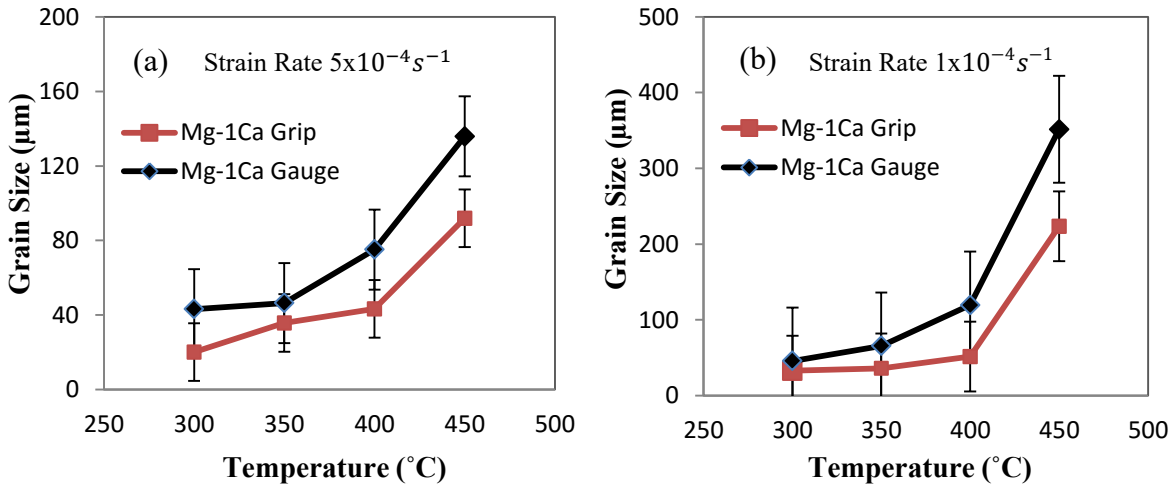

Figure 4.45: Grain size variation with temperature at grip and gauge region for Mg-1Ca alloy at (a) strain rate $5x10^{-4}$ s^{-1} and (b) strain rate $1x10^{-4}$ s^{-1}

In Figure 4.46, grain size variation with temperature at grip and gauge regions for Mg-1Ca-1Sn alloy is shown. With increasing temperature, grain size increased in both grip and gauge regions. For all temperatures, grain size of gauge region is larger than grip region at strain rates $5x10^{-4}$ s^{-1} and $1x10^{-4}$ s^{-1}. Grain size at slower strain rate $1x10^{-4}$ s^{-1} [Figure 4.46(b)] is larger than grain size at higher strain rate $5x10^{-4}$ s^{-1} [Figure 4.46(a)]. Grain size in both grip and gauge regions decreased in this alloy than Mg-1Ca alloy. It is because 1% Sn addition.

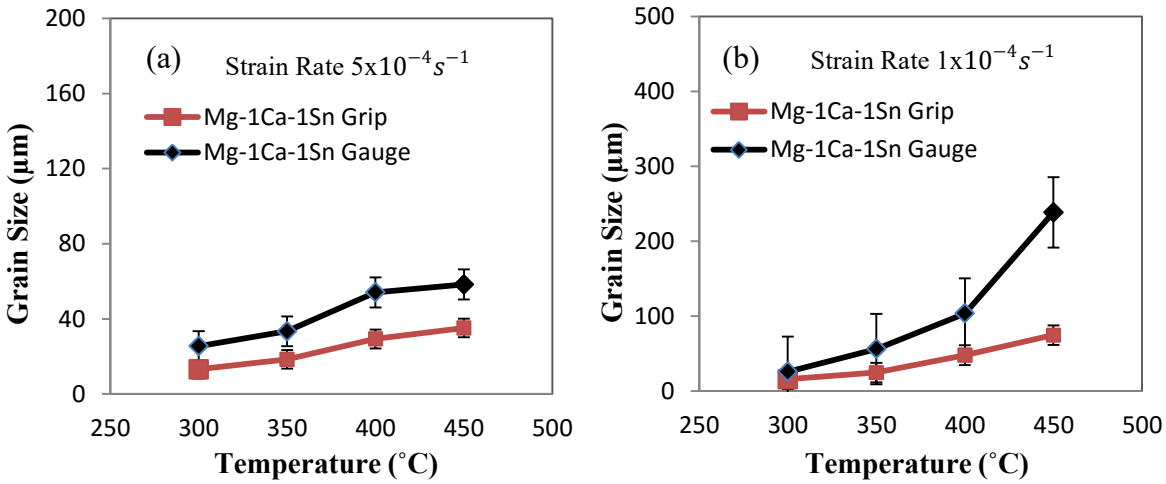

Figure 4.46: Grain size variation with temperature at grip and gauge region for Mg-1Ca-1Sn alloy at (a) strain rate 5x10^{-4} s^{-1} and (b) strain rate 1x10^{-4} s^{-1}

In Figure 4.47, grain size variation with temperature at grip and gauge regions for Mg-1Ca-2Sn alloy is shown. With increasing temperature, grain size increased in both grip and gauge regions at strain rate 5x10^{-4} s^{-1} [Figure 4.47(a)]. However, at strain rate 1x10^{-4} s^{-1}, grain size increase up to 400°C, then decreased slightly at 450°C [Figure 4.47(b)]. It is because of oxide formation at high temperature. For all temperatures, grain size of gauge region is larger than grip region. Grain size at slower strain rate 1x10^{-4} s^{-1} is larger than grain size at higher strain rate 5x10^{-4} s^{-1}. Grain size in both grip and gauge regions decreased in this alloy than that of Mg-1Ca-1Sn alloy. It is because more Sn addition.

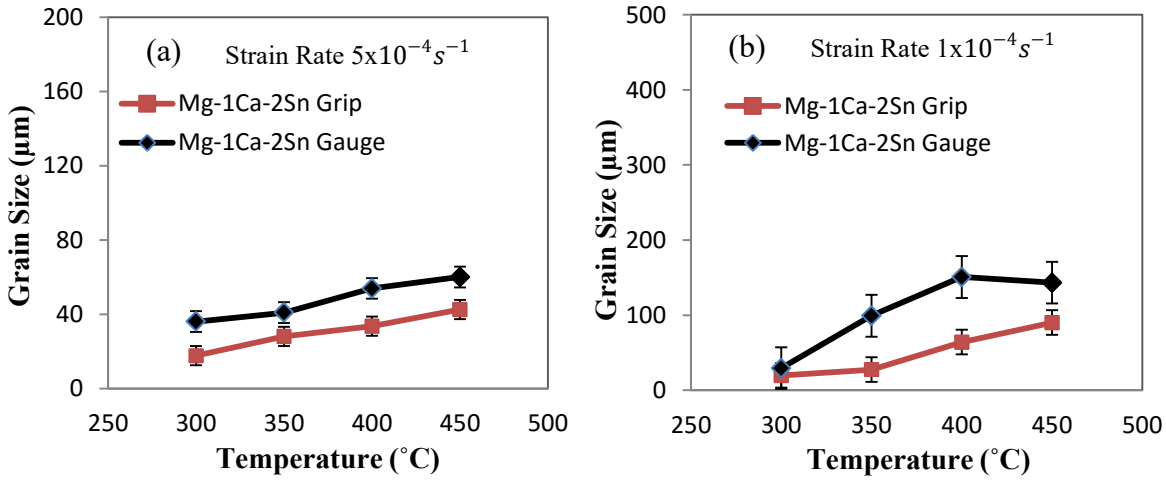

Figure 4.47: Grain size variation with temperature at grip and gauge region for Mg-1Ca-2Sn alloy at (a) strain rate 5x10^{-4} s^{-1} and (b) strain rate 1x10^{-4} s^{-1}

In Figure 4.48, grain size variation with temperature at grip and gauge region for Mg-1Ca-4Sn alloy is shown. With increasing temperature, grain size increased in both grip and gauge regions at strain rate $5x10^{-4}$ s^{-1} [Figure 4.48(a)]. However, at strain rate $1x10^{-4}$ s^{-1}, grain size increase up to 400°C, then at 450°C, grain size is found very small [Figure 4.48(b)]. It is because of high oxide formation at high temperature due to high amount of Sn addition. Grain size at slower strain rate $1x10^{-4}$ s^{-1} is smaller than grain size at higher strain rate $5x10^{-4}$ s^{-1}. It is because, with high amount of Sn addition, excessive intermetallic formed and this increased the oxide formation. Thus, property totally deteriorated at slower strain rate and high temperature.

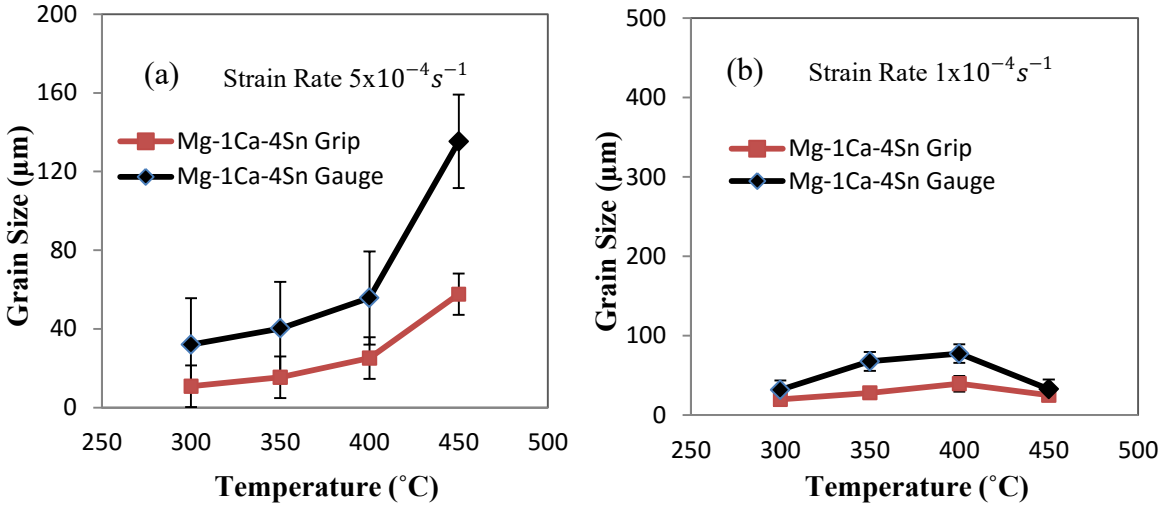

Figure 4.48: Grain size variation with temperature at grip and gauge region for Mg-1Ca-4Sn alloy at (a) strain rate $5x10^{-4}$ s^{-1} and (b) strain rate $1x10^{-4}$ s^{-1}

Grain growth became larger in both grip and gauge regions with slower strain rate $1x10^{-4}$ s^{-1} than strain rate $5x10^{-4}$ s^{-1}. With addition of Sn, grain size decreased, in contrast, with increasing temperature, grain size increased at both strain rates. However, at 450°C and at strain rate $1x10^{-4}$ s^{-1}, with 2% and 4% Sn addition, grain size decreased, because of formation of oxide.

4.7 Deformation Mechanism of Grain Growth

4.7.1 Activation Energy Calculation

General equation [48] for grain growth is given below:

$$d^n - d_o^{\,n} = K_o t \exp\left(\frac{-Q_g}{RT}\right)$$

$$\text{Or, } \ln\left[d^n - d_o^{\,n}\right] = \ln\left[K_o t\right] + \left(\frac{-Q_g}{RT}\right)$$

Here, d is the grain size at a given annealing time;

d_o is the initial grain size;

K_o is a constant;

Q_g is the activation energy for grain growth;

R is the molar constant;

t is the annealing time;

T is temperature and n=2.

$\ln[\, d^n - d_o^{\,n}\,]$ against (1/RT) is plotted for the estimation of activation energy (Q_g). In Figure 4.49(a), $\ln[\, d^n - d_o^{\,n}\,]$ against (1/RT) is plotted at strain rate $5\text{x}10^{-4}$ s^{-1} and in Figure 4.49(b), $\ln[\, d^n - d_o^{\,n}\,]$ against (1/RT) is plotted at strain rate $1\text{x}10^{-4}$ s^{-1} . From the slope of these curves, activation energy can calculate.

Slope = - Q_g

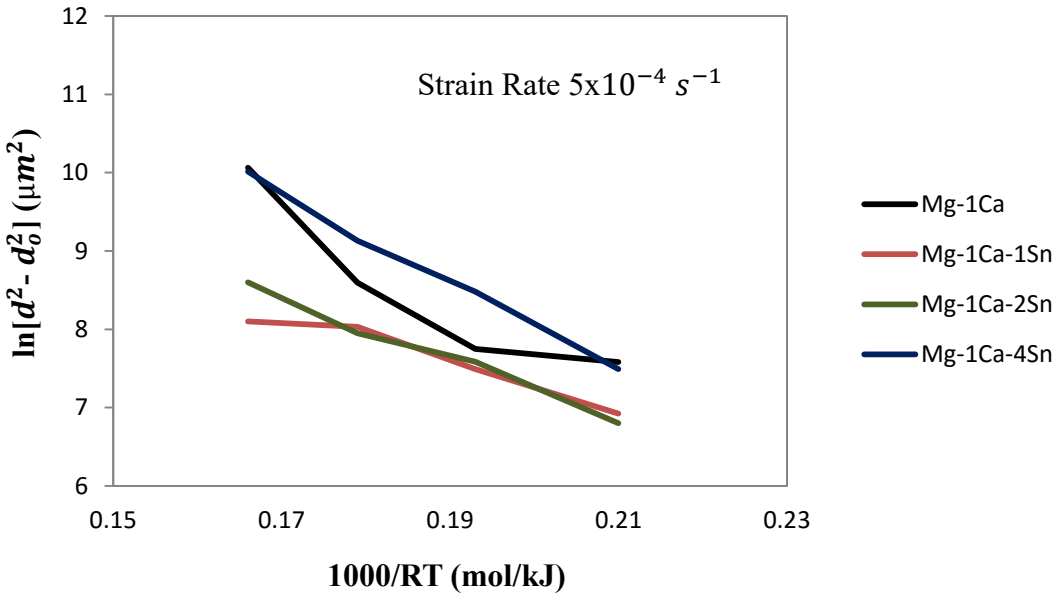

Figure 4.49(a): Plot of ln[d^n-$d_o{}^n$] against (1/RT) at strain rate 5x10^{-4} s^{-1}

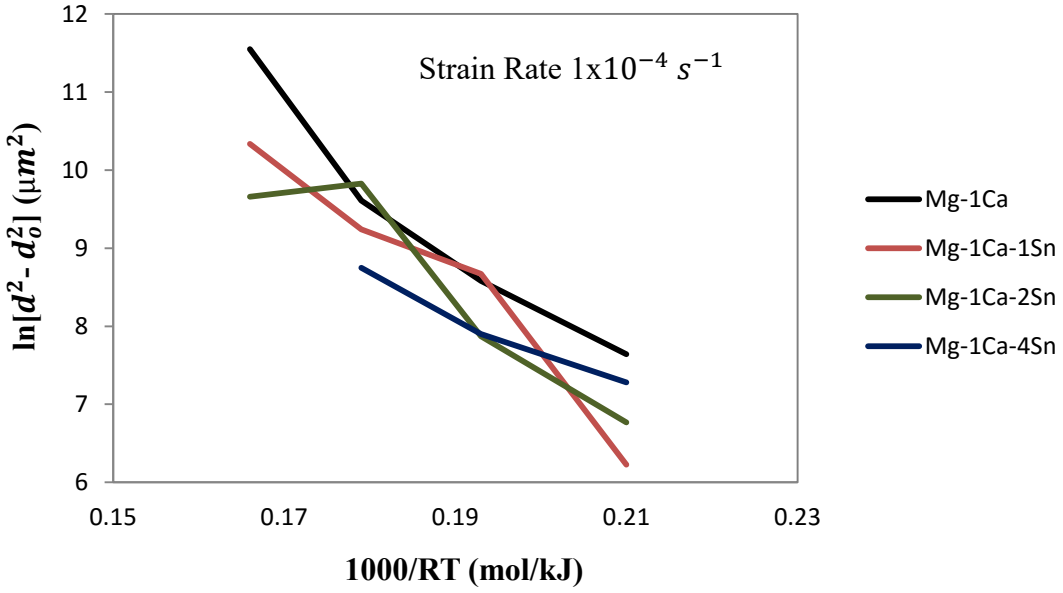

Figure 4.49(b): Plot of ln[d^n-$d_o{}^n$] against (1/RT) at strain rate 1x10^{-4} s^{-1}

Values of activation energy calculated at strain rate 5x10^{-4} s^{-1} are given in Table 4.3, and values of activation energy calculated at strain rate 1x10^{-4} s^{-1} are given in Table 4.4. Activation energy for grain boundary diffusion is 92 kJmol^{-1} and activation energy for lattice self-diffusion is 135 kJmol^{-1} in pure Mg [48], [54]. From Table 4.3, it is found that at higher strain rate 5x10^{-4} s^{-1}, values of activation energy are between 5 to 123 kJmol^{-1} [Table 4.3], which are below 135 kJmol^{-1}. Therefore, grain boundary diffusion mechanism took place for grain growth. However, at slower strain rate (1x10^{-4} s^{-1}), some values of

activation energy are above 135 $kJmol^{-1}$ [Table 4.4]. Thus, deformation mechanism changed from grain boundary diffusion to lattice diffusion, with changing strain rate from higher to slower.

Table 4.3: Value of Q_g at strain rate $5x10^{-4}$ s^{-1}

ALLOY	$Q_g(kJ\ mol^{-1})$		
	300-350°C	**350-400°C**	**400-450°C**
Mg-1Ca	10	60.29	112.85
Mg-1Ca-1Sn	33.41	38.7	5.25
Mg-1Ca-2Sn	46.12	26.07	50.08
Mg-1Ca-4Sn	58.24	46.43	67.92

Table 4.4: Value of Q_g at strain rate $1x10^{-4}$ s^{-1}

ALLOY	$Q_g(kJ\ mol^{-1})$		
	300-350°C	**350-400°C**	**400-450°C**
Mg-1Ca	55.12	73.57	149.23
Mg-1Ca-1Sn	143.82	40.71	84.23
Mg-1Ca-2Sn	64.71	140	13.08
Mg-1Ca-4Sn	36.47	60.71	-

At strain rate $5x10^{-4}$ s^{-1}, only grain boundary diffusion mechanism is found for grain growth. However, at slower strain rate ($1x10^{-4}$ s^{-1}), deformation mechanism changed from grain boundary diffusion to lattice diffusion.

Deformation mechanisms from activation energy are found based on only two values of Q_g. Therefore, finding out deformation mechanisms by using values of activation energy is not a proper way. In practical, strain hardening exponent or strain rate sensitivity index is used for understanding deformation mechanisms.

4.7.2 Strain Hardening Exponent and Strain Rate Sensitivity Index Calculation

From the relation of true stress and true strain,

$$\sigma = K\,\varepsilon^{n}$$

$$\text{Or, } \ln\sigma = \ln K + n \ln\varepsilon$$

Here,

σ is true stress;

ε is true strain;

n is strain hardening exponent and

m is strain rate sensitivity index.

m is inversely proportional to n [54]. Thus, m = 1/n.

lnσ against lnε is plotted for the estimation of strain hardening exponent (n). In Figure 4.50, lnσ against lnε is plotted at strain rate $5x10^{-4}$ s^{-1} for (a) Mg-1Ca, (b) Mg-1Ca-1Sn, (c) Mg-1Ca-2Sn and (d) Mg-1Ca-4Sn alloy and in Figure 4.50, lnσ against lnε is plotted at strain rate $1x10^{-4}$ s^{-1} for (e) Mg-1Ca, (f) Mg-1Ca-1Sn, (g) Mg-1Ca-2Sn and (h) Mg-1Ca-4Sn alloy. From the slope of these curves, strain hardening exponent (n) can be calculated.

Slope = n

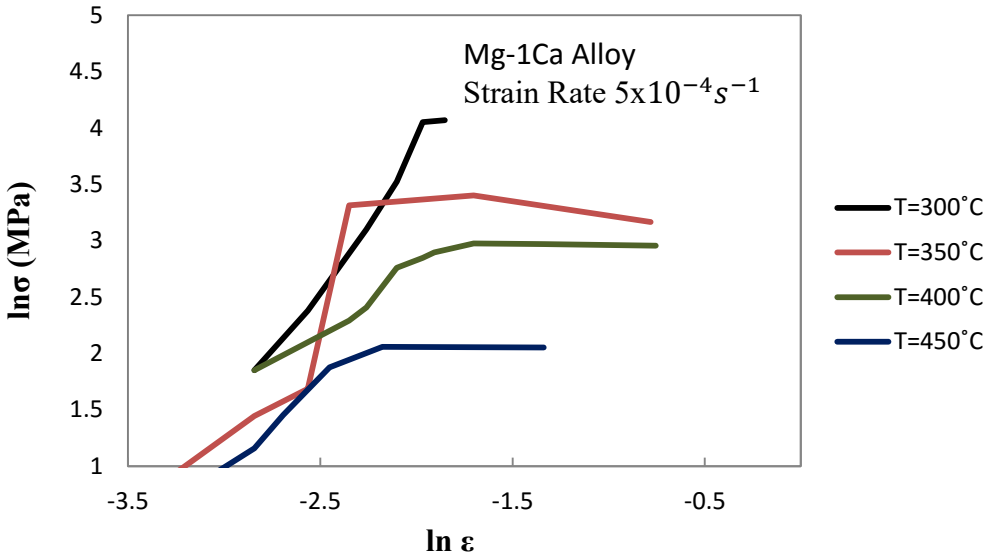

Figure 4.50(a): Plot of lnσ against lnε at strain rate 5x10^{-4} s^{-1} of Mg-1Ca alloy

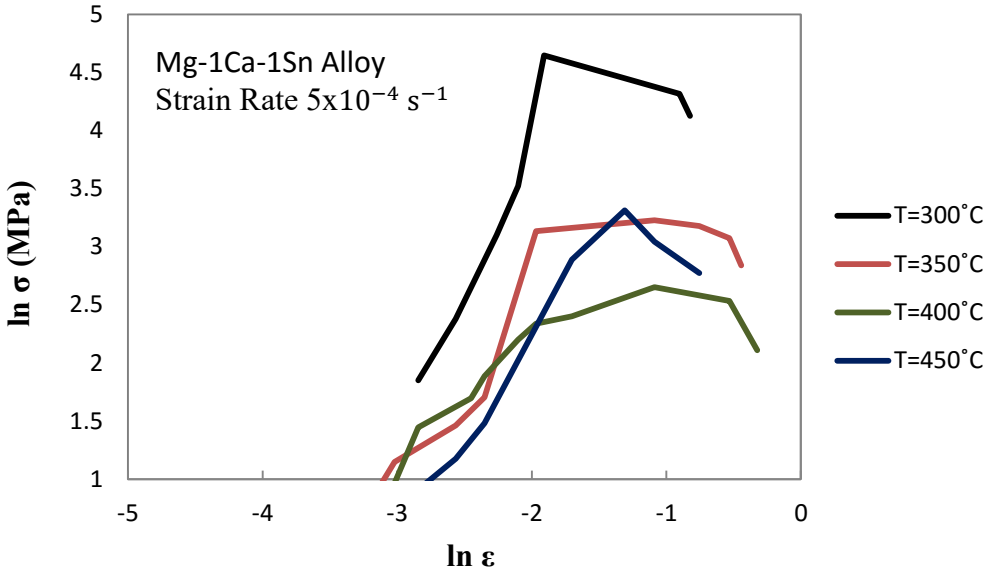

Figure 4.50(b): Plot of lnσ against lnε at strain rate 5x10^{-4} s^{-1} of Mg-1Ca-1Sn alloy

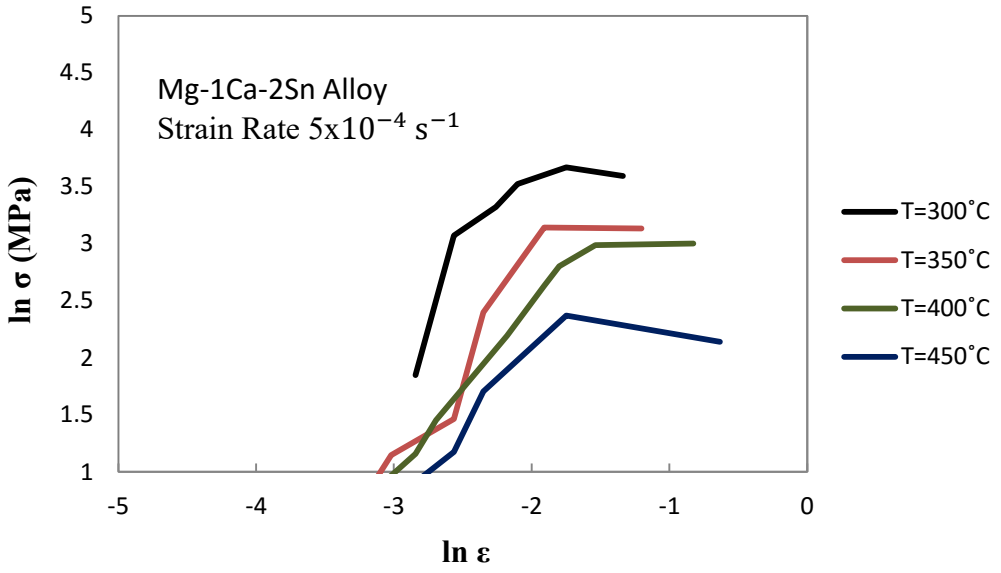

Figure 4.50(c): Plot of lnσ against lnε at strain rate 5x10^{-4} s^{-1} of Mg-1Ca-2Sn alloy

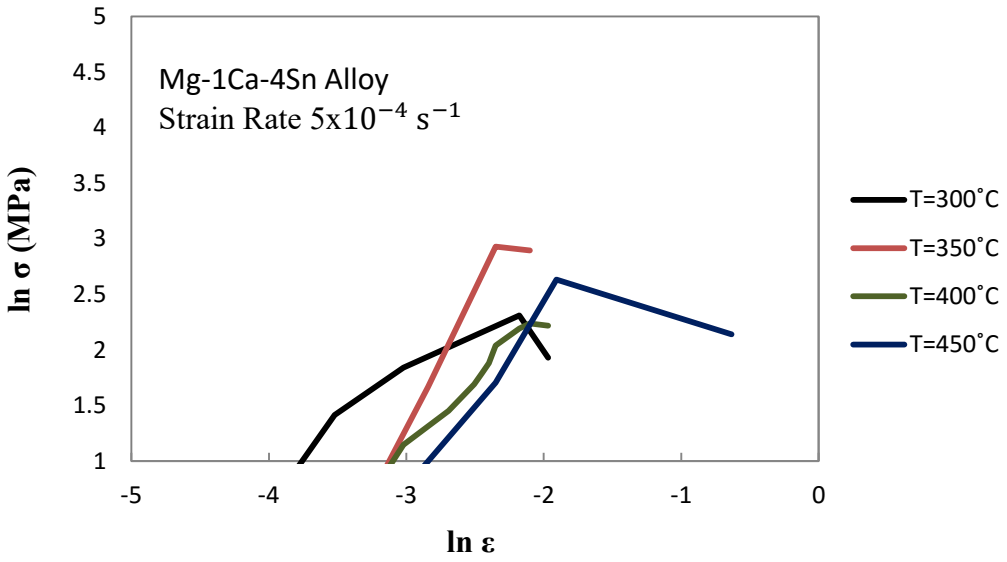

Figure 4.50(d): Plot of lnσ against lnε at strain rate 5x10^{-4} s^{-1} of Mg-1Ca-4Sn alloy

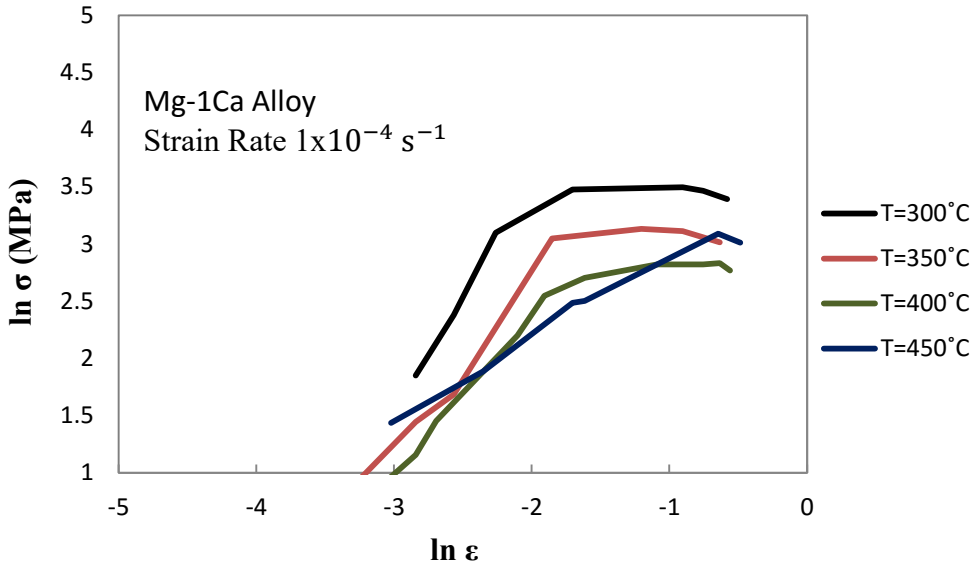

Figure 4.50(e): Plot of lnσ against lnε at strain rate 1x10^{-4} s^{-1} of Mg-1Ca alloy

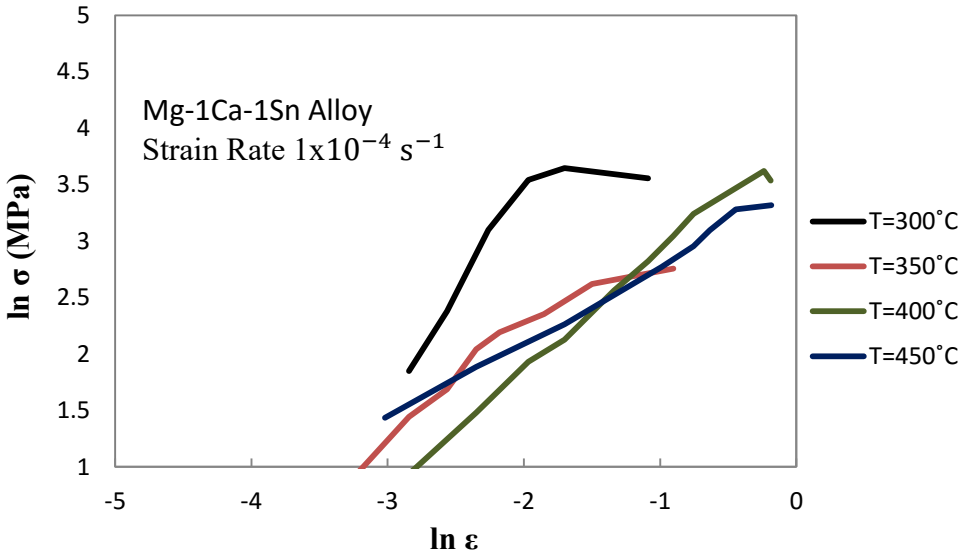

Figure 4.50(f): Plot of lnσ against lnε at strain rate 1x10^{-4} s^{-1} of Mg-1Ca-1Sn alloy

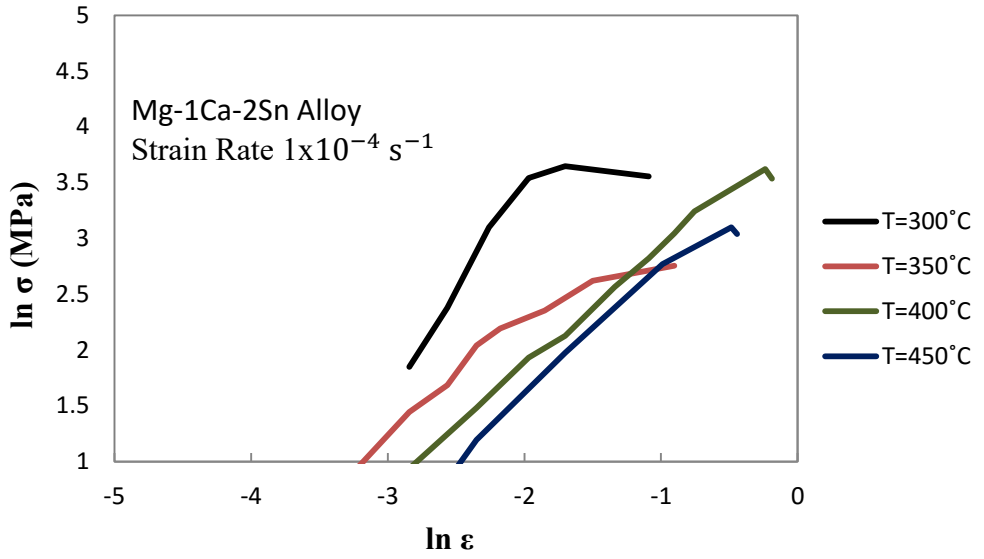

Figure 4.50(g): Plot of lnσ against lnε at strain rate 1x10^{-4} s^{-1} of Mg-1Ca-2Sn alloy

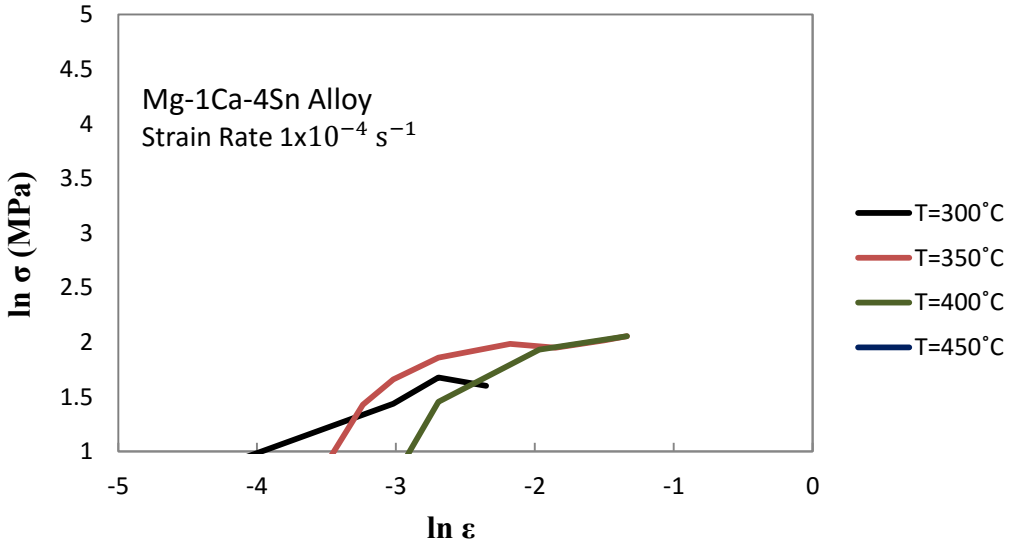

Figure 4.50(h): Plot of lnσ against lnε at strain rate 1x10^{-4} s^{-1} of Mg-1Ca-4Sn alloy

Deformation mechanism at elevated temperatures for different n value is given below [55]:

n= 1 (Diffusional creep)

n= 2 (Grain boundary sliding)

n= 3 (Glide-controlled creep)

n= 4-5 (Climb-controlled creep)

n> 8 (Dispersion-strengthened alloy)

In Tables 4.5 and 4.6, values of n at strain rate $5x10^{-4}$ s^{-1} and $1x10^{-4}$ s^{-1} are shown respectively. From Table 4.5, it is found that at higher strain rate $5x10^{-4}$ s^{-1}, different mechanisms like diffusional creep, grain boundary sliding, glide-controlled creep and climb-controlled creep are happened. However, at slower strain rate ($1x10^{-4}$ s^{-1}), from Table 4.6, only diffusional creep and grain boundary sliding are identified.

Table 4.5: Value of n at strain rate $5x10^{-4}$ s^{-1}

ALLOY	n			
	300°C	350°C	400°C	450°C
Mg-1Ca	2.93	6.9	2.91	1.83
Mg-1Ca-1Sn	2.38	3.57	1.47	2.22
Mg-1Ca-2Sn	5	5.47	1.43	1.13
Mg-1Ca-4Sn	2.73	2.66	1.08	1.28

Table 4.6: Value of n at strain rate $1x10^{-4}$ s^{-1}

ALLOY	n			
	300°C	350°C	400°C	450°C
Mg-1Ca	2	2.07	1.47	1
Mg-1Ca-1Sn	1.88	1	2.03	1.07
Mg-1Ca-2Sn	2.18	1.1	1.25	1.08
Mg-1Ca-4Sn	1	2.27	1.52	-

Strain rate sensitivity index (m) is calculated from inverse of strain hardening exponent (n).

Deformation mechanism for different m value is given below [55]:

m= 1 (Diffusional creep)

m= 0.5 (Grain boundary sliding)

m= 0.33 (Glide-controlled creep)

m= 0.14-0.25 (Climb-controlled creep)

m< 0.125 (Dispersion-strengthened alloy)

In Tables 4.7 and 4.8, values of m at strain rate $5x10^{-4}$ s^{-1} and $1x10^{-4}$ s^{-1} are shown respectively.

Table 4.7: Value of m at strain rate $5x10^{-4}$ s^{-1}

ALLOY	m			
	300°C	350°C	400°C	450°C
Mg-1Ca	0.34	0.15	0.34	0.55
Mg-1Ca-1Sn	0.42	0.28	0.68	0.45
Mg-1Ca-2Sn	0.20	0.18	0.70	0.89
Mg-1Ca-4Sn	0.37	0.37	0.93	0.78

Table 4.8: Value of m at strain rate $1x10^{-4}$ s^{-1}

ALLOY	m			
	300°C	350°C	400°C	450°C
Mg-1Ca	0.5	0.48	0.68	1
Mg-1Ca-1Sn	0.53	1	0.49	0.94
Mg-1Ca-2Sn	0.46	0.91	0.80	0.93
Mg-1Ca-4Sn	1	0.44	0.66	-

In Figure 4.51, plot of value of m against elongation to failure (%) is shown. In this figure, 'red' colored points indicate strain rate of $5x10^{-4}$ s^{-1} and 'blue' colored points indicate strain rate of $1x10^{-4}$ s^{-1}.

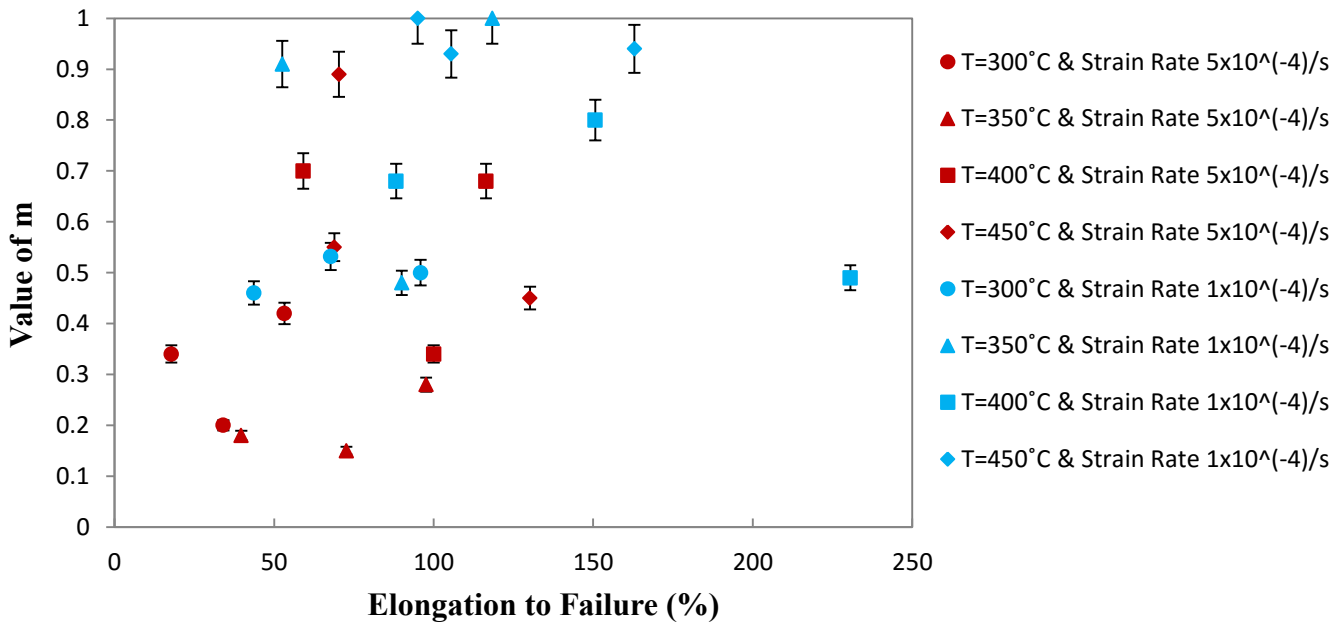

Figure 4.51: Plot of Value of m against Elongation to Failure (%)

At higher strain rate $5x10^{-4}$ s^{-1}, values of m are scattered from 0.15 to 0.89. Therefore, different mechanisms as climb controlled creep (for m= 0.14-0.25), glide controlled creep (for m= 0.33) and grain boundary sliding (for m= 0.5) are followed for grain growth at higher

strain rate. However, at slower strain rate $1x10^{-4}$ s^{-1}, values of m are scattered from 0.46 to 1, which indicated grain boundary sliding (for m= 0.5) and diffusional creep (for m= 1) mechanisms for grain growth.

With increasing elongation to failure, value of m shifted higher in the plot of Figure 4.51. This indicated increase of m value. Thus, with higher elongation to failure, deformation mechanism changes from glide and climb controlled mechanism to grain boundary sliding and diffusional creep.

Superplastic alloys exhibit m>0.33. Grain boundary sliding is generally predominant mode of deformation during superplastic flow. In this case activation energy is either equal to activation energy for lattice diffusion, or to the activation energy for grain boundary diffusion [55]. Therefore, at slower strain rate, all of the four alloys showed superplastic behavior, because of high value of m and elongation to failure.

Chapter 5
Conclusions

The objective of this work was to investigate the effects of Sn on microstructure and dynamic grain growth behavior in Mg-1Ca alloy at different temperatures and at different strain rates. Results obtained from this work can be summarized as follows:

1) Microstructure of as-cast samples revealed that Sn addition increased dendrite formation. With increasing Sn content, dendrite became larger.

2) Microstructure of rolled samples showed that grain size of rolled sample became small with increasing Sn content in alloy, thus more recrystallization happened.

3) SEM results declared that in Mg-1Ca alloy, there was a prominent phase Mg_2Ca. With small Sn addition CaMgSn phase formed and with addition of more Sn, another Mg_2Sn phase formed.

4) Sn addition increased the formation of intermetallic particles. Particles became more circular with increasing Sn addition.

5) Tensile test result showed that ultimate tensile strength and elongation to failure increased with 1% Sn addition because of grain refinement. But with increasing Sn addition to 2% and 4%, both ultimate tensile strength and elongation to failure degraded because of excessive intermetallic particle formation.

6) At slower strain rate, the onset of neck formation was delayed and grain growth happened. Thus, strength decreased but elongation to failure increased.

7) At high temperature, flow softening happened, thus, lower strength and higher elongation to failure were observed with increasing temperature.

8) At high temperature and with high percentage of Sn addition, oxide formed. As a result, at 450°C, very low value of strength and elongation to failure was observed. At this temperature and at slower strain rate, alloy became fully oxidized.

9) With increasing temperature both static grain growth (SGG) and dynamic grain growth (DGG) increased. Dynamic grain growth was always higher than static grain growth. At slower strain rate more grain growth was observed.

10) At different temperatures and strain rates, deformation mechanisms varied. According to the value of activation energy, at higher strain rate, grain boundary diffusion was the deformation mechanism. At slower strain rate, deformation mechanism changed from grain boundary diffusion to lattice self-diffusion. But this is not proper analysis method for deformation mechanisms. According to strain hardening exponent and strain rate sensitivity index, at higher strain rate, different mechanisms as diffusional creep, grain boundary sliding, glide-controlled creep and climb-controlled creep were found. In addition, at slower strain rate, diffusional creep and grain boundary sliding were prominent mechanism for diffusion.

11) With higher elongation to failure, value of m found higher. At slower strain rate, because of high m value ($m>0.33$), all of the alloys showed superplastic behavior, thus, deformation followed diffusional creep and grain boundary sliding mechanisms.

Future Work

This thesis is only an initial step of evaluating deformation mechanisms. Further analysis can be developed for describing dynamic grain growth from precipitations. Therefore, mechanisms of deformation can be understood from the microstructures.

References

1. U.S Energy Information Administration. International Energy Outlook 2016. U.S. Department of Energy, Washington, 2016
2. W.J. Joost and P.E. Krajewski, *Towards magnesium alloys for high-volume automotive application,* Scripta Materialia, **128**, 2017, pp.107–112
3. M. Lentz, M. Risse, N. Schaefer, W. Reimers and I. Beyerlein, *Strength and ductility with {10-11}-{10-12} double twinning in a magnesium alloy*, Nature Communications, **7(11068)**, 2016, pp.1-7
4. S.M. Razavi, D.C. Foley, I. Karaman, K.T. Hartwig, O. Duygulu, L.J. Kecskes, S.N. Mathaudhu and V.H. Hammond, *Effect of grain size on prismatic slip in Mg3Al1Zn alloy,* Scripta Materialia, **67**, 2012, pp.439-442
5. J.H. Jun, B.K. Park, J.M. Kim, K.T. Kim and W.J. Jung, *Effects of Ca addition on microstructure and mechanical properties of Mg-RE-Zn casting alloy,* Materials Science Forum, **488-489**, 2005, pp.107-110
6. M. Yang, C. Duan, H. Li, T. Guo and J. Zhang, *Effects of minor Ca addition on as-cast microstructure and mechanical properties of Mg–4Y–1.2Mn–1Zn (wt.%) magnesium alloy,* Journal of Alloys and Compounds, **574**, 2013, pp.165-173
7. S Wei, T Zhu, M Hodgson and W Gao, *Effects of Sn addition on the microstructure and mechanical properties of as-cast, rolled and annealed Mg–4Zn alloys*, Materials Science and Engineering: A, **585**, 2013, pp.139-148
8. P. Metalnikov, G. Ben-Hamu, D. Eliezer and K.S. Shin, *Role of Sn in microstructure and corrosion behavior of new wrought Mg-5Al alloy*, Journal of Alloys and Compounds, **777**, 2019, pp.835-849
9. J.C. Oh, T. Ohkubo, T. Mukai and K. Hono, *TEM and 3DAP characterization of an age-hardened Mg-Ca-Zn alloy*, Scripta Materialia, **53**, 2005, pp.675-679
10. L.L. Chang, H. Tang and J. Guo, *Strengthening effect of nano and micro-sized precipitates in the hot-extruded Mg-5Sn-3Zn alloys with Ca addition,* Journal of Alloys and Compounds, **703**, 2017, pp.552-559
11. H. Pan, G. Qin, Y. Huang, Y. Ren, X. Sha, X. Han, Z. Liu, C. Li, X. Wu, H. Chen, C. He, L. Chai, Y. Wang and J. Nie, *Development of low-alloyed and rare-earth-free magnesium alloys having ultra-high strength,* Acta Materialia, **149**, 2018, pp.350-363

12. F.R. Cao, H. Ding, Y.L. Li, G. Zhou and J.Z. Cui, *Superplasticity, dynamic grain growth and deformation mechanism in ultra-light two-phase magnesium–lithium alloys*, Materials Science and Engineering: A, **527**, 2010, pp.2335-2341
13. F. Czerwinski, *Magnesium and Its Alloys, Magnesium Injection Moulding,* Springer, Boston, MA, 2008, p.1
14. M. M. Avedesian and H. Baker, *ASM Specialty Handbook—Magnesium and Magnesium Alloys*, Materials Park, OH: ASM International, 1999, pp.210-226
15. Metal-Profile-Magnesium, The balance, 2019
16. Periodic table-element-12-magnesium. Royal society of chemistry.
17. Z. R. Zeng, M. Z. Bian, S. W. Xu, C. H. J. Davies, N. Birbilis and J. F. Nie, *Effects of dilute additions of Zn and Ca on ductility of Magnesium alloy sheet,* Materials Science & Engineering A, **674**, 2016, pp.459-471
18. G. E. J. Poinern, S. Brundavanam and D. Fawcett, *Biomedical magnesium alloys: A review of material properties, surface modifications and potential as a biodegradable orthopaedic implant,* American Journal of Biomedical Engineering, **2(6)**, 2012, pp.218-240
19. K. U. Kainer, *Magnesium–Alloys and Technologies*, Weinheim, Cam- bridge: Wiley-VCH, 2003, pp.252-253
20. Standard Practice for Temper Designations of Magnesium Alloys, Cast and Wrought, ASTM B296 – 03, 2008
21. R. E. Brown and M. Kutz, *Mechanical engineers' handbook: Materials and mechanical design*, John Wiley & Sons: 3rd edition, **1**, 2006, pp.278–286
22. H. E. Friedrich and B. L. Mordike, *Magnesium technology–metallurgy, design data, applications*, Springer, 2006, p.93
23. C. Cáceres and A. Blake, *The strength of concentrated Mg–Zn solid solutions,* Physica status solidi (a), **194(1)**, 2002, pp.147-158
24. B. C. Suh, J. H. Kim, J. H. Bae, J. H. Hwang, M. S. Shim and N. J. Kim, *Effects of Sn addition on microstructure and deformation behavior of Mg-3Al alloy,* Acta Materialia, **124**, 2017, pp.268-279
25. E. Emley, *Principles of magnesium techonologies*, Pergamon Press, Oxford, 1966
26. A. Luo and M. Pekguleryuz, *Cast magnesium alloys for elevated temperature applications,* Journal of Materials Science, **29(20)**, 1994, pp.5259-5271
27. J. B. Clark, *Age hardening in a Mg-9 wt.% Al alloy,* Acta Metallurgica, **16(2)**, 1968, pp.141-152

28. M. O. Pekguleryuz and A. A. Kaya*, Creep resistant magnesium alloys for powertrain applications,* Advanced Engineering Materials, **5(12)**, 2003, pp.866–878
29. S. Sandlobes, S. Zaefferer, I. Schestakow, S. Yi and R. G. Martinez, *On the role of non-basal deformation mechanisms for the ductility of mg and mg-2013y alloys*, Acta Materialia, **59(2**), 2011, pp.429 – 439
30. C. Lee, B. Duggan, *A simple theory for the development of inhomogeneous rolling textures*, Metallurgical Transactions A, **22(11)**, 1991, pp.2637– 2643
31. G. Proust, C. N. Tome, A. Jain and S. R. Agnew, *Modeling the effect of twinning and detwinning during strain-path changes of magnesium alloy {AZ31},* International Journal of Plasticity, **25(5)**, 2009, pp.861 – 880
32. M. Homayonifar and J. Mosler, *On the coupling of plastic slip and deformation-induced twinning in magnesium: A variationally consistent approach based on energy minimization,* International Journal of Plasticity, **27(7)**, 2011, pp.983 – 1003
33. Y. Chang and D. M. Kochmann, *A variational constitutive model for slip-twinning interactions in hcp metals: application to single- and polycrystalline magnesium*, International Journal of Plasticity, **73**, 2015, pp.39-61
34. R. E. Smallman and R.J. Bishop, *Metals and materials: Science, processes, applications,* Sydney: Butterworth-Heinemann Ltd, 1995, pp.281-283
35. G. E. Dieter, *Mechanical Metallurgy*, SI Metric, London: McGraw- Hill, 1988
36. F. J Humphreys. and M. Hatherly, *Recrystallization and related annealing phenomena,* Pergamon, Oxford, U.K, 1996
37. R. A. P. Djaic and J.J. Jonas, *Metallurgical transactions,* **4**, l973, p . 62l.
38. M. M. Avedesian and H. Baker, *ASM specialty handbook—Magnesium and magnesium alloys*, Materials Park, OH: ASM International, 1999
39. W. D. Callister and D.G. Rethwisch, *Materials science and engineering*, John Wiley & Sons NY, **5**, 2011
40. I. Polmear and D.S. John, *Light alloys: from traditional alloys to nanocrystals*, Butterworth- Heinemann, 2005
41. S. Celotto, *TEM study of continuous precipitation in Mg–9 wt% Al–1 wt% Zn alloy,* Acta materialia, **48(8)**, 2000, pp.1775-1787
42. K. U. Kainer, *Magnesium–alloys and technologies*, Weinheim, Cam- bridge: Wiley-VCH, 2003

43. A. A. N. Hashemi and J. B. Clark, *The Ca-Mg (Calcium-Magnesium) system*, Bulletin of Alloy Phase Diagrams, **8**, 1987, pp.58–65
44. J. L. Haughton, *Alloys of magnesium. Part 6—the construction of the magnesium-rich alloys of magnesium and calcium,* Journal of Institute of Metals, **61**, 1937, pp.241–246
45. H. Vosskühler, *The Phase diagram of magnesium-rich Mg-Ca alloys,* Zeitschrift fur Metallkunde, **29**, 1937, pp.236–237
46. C. L. Mendis, D. Tolnai, C. Blawert and N. Hort, *Effects of Sn addition on the Age Hardening Response, Microstructures and Corrosion Resistance of Mg-0.8 Ca (wt%) Alloys,* Magnesium Technology, 2013, pp.237-241
47. F. Wang, H. Dong, S. Sun, Z Wang, P. Mao and Z. Liu, *Microstructure, tensile properties and corrosion behavior of die cast Mg-7Al-1Ca-xSn alloys,* Journals of Materials Engineering and Performance, **27(2)**, 2018, pp.612-623
48. H. K. Kim, *Activation energies for the grain growth of an AZ31 Mg alloy after equal channel angular pressing,* Journal of materials science, **39**, 2004, pp.7107-7109
49. D. S. Wilkinson and C. H. Caceres, *On the mechanism of strain enhanced grain growth during superplastic deformation*, Acta Metall, **32(9)**, 1984, pp.1335-1345
50. B. M. Watts and M. J. Stowell, *Variation in flow stress and microstructure during superplastic deformation of the Al-Cu eutectic*, Journal of Materials Science, **6**, 1971, pp.228-237
51. H. G. Jeong, Y. G. Jeong and W. J. Kim, *Microstructure and superplasticity of AZ31 sheet fabricated by differential speed rolling*, Journal of Alloys and Compound, **483**, 2009, pp.279-282
52. F. Li and A. K. Ghosh, *Anisotropy of dynamic grain growth in a superplastic aluminum- magnesium alloy,* Materials Science Forum, **217-222**, 1996, pp.535-540
53. B. Zhang, P. S. Bate and N. Ridley, *The Effect of strain rate history on the dynamic grain growth behavior of AA 5083*, Materials Science Foram, **551-552**, 2007, pp.627-632
54. D. W. Livesey and N. Ridley, *Activation energies for superplastic tensile and compressive flow in microduplex α/β copper alloys,* Journal of materials science, **19**, 1984, pp.3602-3611
55. T. G. Nieh, J. Wadsworth and O. D. Sherby, Superplasticity in Metals and Ceramics, Chapter 3, 4, 6, 10, 2005

56. G. S. Kim, *Small volume investigation of slip and twinning in magnesium single crystal*, HAL, 2012
57. D. Kapinos, B. Augustian and M. Szymanek, *Methods of introducing alloying elements into liquid magnesium,* Metallurgy and Foundry Engineering, **40**, 2014, pp.141-160
58. A. A. N. Hashemi and J. B. Clark, *The Mg-Sn (Magnesium-Tin) system*, Bulletin of Alloy Phase Diagrams, **5(5)**, 1984, pp.466–476
59. B. N. Kim, K. Hiraga, Y. Sakka, and B. W. Ahn, *A grain boundary diffusion model of dynamic grain growth during superplastic deformation,* Acta Mater, **47(12)**, 1999, pp.3433-3439
60. J. Sun, Y. Ma, H. Miao, K. Li, C. Li and H. Huang, *Effects of Ca concentration on microstructure and mechanical properties of as-cast and as-extruded quasicrystal-strengthened Mg-7.2Zn-2.4Gd alloy,* Advances in Materials Science and Engineering, **2018**, 2018, pp.1-7
61. Y. Pan, C. Chen, R. Feng, H. Cui, B. Gong, T. Zheng and Y. Ji, *Effect of calcium on microstructure and corrosion behavior of microarc oxidized Mg-xCa alloys,* Biointerphases, **13(1)**, 2018, pp.1-6
62. X. Zhao, S. Li, Y. Xue and Z. Zhang, *An investigation on microstructure, texture and mechanical properties of az80 mg alloy processed by annular channel angular extrusion,* Materials, **12(6)**, 2019, pp.1-16

Appendix A

EDX of Mg-1Ca Alloy:

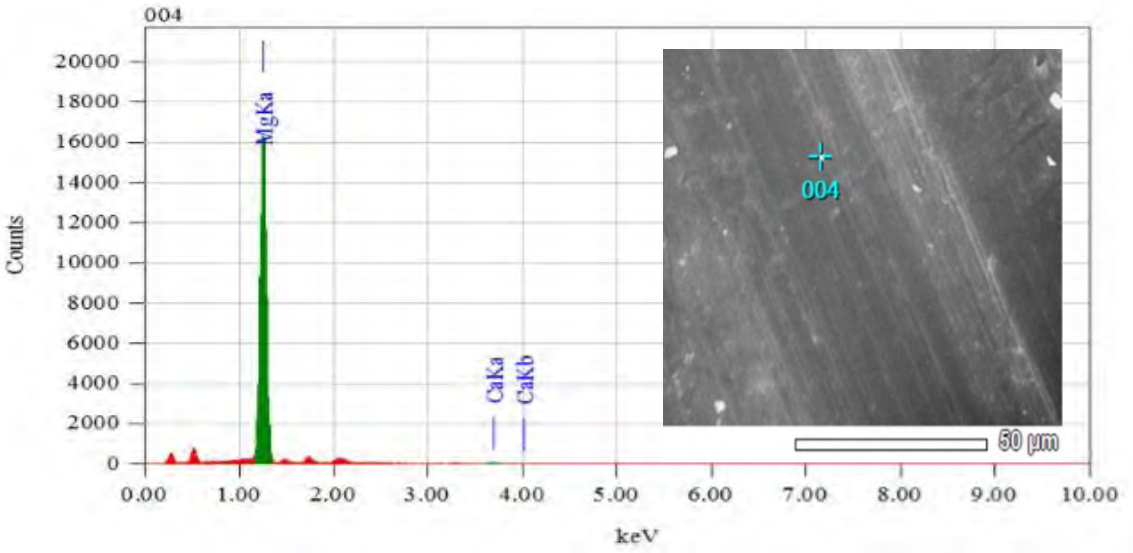

Figure 4.52: EDX of Mg_2Ca particle in Mg-1Ca alloy

EDX of Mg-1Ca-1Sn Alloy:

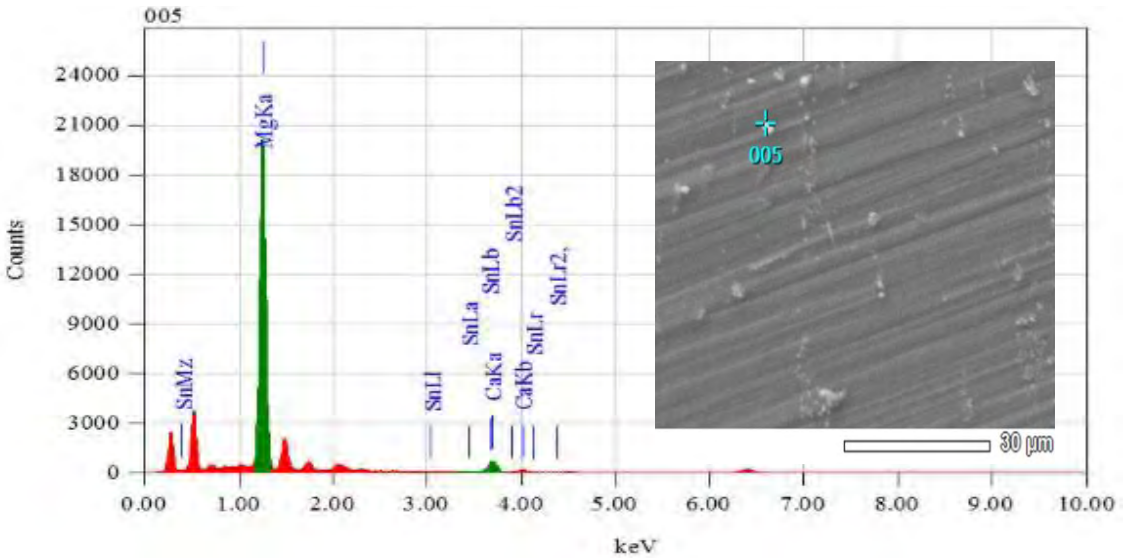

Figure 4.53(a): EDX of Mg_2Ca particle in Mg-1Ca-1Sn alloy

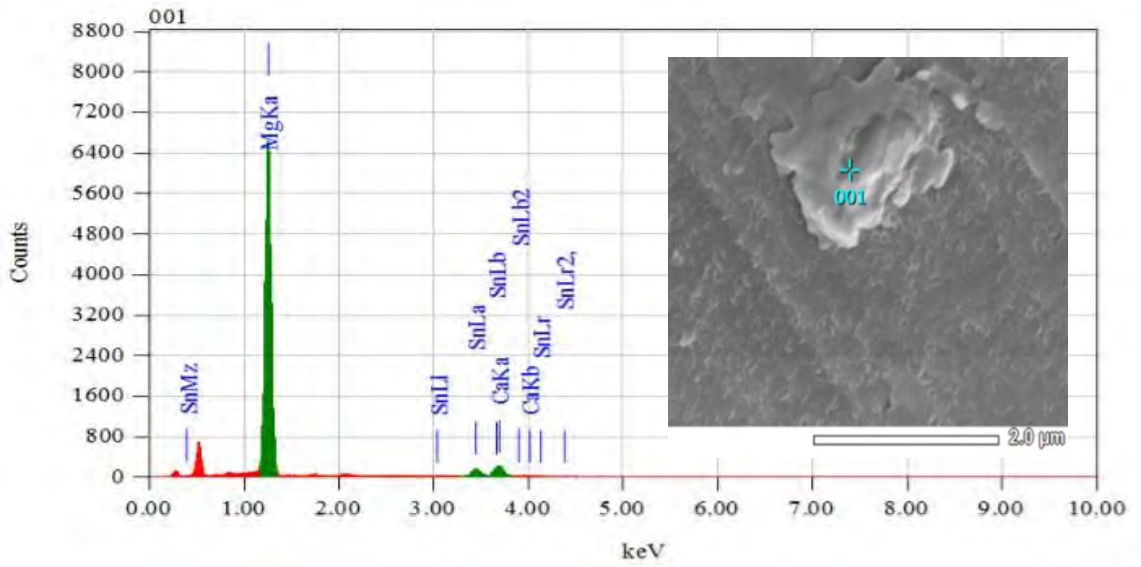

Figure 4.53(b): EDX of CaMgSn particle in Mg-1Ca-1Sn alloy

EDX of Mg-1Ca-2Sn Alloy:

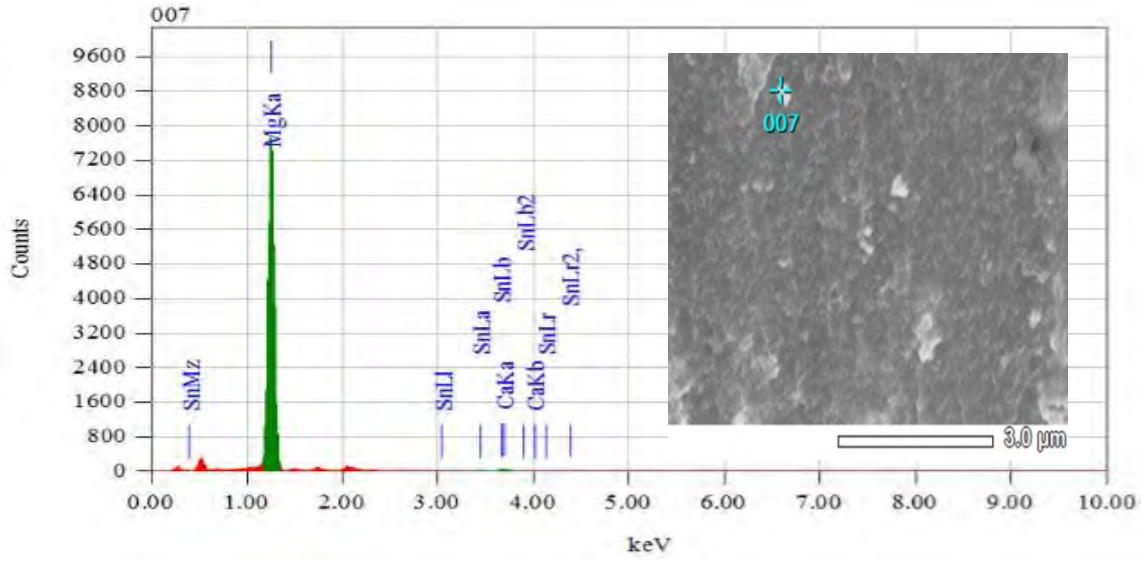

Figure 4.54(a): EDX of Mg_2Ca particle in Mg-1Ca-2Sn alloy

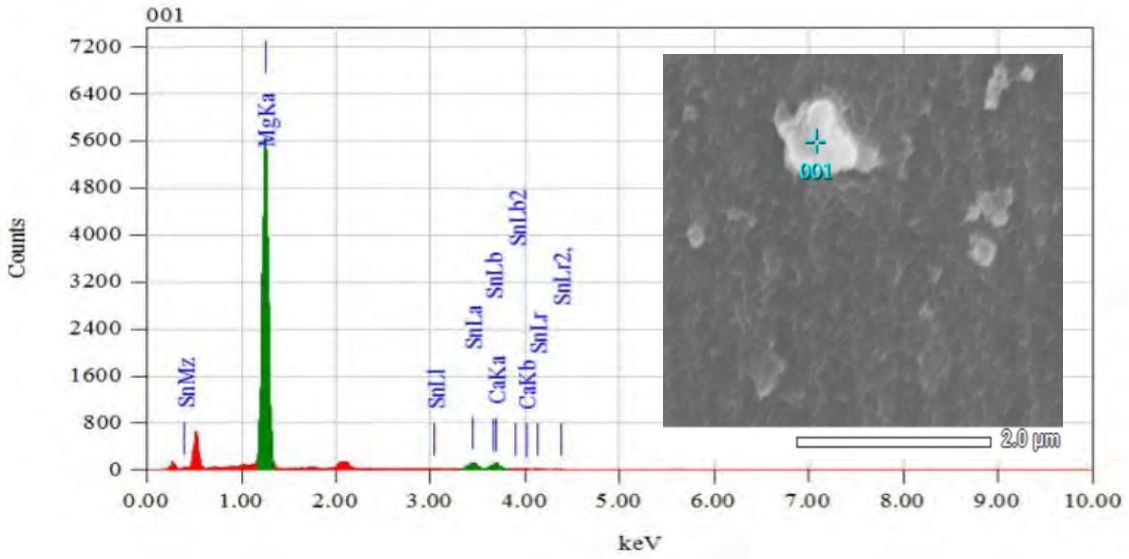

Figure 4.54(b): EDX of CaMgSn particle in Mg-1Ca-2Sn alloy

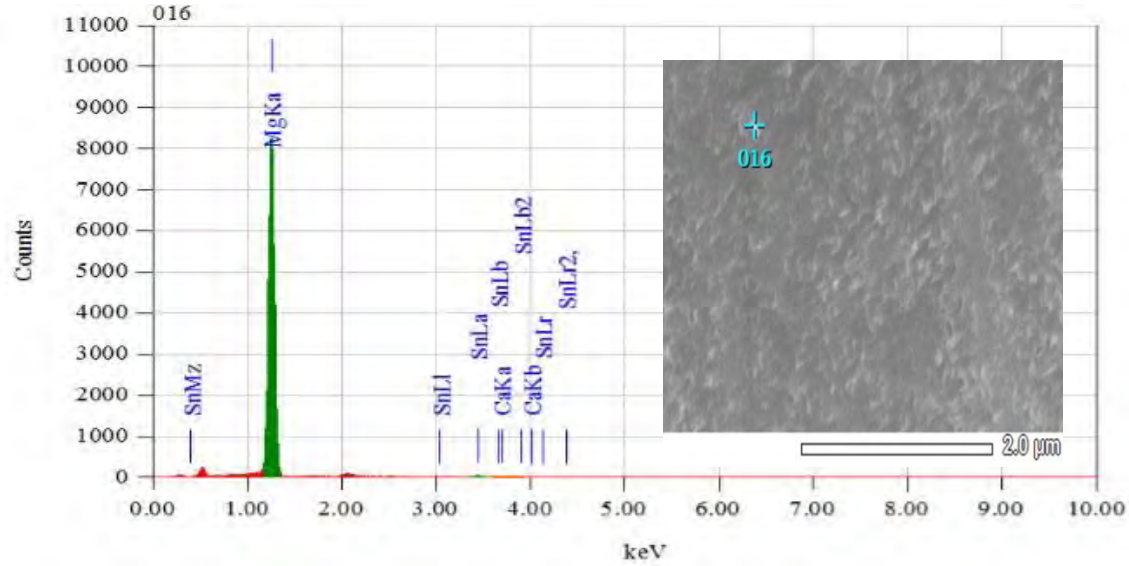

Figure 4.54(c): EDX of Mg_2Sn particle in Mg-1Ca-2Sn alloy

EDX of Mg-1Ca-4Sn Alloy:

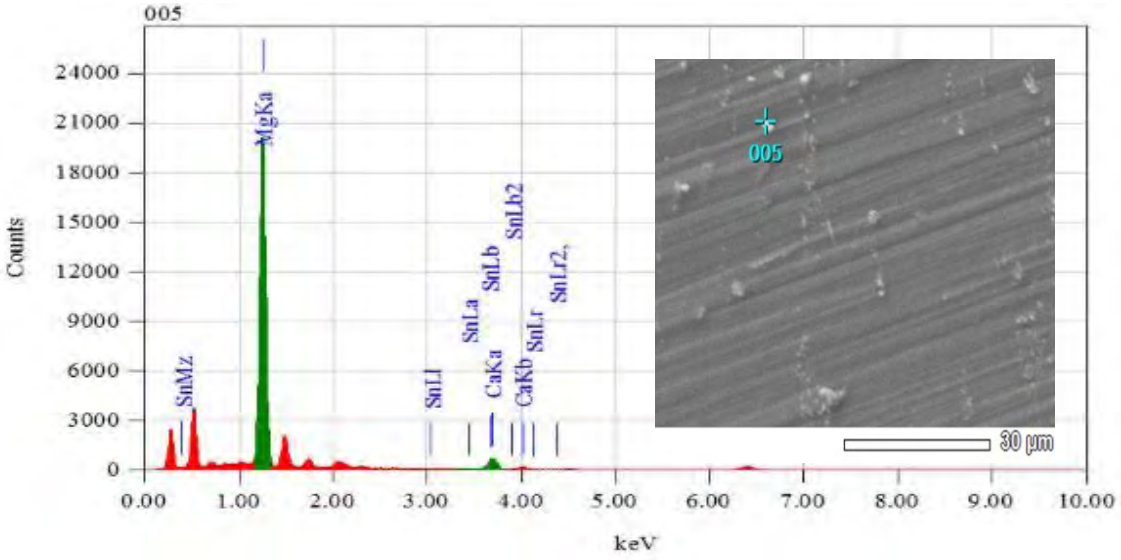

Figure 4.55(a): EDX of Mg_2Ca particle in Mg-1Ca-4Sn alloy

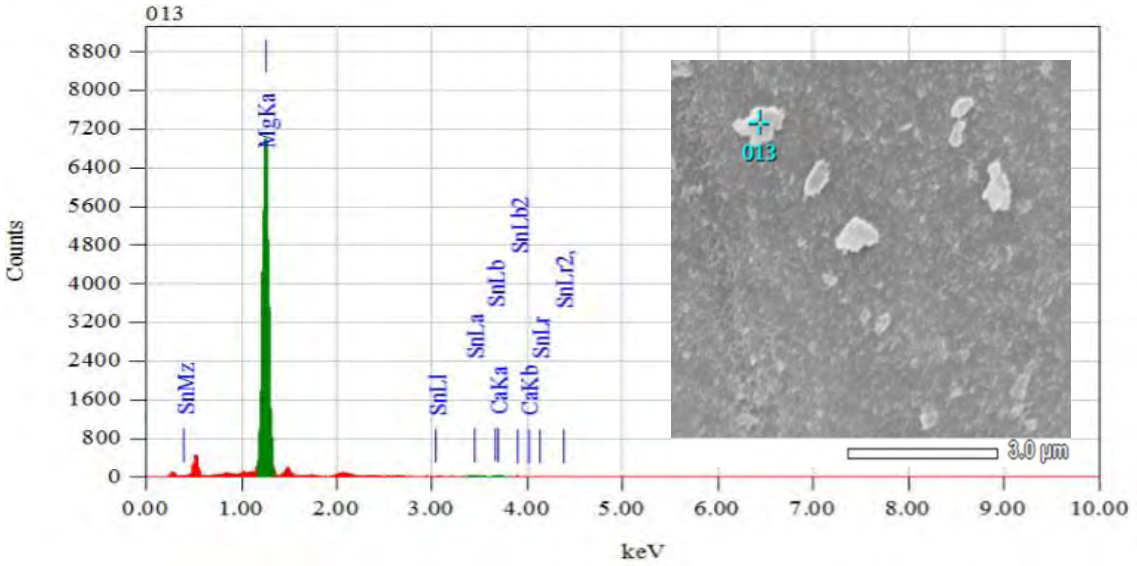

Figure 4.55(b): EDX of CaMgSn particle in Mg-1Ca-4Sn alloy

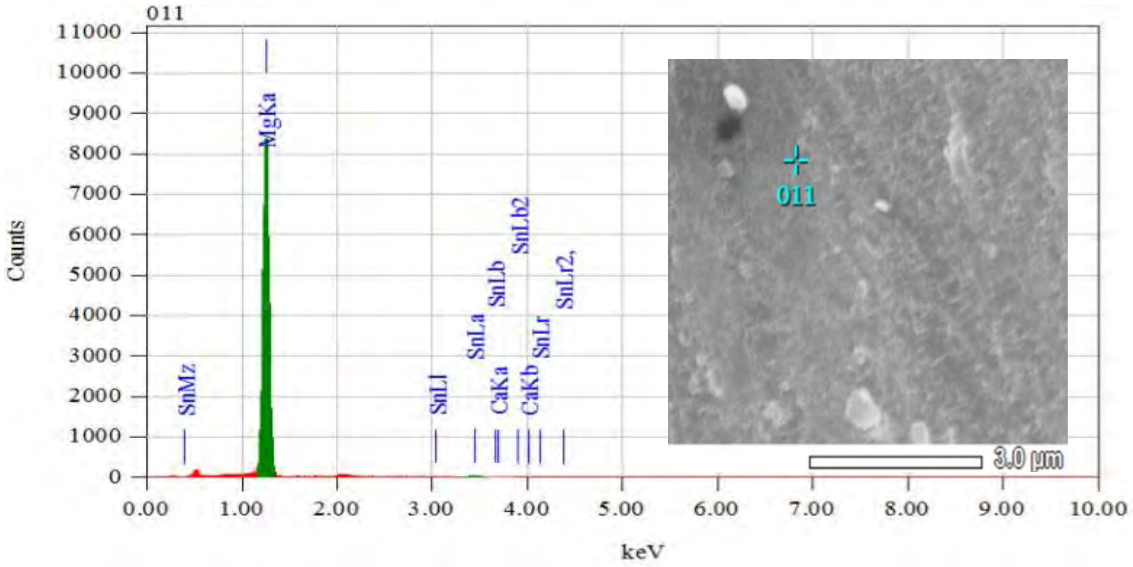

Figure 4.55(c): EDX of Mg_2Sn particle in Mg-1Ca-4Sn alloy